INVESTIGATING SINGLE CRYSTAL PLASTICITY OF NIOBIUM WITH A DISLOCATION MECHANICS-BASED MODEL

By

Eureka Pai Kulyadi

A DISSERTATION

Submitted to
Michigan State University
in partial fulfillment of the requirements
for the degree of

Materials Science and Engineering – Doctor of Philosophy

2022

ABSTRACT

One suggested method to manufacture superconducting radio frequency (SRF) cavities, which are used as driving units in particle accelerators, is the deep-drawing of Niobium (Nb) disks that were cut from large-grained ingots. This is a promising and cost-effective alternative to the current industry standard of deep-drawing rolled poly-crystalline sheets. It is essential to understand the sources of the observed variability in the performance of cavities fabricated by either process in order to define the most suitable fabrication route.

Cavity performance is hampered by material defects such as dislocations or crystallite boundaries that can arise and evolve during deformation processes involved in the mechanical shaping of the cavity (mostly by deep-drawing). Such defects can trap magnetic flux causing significant dissipative losses leading to reduced performance. Understanding dislocation mechanics in Nb based on deformation experiments allows predictive modeling to enable informed design strategies for optimal cavity fabrication and improved performance.

Crystal plasticity (CP) modeling is a powerful and well-established computational materials science tool to investigate mechanical structure–property relations in crystalline materials. A dislocation mechanics-based constitutive description of plastic deformation in body-centered cubic (BCC) metals is used to formulate a CP model for Nb. Uniaxial tension experiments on several Nb single crystals cut from a large-grained ingot disk were conducted at several different strain rates. The specific selection of grains and the in-plane orientation of deformation samples cut from those grains were based on the active slip systems anticipated from Schmid factor calculations. The results from these specifically designed deformation experiments are used to validate the model.

Simulations and corresponding deformation experiments exhibit notable discrepancies in terms of the stress–strain response and lattice reorientation. These discrepancies are rationalized by considering the effect of a distribution in pre-existing dislocation densities across the possible slip systems, which entails a significant variability in the resulting slip system activity and associated crystal re-orientation and strain hardening behavior. An exhaustive numerical study probing thousands of initial dislocation density distributions could be condensed into inverse pole figure (IPF)

maps that chart the range of crystallographic tensile directions for which stable outcomes can be expected despite a given variability in the pre-existing dislocation density distribution. Consequently, it becomes clear that while single-crystal experiments can be a useful guide toward the development and testing of dislocation mechanics-based models, the expectation of a one-to-one matching between any specific experiment and its corresponding simulation is not easily achieved, since the exact values and distribution of pre-existing dislocations in the sample is generally unknown (and likely unknowable).

To my dearest mother, for her continual guidance, encouragement and inspiration

ACKNOWLEDGEMENTS

I am deeply grateful to my advisor Dr. Philip Eisenlohr for his commitment to guide me throughout the course of my thesis. In addition to his commitment, he allowed me to share his experiences and principles, and in doing so not only influenced this work positively, but also shaped my view of scientific working methods and their implementation. I will always cherish our impromptu meetings. Whether it was a 5 minute discussion, 2 hour brainstorm session or a 4 hour long joint debugging session, it was always enjoyable.

I would also like to thank Dr. Thomas Bieler for his joint supervision on my project and his pleasant cooperation, both professionally and personally. My approach towards research problems is significantly influenced by the discussions which I had with Dr. Bieler. His appreciation of progress, both small and significant, was immensely useful throughout my journey, especially while navigating tough problems.

I express my gratitude to my committee members, Dr. Carl Boehlert and Dr. Yang Guo, for reviewing my thesis progress over the years and for their valuable inputs and encouragement.

I would also like to thank past and present collaborators of the SRF Niobium group for their discussions in many weekly meetings and continuous appreciation of my contributions. I also extend my sincere thanks to past and present members of the Computational Materials Mechanics research group and the Metals research group, for the scientifically stimulating discussions and the valuable suggestions over the years.

I would like to thank Jean-Francois Croteau and Elisa Cantergiani and for enabling a successful collaboration that provided me with a rich data set for analysis.

Graduate school would not have been smooth without my close friends, who have always been my cheerleaders and encouraged me to chase my aspirations, both personally and professionally. I especially would like to thank Manas, Rakesh, Kalyani, Mario, Supreeth, Vidyashankar and Subhrajit for keeping my spirits up, especially during the pandemic.

My heartfelt gratitude to my dearest mother for her unconditional love, constant encouragement, and countless sacrifices. I thank my siblings for all the joys we shared and for always

thinking of me. I thank Dr. and Mrs. Garimella for being my loving family away from India. Last but not the least, I thank my dear husband Girish for his love, support, inspiration and for making the journey more memorable.

This work was funded by the US Department of Energy's Office of High Energy Physics, grant number DE-SC0009962. Jean-Francois and Elisa would like to thank the Marie Sklodowska-Curie Action (MSCA) Innovative Training Network (ITN) and funding from the European Union's H2020 Framework Programme under grant agreement no. 764879.

TABLE OF CONTENTS

LIST OF ABBREVIATIONS

SRF Superconducting Radio Frequency

RF Radio Frequency

CP Crystal Plasticity

IPF Inverse-Pole Figure

ILC International Linear Collider

BCC Body Centered Cubic

ECCI Electron Channeling Contrast Imaging

EBSD Electron Back-Scattered Diffraction

RSS Resolved Shear Stress

CRSS Critical Resolved Shear Stress

SF Schmid factor

DAMASK Düsseldorf Advanced Material Simulation Kit

MPIE Max-Planck-Institut für Eisenforschung

FE Finite Element

RRR Residual Resistivity Ratio

EDM Electron Discharge Machining

FFT Fast Fourier Transform

CHAPTER 1

INTRODUCTION

1.1 SRF technology overview

Superconducting radio frequency (SRF) technology is a complex multidisciplinary field that is continuously advancing and researched for use in high-energy physics, nuclear physics, life sciences and materials science [64]. SRF particle accelerators have shown the ability to offer better power savings and improved beam quality as compared to conventional copper accelerators [62, 63]. A key component of a modern particle accelerator is the electromagnetic resonator cavity that imparts energy to the charged particles [64]. This cavity is a metallic structure made up of a string of ellipsoidal cells and is known as the *SRF* cavity [61]. As charged particles pass through the SRF cavity during radio-frequency induction, the polarity of the electromagnetic field between adjacent cells switches so as to maintain the direction of acceleration. The number of cavities in an accelerator depends on the characteristics of the particles and their desired velocity [63].

Figure 1.1 A 1m, nine-cell 1.3 GHz superconducting niobium cavity used in the ILC [6].

The introduction of superconducting material in place of copper in the 60s was a major advance towards better performing accelerators [62]. One of the primary advantages of superconducting cavities is that the energy losses from the cavity walls is several orders of magnitude lower than that of a copper wall [62]. Another benefit is that superconducting cavities can have larger beam openings than copper cavities which reduces beam-cavity interactions and therefore improves the beam quality and current, and consequently the precision of the experiment [62].

Many superconducting materials may be potentially considered, but Niobium (Nb) has proved to be the winning choice because it has the highest superconducting transition temperature (T_c)

among elemental metals. It also has good machinability, formability and thermal conductivity which are requirements to its application [4, 52].

Figure 1.1 shows the assembly of a TESLA 9-cell SRF cavity used for designing the International linear Collider (ILC) [6]. The larger diameter of the ellipsoid is called the equator and the smaller diameter is called the iris.

The fabrication of superconducting radio frequency (SRF) cavities with better performance and reduced manufacturing costs is important to design particle accelerators with superior collision energies. The performance of SRF cavities is linked to two parameters:

- The quality factor (Q_0), which is the number of oscillations a resonator would take to dissipate its stored energy.
- The accelerating field/gradient (E_{acc}), which is the average electric field by which the particles in the cavity are accelerated [64]

Higher values of Q_0 indicate more efficient power use, and higher values of E_{acc} result in higher particle velocities, which enable new discoveries in physics. Continuing research in Nb for SRF cavities is driven by the need to increase cavity performance by improving these values.

1.2 SRF cavity performance issues

The performance of SRF cavities are mainly limited by the cavity material limitations for high energy applications. Material defects such as voids, inclusions, hydrides, impurity atoms, dislocations and grain boundaries are major sources of these limitations [4]. These arise in the cavity fabrication route during processing steps such as ingot purification, forging, rolling, deep drawing and welding. Some of the cavity performance issues are explained below.

Magnetic flux pinning is a phenomenon where incoming magnetic flux from the applied magnetic field is trapped at pinning centers in the cavity. When the field is withdrawn or expelled by becoming superconducting, the residual flux lines introduces errors in the measurement of the critical magnetic field. Dislocations and interstitial impurities are known defects that serve as flux pinning centers. Using appropriate etching and heat treatments after cavity forming can minimize the presence of these defects and consequently reduce flux pinning [64].

Multipacting, also known as resonant field emission is a phenomenon where electrons emitted from the surface of the cavity re-impact the cavity wall after emission. This effect causes secondary electrons to escape from the surface resulting in an avalanche effect which can consume all available power leading to cavity failure. To prevent this issue, cavity design changes were employed so that the drift the emitted electrons is towards the equator which is a region of zero surface electric field [64].

Thermal breakdown, also known as a quench, is a phenomenon where the temperature of the cavity exceeds T_c leading to significant energy losses. This is a localized effect in which the presence of defects on the cavity surface causes a local increase in temperature. The fraction of normal conducting electrons thus increases, thereby increasing resistance that leads to power dissipation. Improving the thermal conductivity of Nb by improved material purity has been the primary method of eliminating this issue [64].

Although significant improvements have been achieved to reduce the likelihood of these issues, the origin of these issues are not well understood. Over the years, research and development efforts have focused on the material aspects of Nb for SRF cavities. Material defects such as dislocations major contributors to cavity performance issues. Understanding the metallurgy and deformation mechanics of Nb is key to establish remedies to these performance issues.

1.3 Large-grain approach to cavity forming

While cavity manufacturing favors specifications that call for fine-grained Nb sheets, using large-grained ingot slices for cavity forming and the idea of single crystal cavities has gained a lot of interest due to its potential to significantly reduce fabrication costs while still achieving comparable or even better cavity performance [43, 44]. This idea was first proposed and demonstrated by Jefferson Lab.

In the well-established fine-grain approach, ingots of pure Nb are broken down by forging, milling, and rolling that includes a couple of intermediate heat treatments to retrieve formability. Alternatively, in the large-grain approach, disks are directly sliced from the ingots. Figures 1.2 and 1.3 are schematic flow diagrams of the fine-grain the large-grain approach to cavity forming

respectively.

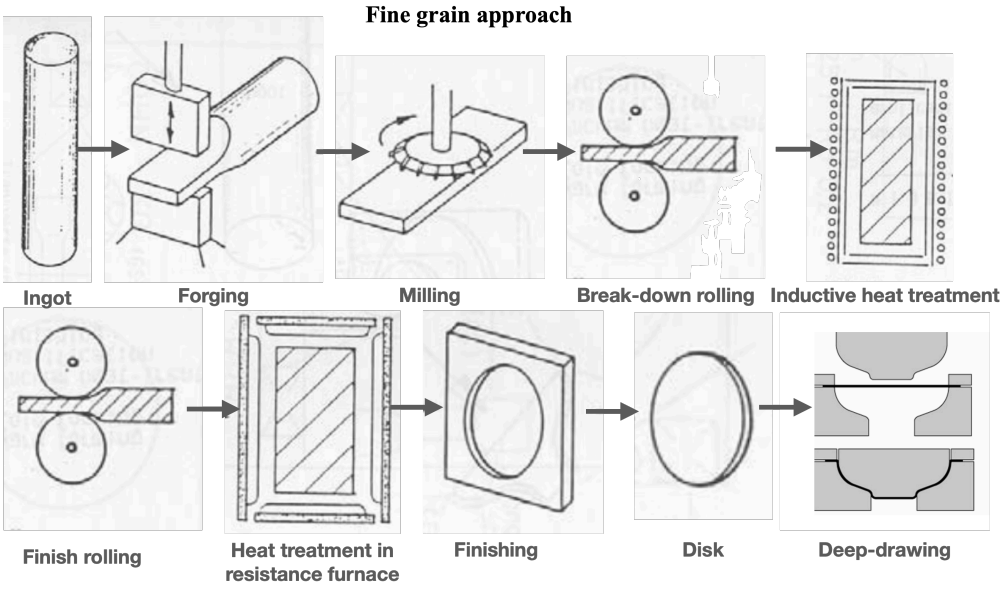

Figure 1.2 SRF cavity fabrication using the fine-grain approach, adapted from [40].

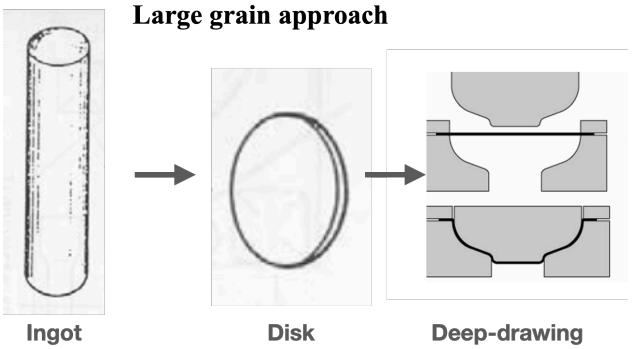

Figure 1.3 SRF cavity fabrication using the large-grain approach, adapted from [40].

An apparent difference between disks obtained from the two methods is the average grain size. Fine grain disks usually have a uniform grain size of approx. 50 µm, while the grain size for large grain disks is much less uniform, and can be as large as 20 cm [5]. Using the large-grain approach

eliminates intermediate rolling and annealing treatments thus avoiding unnecessary contamination. Also, it significantly reduces material waste and processing costs. Studies have also shown that smooth surfaces on large-grained slices can be easily obtained with simple a BCP etch which avoids the more complicated electropolishing procedure needed for fine-grained sheets [4]. Past work has also demonstrated that grain boundaries can facilitate magnetic flux trapping and cavity losses, which is yet another reason to explore the large-grain approach [40, 50, 67, 84, 85, 93].

However, due to the orientation dependence of mechanical properties observed in single-crystals, forming can result in highly anisotropic deformation, leading to irregular shapes with the large-grain approach [5, 7]. Therefore, the large-grain approach has poorer formability and dimensional stability than the fine-grain approach. Therefore, although large-grained cavities have the potential to improve cavity performance (due to fewer grain boundaries and dislocations), the major concern is whether this cost effective alternative can be understood well-enough to gain reasonable control on potential uncertainties in deformation [7].

1.4 Opportunities for research

As we try to continually improve the performance of SRF cavities, knowledge of the effect of the metallurgical state of Niobium on cavity performance is limited. The role of crystal structure and dislocation mechanisms are critical to understanding plasticity of niobium during cavity manufacturing. Dislocations are present in the undeformed material and evolve in number and configuration with each manufacturing step due to plastic deformation. There is a need for better predictive material models that track microstructure evolution during cavity processing. This needs a thorough understanding of the plastic deformation mechanisms in Nb. Crystal plasticity (CP) models require constitutive laws that take into account the effect of anisotropy of the material response to an external load. This makes it a powerful tool to investigate structure-property relationships and mechanical properties.

Single-crystal deformation experiments and their corresponding crystal plasticity simulations can be performed to fill the current knowledge gaps that exist for exploring the large-grain approach. The primary objective of this thesis is to develop a dislocation mechanics-based crystal

plasticity model that incorporates thermally activated kinetics of dislocation motion and the effects of their mutual interactions. This is formulated for pure Niobium for the purpose of predicting slip activity and the associated strain-hardening and lattice re-orientations using single-crystal simulations. The stress–strain response and lattice reorientations of several Nb single crystals measured from strategically designed uniaxial tension experiments are used for the purpose of validating the model [14]. Findings from this study aim to supplement prior knowledge in this field and provide insights into the feasibility of the large-grain approach to SRF cavity forming.

To help navigate through the thesis, an outline is presented here: First, a survey of the necessary knowledge required for this research is summarized in Chapter 2. This is followed by the experimental investigation of mechanical properties of single crystal Nb as Chapter 3. Next, the formulation of a dislocation mechanics-based crystal plasticity model and simulations of select specimens from experiments is documented in Chapter 4. An exhaustive numerical study probing thousands of initial dislocation density distributions which are then condensed into inverse pole figure (IPF) maps that chart the range of crystallographic tensile directions for which unique slip activity is expected based upon variability in the pre-existing dislocation density distribution is shown in Chapter 5. The overall summary of findings is written in Chapter 6. The key conclusions and recommendations for future work are summarized in Chapter 7.

CHAPTER 2

LITERATURE REVIEW

2.1 Dislocation basics

The information in this section is derived from standard works that describe dislocations: [19, 35, 37, 88]. Any additional sources are referenced separately.

One of the mechanisms that enables plastic deformation in metallic materials is dislocation slip. Dislocations are one-dimensional line defects that constitute the (necessarily closed) boundary between the slipped and non-slipped areas within a crystal lattice. The magnitude and direction of shear of a dislocation is defined by its Burgers vector, denoted by **b**. A slip plane is the plane of atoms that a dislocation glides on, and contains the Burgers vector **b** and line direction **t**. A slip system is composed of a slip direction and a slip plane, and multiple slip systems can be simultaneously activated during plastic deformation.

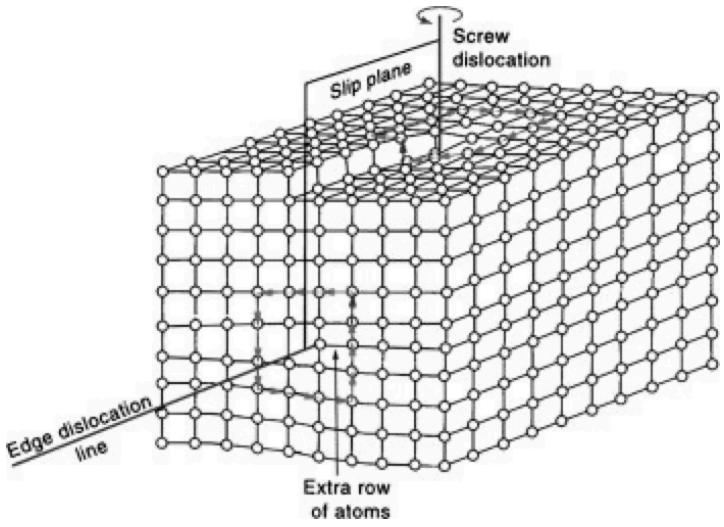

Figure 2.1 Geometry of edge and screw dislocations in a crystal lattice [72].

Dislocations can be categorized into two 'pure' types called edge and screw dislocations. An edge dislocation has its line direction perpendicular to the Burgers vector and can be thought of as an extra half-plane of atoms inserted into a perfect crystal lattice. A screw dislocation has its line

direction parallel to the Burgers vector and can be illustrated as a spiral ramp. A schematic of the edge and screw dislocations within an otherwise perfect crystal lattice is shown in Fig. 2.1. Dislocations with line directions between the limiting case of edge and screw have a mixed character.

A dislocation may glide under an applied stress if that stress translates to a sufficiently high shear stress ("resolved shear stress", RSS) on its slip plane in the direction of the Burgers vector. Dislocation slip is defined by the slip plane normal **n** and the slip direction **m**. In crystals, slip occurs on densely-packed planes containing both the dislocation line and the Burgers vector. Since the line direction is parallel to the Burgers vector for a screw dislocation, their motion can occur in any plane containing the dislocation line, whereas for edge dislocations slip can only occur on one particular plane that contains the perpendicular line direction and Burgers vector. An alternative (and non-volume-preserving) mechanism for edge dislocation motion is known as dislocation climb. Climb allows an edge dislocation to move perpendicular to its glide plane via diffusion of point defects in the lattice. Dislocation climb is temperature-dependent and typically occurs at high homologous temperatures, whereas slip is common for most metals at room temperature.

The density of dislocations in a material is increased by their storage and multiplication owing to their mutual interactions and cutting processes. These mechanisms increase the stress in metallic crystals during plastic straining and this process is known as strain hardening. Presence or addition of pinning points such as alloying elements can strengthen the material further by serving as obstacles for dislocation motion and consequently causing the material to have a higher resolved stress to overcome those obstacles. One way of eliminating dislocations is by the annihilation of two dislocations with opposite Burgers vectors. Dislocations can disappear at a free surface or be absorbed into a grain boundary.

2.2 Plastic deformation in BCC metals

The geometrical and crystallographical peculiarities of plastic deformation in BCC metals have been of interest since the 1920s. Some of the unusual features include 'anomalous slip' where slip occurs on planes that do not satisfy the maximum resolved shear stress and 'twinning / anti-twinning asymmetry' which is an asymmetric stress response to the direction of slip [11, 12, 22, 24, 25, 31, 34, 36, 58, 86, 87, 89, 90]. These features have been widely described as the breakdown of the rule of geometric projection of the resolved shear stress (RSS) from the stress tensor, commonly known as *Schmid* law [75]. These phenomena have been widely reported in literature both experimentally and computationally and are a clear contrast to the plastic behavior of face-centered cubic (FCC) and hexagonal close-packed (HCP) metals. BCC single crystals have also shown a characteristic temperature dependence of flow stress owing to the thermally activated nature of screw dislocation glide [3, 10, 11, 77, 87].

These peculiarities in the plastic behavior complicate the understanding and manipulation of BCC metals for practical applications. Computational methods have emerged as a way of shining light on some of the above-mentioned characteristics, providing physically-aware explanations of experimental observations. Over the past decades, research and development in this area have improved the understanding of the nuances of dislocation mobility and mechanisms of plasticity in BCC metals resulting in the ability to formulate better predictive models.

2.2.1 Active slip systems

Establishing the primary slip systems in BCC metals is critical to understanding and modeling deformation behavior. The onset of plastic flow in metals happens when the resolved shear stress (RSS) on a slip system reaches a critical value known as the critical resolved shear stress (CRSS). This yield criterion is famously called the Schmid law [75]. Slip typically occurs on crystallographic planes with the highest planar density of atoms and along the most tightly packed directions as such combinations are known to offer the least resistance to the dislocation motion.

Unlike face-centered cubic (FCC) and hexagonal close-packed (HCP) metals, BCC metals do not have close-packed crystallographic planes. Experimental observations have shown dislocation

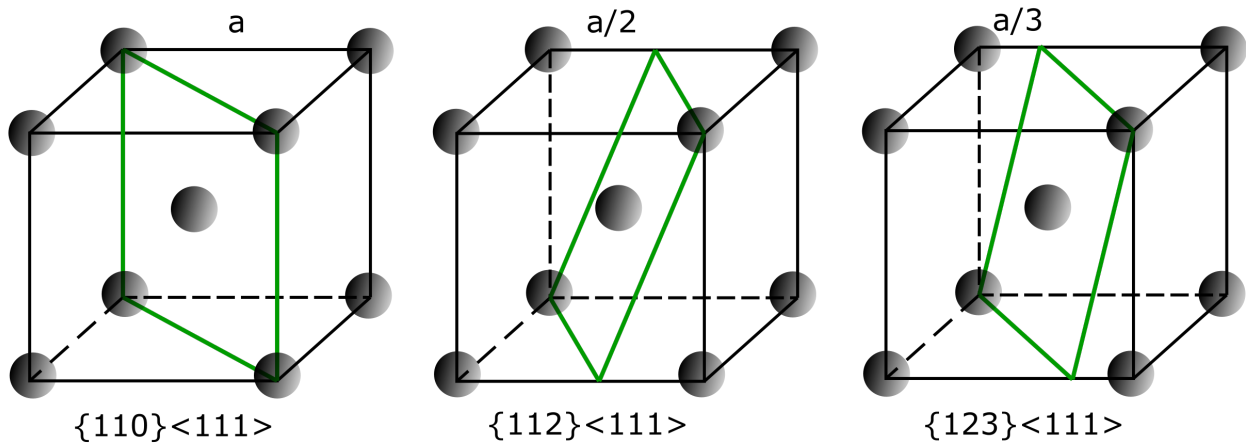

Figure 2.2 Observed slip systems in BCC metals.

slip along the close-packed $\langle 1\,1\,1 \rangle$ directions but the plane(s) of the primary active slip systems have been inconclusive [12, 89, 95]. Due to their high stacking fault energy, stable stacking faults have not been observed in BCC metals and, therefore, dissociated dislocations have not been reported. Kocks [46] described "pencil glide," in which slip occurs in $\langle 1\,1\,1 \rangle$ directions without following any particular slip planes.

Slip trace analysis is widely used in fundamental studies of slip. During deformation, dislocations that transport onto a free surface form respective slip traces. These slip traces can be imaged using optical microscopy, scanning electron microscopy (SEM), and atomic force microscopy (AFM). The discrepancies in the primary slip planes in BCC metals were reported by identifying slip traces on deformed single crystals which were ill-defined and wavy [21, 33]. It is generally accepted that the waviness is a consequence of cross-slip of the screw dislocations [78].

At various temperature and strain-rate regimes, BCC metals have reported slip on $\{1\,1\,0\}$, $\{1\,1\,2\}$ and $\{1\,2\,3\}$ planes which intersect along a common $\langle 1\,1\,1 \rangle$ direction [33] A schematic of the active slip systems in BCC metals is shown in Fig. 2.2.

Investigation of slip in Nb began when several researchers deformed single crystal Nb under different experimental conditions [9, 24, 29, 47, 54]. Maddin and Chen [54] performed optical slip trace analyses and Laue X-ray diffraction and identified slip traces only on 110 planes in Nb at room temperature under tension and compression. However, Duesbery and Foxall [24] found slip

traces on either $\{1\,1\,0\}$ or $\{1\,1\,2\}$ planes depending on the direction of stress and the orientation of single crystals. Raabe and Lücke [69] observed slip on $\{1\,2\,3\}$ in Nb at large strains at room temperature. Seeger and Wasserbäch [78] showed that high purity BCC metals such as Nb may exhibit 'anomalous slip', which is unexpected slip on a $\{1\,1\,0\}$ plane with much lesser resolved shear stress than on the primary $\{1\,1\,0\}$ slip plane with the highest resolved shear stress. He explained that anomalous slip was prevalent in Nb even when the stress axis of a crystal orientation was located near the center of the standard stereographic triangle. More recently, Baars [5] analyzed Nb single crystals with different orientations cut from a large grain Nb ingot slice. The orientations were selected such that either a single slip system or a combination of slip systems would be activated. The results indicated that the dominant slip systems at yield are always $\{1\,1\,2\}$. This conclusion is based on the observation that the strain-hardening of a sample that was oriented to favor a single $\{1\,1\,0\}$ slip system resembled another sample that favored two intersecting $\{1\,1\,2\}$ slip systems [5]. Finally, it was concluded that the onset of hardening in both samples was predominantly caused by two $\{1\,1\,2\}$ slip systems interacting with each other [5]. More recently, Kang [40] performed single crystal Nb tensile tests followed by slip trace analyses and concluded that the preferred active slip planes are dependent on the pre-existing dislocations. Non-annealed samples with pre-existing dislocations preferred the $\{1\,1\,2\}$ planes, while annealed samples of the same orientation preferred $\{1\,1\,0\}$ planes. Another recent study on single crystal Tantalum by Lim et al. [51] showed that experimental observations and crystal plasticity modeling support dominant dislocation slip along $\{1\,1\,2\}$ planes under compressive load.

2.2.2 Theory of dislocation activity in BCC metals

In-situ electron microscopy observation of dislocations in BCC metals suggests that edge dislocations have high mobility compared to screws [32, 53, 80]. The high mobility of edge dislocations enables them to exit out of the crystal forming slip steps, leaving screw dislocations behind, which control the strain rate [30, 80]. The difference in mobility arises from the fact that for a dislocation to be mobile, it has to overcome the intrinsic periodic lattice resistance (Peierls potential), which is different for different dislocation types [79]. Edge dislocations have a low Peierls energy barrier compared to screws, and thus have higher mobility.

Two effects are thought to be responsible for the higher Peierls barrier in screw dislocations: the twinning/anti–twinning asymmetry, and the non-planar screw dislocation core [22]. Twinning/anti-twinning asymmetry indicates that for most BCC orientations the CRSS varies with the sense of slip, and in particular that for orientations in which the plane of maximum resolved shear stress (MRSS) is $\{2\,1\,1\}$, the CRSS for slip is lower in the twinning sense [12, 22, 91]. This asymmetry has been correlated to the energy required to displace an atom within a given slip plane in the direction of the Burgers vector [22]. This energy is visualized using a γ –surface, which is a contour map of the energy required to displace an atom from its unstressed equilibrium position to another location on the slip plane from atomistic calculations, using Finnis–Sinclair interatomic force laws [22, 28]. Figure 2.3 shows the contour maps of the γ-surfaces for the plane for the group VB metals vanadium, niobium, tantalum, and the group VIB metals chromium, molybdenum, and tungsten.

For a given slip plane, the more centro-symmetric the surface, the lesser the asymmetry between the twinning and anti-twinning sense of slip. From Fig. 2.3, it is clear that for the $\{1\,1\,0\}$ plane, Mo happens to be the least centro-symmetric while Nb happens to be much more centro-symmetric. A similar observation can be made for the $\{1\,1\,2\}$ plane, implying that the twinning/anti-twinning asymmetry is small, but existent [22]. In addition, Christian [12] reported that the tension-compression (analogous to twinning/anti-twinning) asymmetry of Nb was not evident at room temperature and only became considerable at 77 K. Baars [5] suggested that twinning/anti-twinning

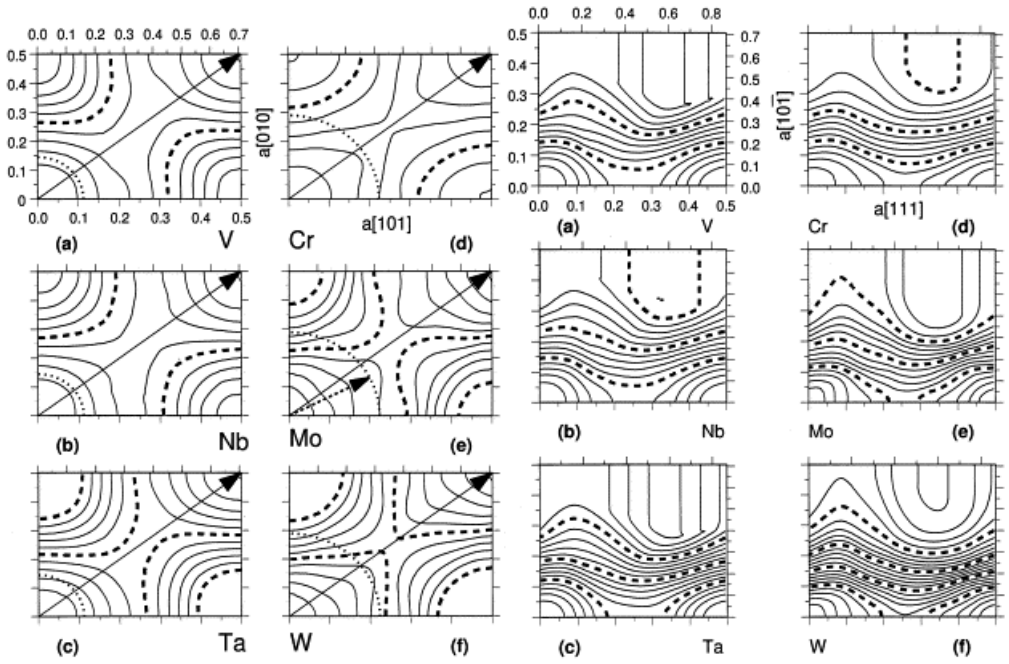

Figure 2.3 Contour maps of the $\{1\,1\,0\}$ (left) and $\{1\,1\,2\}$ (right) γ-surfaces for the plane for the group VB (Va, Nb, Ta) and the group VIB metals (Cr, Mo, W) [22].

effects in Nb may only alter the critical resolved shear stress by a small amount. Mapar [57]'s efforts to formulate non-*Schmid* effects in crystal plasticity modeling of single-crystal Nb suggested that the *Schmid* model could predict the tensile deformation of Nb better than the non-*Schmid* model. Thus, including this effect may not be necessary for practical models for the deformation of large grain Nb [5, 40, 57].

The second reason for a higher Peierls barrier observed for screw dislocation in BCC metals is the non-planar nature of the screw dislocation core structure [38, 90, 91, 95]. Empirical atomistic models have been instrumental in establishing the core structure of screw dislocations. Notably, all simulations confirmed that the screw dislocation core is non-planar in nature. Specifically, they show two possible types of equilibrium core structures in BCC metals: the compact core, which exhibits the full D3 symmetry of the $\langle 1\,1\,1\rangle$ zone, and the polarized core, which only exhibits C3 symmetry (the three-fold rotation axis) and therefore has two degenerate structures related through the $\langle 1\,1\,0\rangle$ diad [22, 94]. Weinberger et al. [94] first reported the compact core structure of Nb from DFT calculations. Furthermore, these simulations have shown that the Peierls stress of screw dislocations is high and that dislocation motion is indeed thermally activated. Unlike FCC

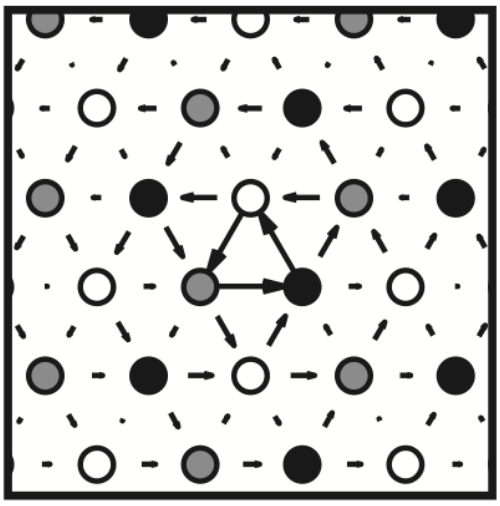

Figure 2.4 Close-up of the differential displacement map of the compact core structure observed for Nb [94].

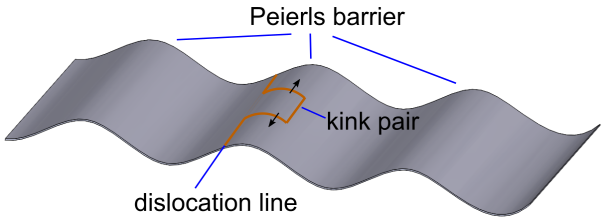

Figure 2.5 Schematic of the intrinsic periodic lattice resistance (Peierls barrier) to slip.

metals, dissociation of screw dislocations into partials has not been observed and hence no stable stacking faults have been found in BCC metals. Thus, the mechanism of slip in BCC metals is not straightforward.

Screw dislocations overcome their Peierls barrier (Fig. 2.5) by lifting a short segment of the dislocation over the barrier and letting the segments connecting the two adjacent valleys laterally relax along the Peierls hills [20, 23, 65, 79, 91, 94]. Such segments were named 'kinks' by Shockley. The kinks experience periodic potential energy variation by their position z along the hills. This position-dependent potential energy is referred to as the *Peierls* potential. In Nb, this occurs among pairs of $\frac{1}{2}\langle 1\,1\,1\rangle$ type kinks of opposite signs. Exhaustive knowledge on the formulation of

this screw dislocation mobility law in crystal plasticity modeling for Nb is provided in Chapter 4.

2.2.3 Dislocation interactions in BCC metals

Dislocation interactions are governed by the interactions of stress fields around dislocations and are generated by the distortion of the crystal lattice caused by the dislocation. In the high-temperature regime, above the so-called athermal temperature, the Peierls barriers are negligible and the dislocations have high mobility. The flow stress of BCC crystals in this case is controlled by reactions between non-coplanar dislocations. These reactions are formed for the purpose of self-energy minimization.

According to the Taylor relation, the athermal resistance to deformation stress $\tau^{\alpha}_{\text{pass}}$ is proportional to the square root of the total density of forest dislocations ρ piercing the active slip planes.

$$\tau^{\alpha}_{\text{pass}} = a\mu b\sqrt{\rho} \tag{2.1}$$

To account for the anisotropy of the interactions between slip systems, equation 2.1 is expanded as:

$$\tau^{\alpha}_{\text{pass}} = \mu b\sqrt{\sum_{\alpha'=1}^{N_s} \xi_{\alpha\alpha'}\rho} \tag{2.2}$$

where $\tau^{\alpha}_{\text{pass}}$ is the stress for activating slip system α which is determined by dislocation densities in all slip systems α' including itself. The scalar constant a is replaced by a matrix of coefficients $\xi_{\alpha\alpha'}$ such that $\sqrt{\xi_{\alpha\alpha'}}$ represents the average interaction strength between slip systems α and α'. Therefore, the total density is replaced by a sum of contributions containing the dislocation density of each slip system multiplied by its coefficient of interaction with other slip systems including itself (self-interaction). These coefficients are used to make comparisons between experimental and theoretical estimates and are calculated using Discrete Dislocation Dynamics (DDD) simulations.

Queyreau et al. [68] calculated six distinct types of BCC dislocation interactions for α-Fe. These values were generalized for all BCC materials until Madec and Kubin [55] showed that this is not necessarily true. They explained that the interaction strength between dislocations is

influenced by the "Poisson ratio" and "asymmetric junction configurations". These two effects were found to be more prominent in BCC metals than in FCC metals. In their study, strengths of dislocation interaction among $\langle 1\,1\,1\rangle\{1\,1\,0\}$ and $\langle 1\,1\,1\rangle\{1\,1\,2\}$ slip systems were determined using DDD simulations at high homologous temperatures for five BCC transition metals, including Nb.

Madec and Kubin [55] made use of Scattergood and Bacon's shear moduli and Poisson's ratios to approximate the behavior of curved dislocations in an anisotropic medium. It was inferred that the strength of junctions is mainly governed by the orientation dependence (angle between the interacting slip planes) of the line energies in BCC metals. This angle affects the magnitude of short-range interactions between dislocation segments influencing the limit between attraction and repulsion for non-coplanar dislocation reactions. The value of the Poisson ratio affects all the strengthening coefficients to various extents. Higher Poisson's ratio strengthens the collinear interactions, while lower values lead to less stable junctions due to higher line energies.

Using this theory, Madec and Kubin [55] calculated 24 different coefficients corresponding to the self-interaction (α_0'), the coplanar interaction (α_2), three collinear interactions, and twelve junctions, of which seven are doubly degenerated and five occur between $\{1\,1\,0\}$ and $\{1\,1\,2\}$ slip systems.

The different dislocation interactions in BCC metals are described as follows: The interactions between coplanar slip systems are the coplanar and self-interactions. Reactions between dislocations gliding in non-coplanar slip systems form junctions, except in the case of annihilation of two attractive dislocations gliding in two slip planes that contain their Burgers vector (the collinear interaction). There are 3 possible collinear reactions in BCC metals and 12 junction reactions. The collinear reactions are quite sensitive to the angle between slip planes. They are significantly stronger when the slip planes are perpendicular and weaker for low angle values, although they remain stronger than all junction-forming reactions [55].

Use of the newly calculated material-dependent coefficients is expected to improve the predictive ability of CP models for BCC plasticity. The interaction matrix and the coefficients for Nb are described in greater detail in Chapter 4, Section 4.4.1.

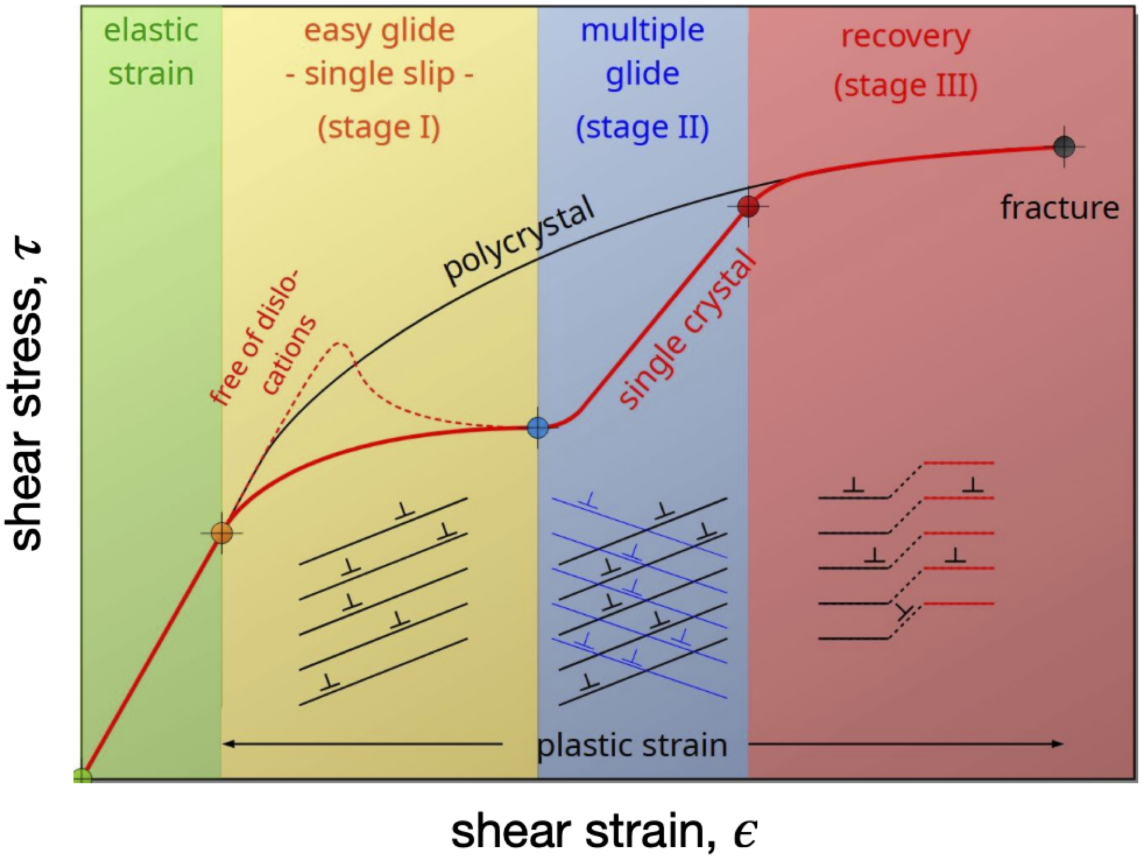

Figure 2.6 Generalized shear stress–shear strain curve of a single crystal deformed in tension showing the three stages of strain hardening [1]. Stage I, or 'easy glide' begins with a low strain-hardening rate on the primary slip system. During stage II, secondary slip systems are activated leading to an increase in strain hardening rate due to dislocation interactions. Stage III features a decreasing hardening rate with increasing flow stress due to dynamic recovery, finally leading to fracture.

2.3 Work hardening during tensile deformation in single crystals

Stress–strain curves of single crystals are often described with three hardening stages (schematic in Fig. 2.6) [16, 70].

Stage I, also known as 'easy glide', begins with a low strain-hardening rate on the primary slip system and only occurs in single crystals. In extreme cases of dislocation-free crystals, only when sufficient dislocations are present, the deformation process can be continued with lower shear stress, as indicated with a dotted red line in stage I.

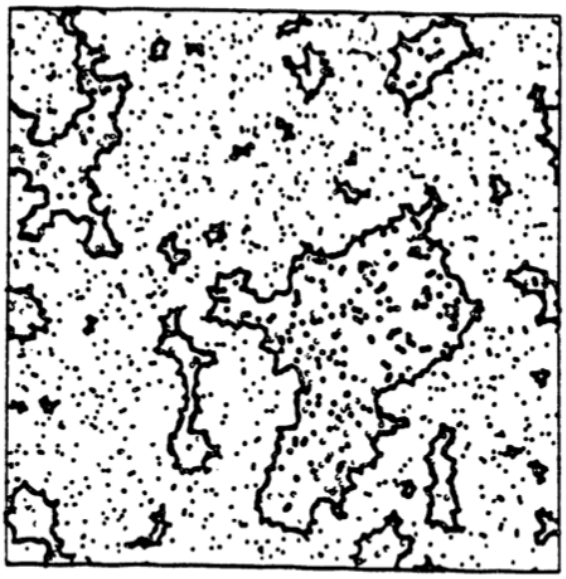

Figure 2.7 Computer simulations of dislocation glide with a random distribution of point obstacles showing glide loops that represent the interactions of forest systems with the slip plane [45, 70].

During stage II, secondary slip systems are activated leading to an increase in strain hardening due to mutual dislocation interactions and pile-ups. The dislocations produced in this stage are termed "forest" dislocations with respect to the primary slip system. The term "forest" refers to the fact the flow stress on a given plane is determined by the short-range interactions of mobile dislocations on a slip plane with those dislocations that intersect it. This is illustrated using a computer-simulated microstructure in Fig. 2.7.

Stage III features a decreasing hardening rate with increasing flow stress due to dynamic recovery [70]. Dynamic recovery refers to the loss of dislocation line length during straining, which is mainly because of the mutual annihilation of dislocations.

2.4 Overview of deformation of single crystal Nb

Early studies by Mitchell et al. [58] and Duesbery et al. [21], investigated the deformation of high purity single-crystal niobium, examining the effects of tension, compression, orientation, temperature, and strain rate on the stress–strain behavior, slip line morphology, and active slip systems.

Mitchell et al. [58] performed tensile tests at a nominal strain rate of $4.5 \times 10^{-5}\,\mathrm{s}^{-1}$ for several different single crystal orientations. There was no observation of a particular trend in the strain hardening stages. The extent of hardening stages I and II were lower for orientations closer to the $[0\,0\,1]$–$[1\,0\,1]$ symmetry boundary. Specimens on the boundary showed no stage I (easy glide), higher yield stresses, and lowest strains at failure. Ermakov et al. [27] also observed anisotropic tensile properties in the plastic regime through orientation-dependent elongation to failure. Duesbery et al. [21] observed wavy slip lines on the top face and straight slip lines on the side face of their samples suggesting that the edge dislocations travel much further than the screws, and that slip bands are formed by the double cross-slip mechanism. They observed slip traces on $\{1\,1\,0\}$ and $\{1\,1\,2\}$ planes in niobium single crystals with differences in the critical resolved shear stress (CRSS) for the two families between tension and compression.

More recently, Baars [5], Kang [40], Wang [92] conducted research with efforts to characterize the slip behavior of single crystal Nb using uniaxial in-situ tensile tests. Kang compared the deformation behavior of a set of single crystal samples in the as-received condition to the same samples after an annealing treatment of 800 °C for 2 hours, to characterize the effects of annealing on the slip behavior of single crystal Nb.

Figure 2.8 shows the tensile axis orientations of the nine samples tested. The crystal orientation of the samples along the tensile axis is indicated by letters (P–Z) in the standard stereographic triangle (SST).

Figure 2.9 shows the engineering stress–strain curves of the as-received (left) and heat-treated (right) samples. The color used for each curve is the same as the original tensile direction IPF color for that orientation. More green curves are available because many samples had tensile orientations between the center and $\langle 1\,0\,1 \rangle$ of the SST corner as can be seen in Fig. 2.8. The first and most obvious observation from these curves is that the yield and flow stresses are highly orientation-dependent. Second, flow stresses and yield strengths are consistently lower after the 2 h at 800 °C anneal. In some samples, there is no longer a slight drop in the flow stress of the annealed sample between yield and about 15 % engineering strain, which is most significantly

the case for orientation T, as seen in Fig. 2.10 This was further investigated by Wang et al. [93]. Increased strain-hardening rates for the tensile orientations closer to a boundary of the SST may suggest the activation of slip on additional planes with the same $\langle 1\,1\,1 \rangle$ directions. Figure 2.11 shows the rotation of tensile axis orientations of the as-received and heat-treated samples using an IPF. As-received samples are indicated by triangles connected with dashed lines, whereas colored dots connected by solid lines are used for the heat-treated samples. The trajectories of rotation are similar for orientation S, whereas the other orientations show varying degrees of differences between the as-received and heat-treated samples (X is an extreme). This indicates the possibility of different primary slip systems between the as-received and annealed samples, likely due to pre-existing dislocations present in the former kind.

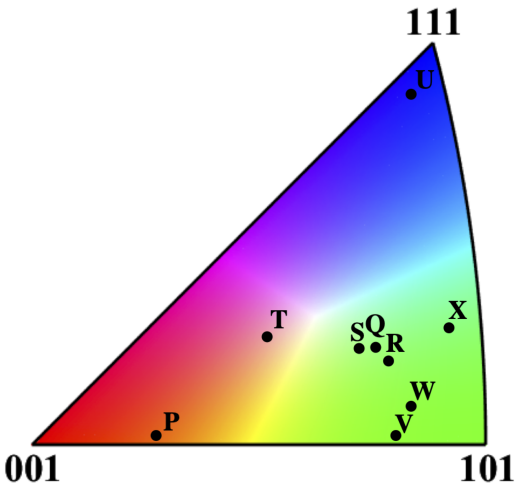

Figure 2.8 IPF showing tensile axis orientations of the nine samples used for the study by Kang et al. [41]. This figure was reproduced from [41].

Wang et al. [93] performed electron channeling contrast imaging (ECCI), slip trace analysis, and atomic force microscopy (AFM) on sample T in the undeformed and deformed conditions for both the as-received sample and the annealed sample. Observations on the undeformed as-received sample showed a high pre-existing dislocation density on certain slip systems which was characterized using ECCI. However, the characterization of dislocations on the undeformed annealed sample was difficult to perform. Post deformation ECCI and slip trace analysis on both

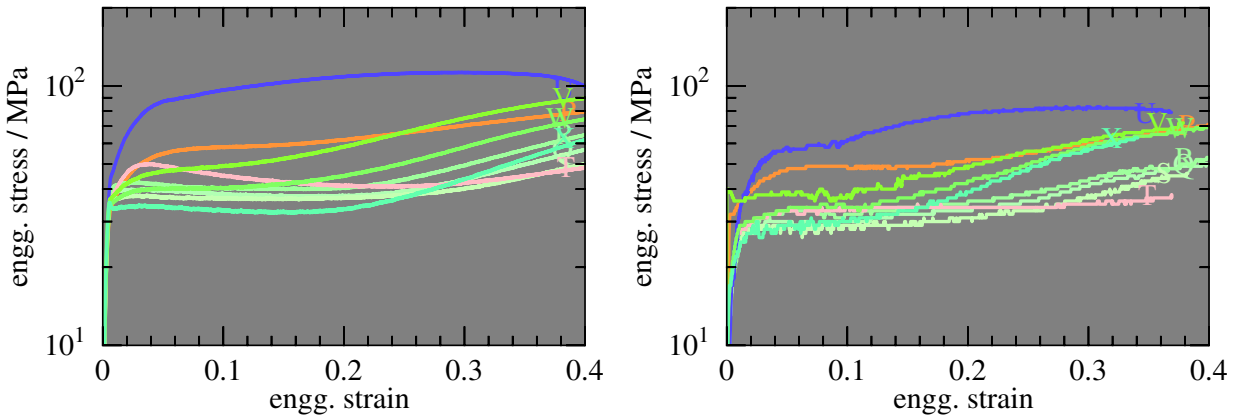

Figure 2.9 Engineering stress–strain curves of as-received (left) and annealed (right) samples. Each curve is colored by the tensile direction orientation in the inverse pole figure. This figure was replotted from the work of Kang et al. [41].

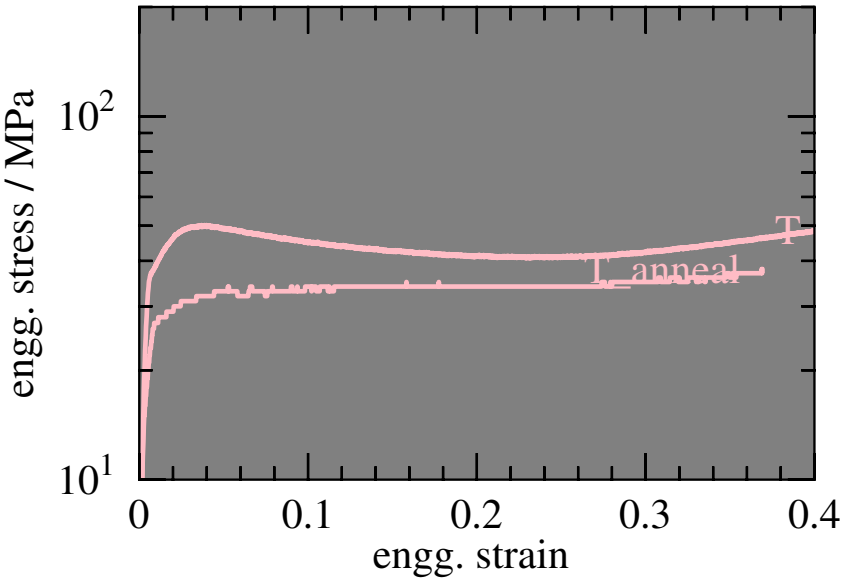

Figure 2.10 Engineering stress–strain curves of the as-received sample T showing greater yield stress and work hardening than the annealed sample. The curve is colored by the tensile direction orientation of the sample in the inverse pole figure. This figure is adopted and replotted from the work of Kang et al. [41], Wang [92], Wang et al. [93].

as-received and annealed samples showed densities on different sets of slip systems, indicating that the preferred slip planes changed from $\{1\,1\,2\}$ to $\{1\,1\,0\}$ in annealed samples, likely due to partial or complete removal of pre-existing dislocations. Slip trace observations of the as-received and annealed samples after deformation using AFM suggested that the two deformed samples ex-

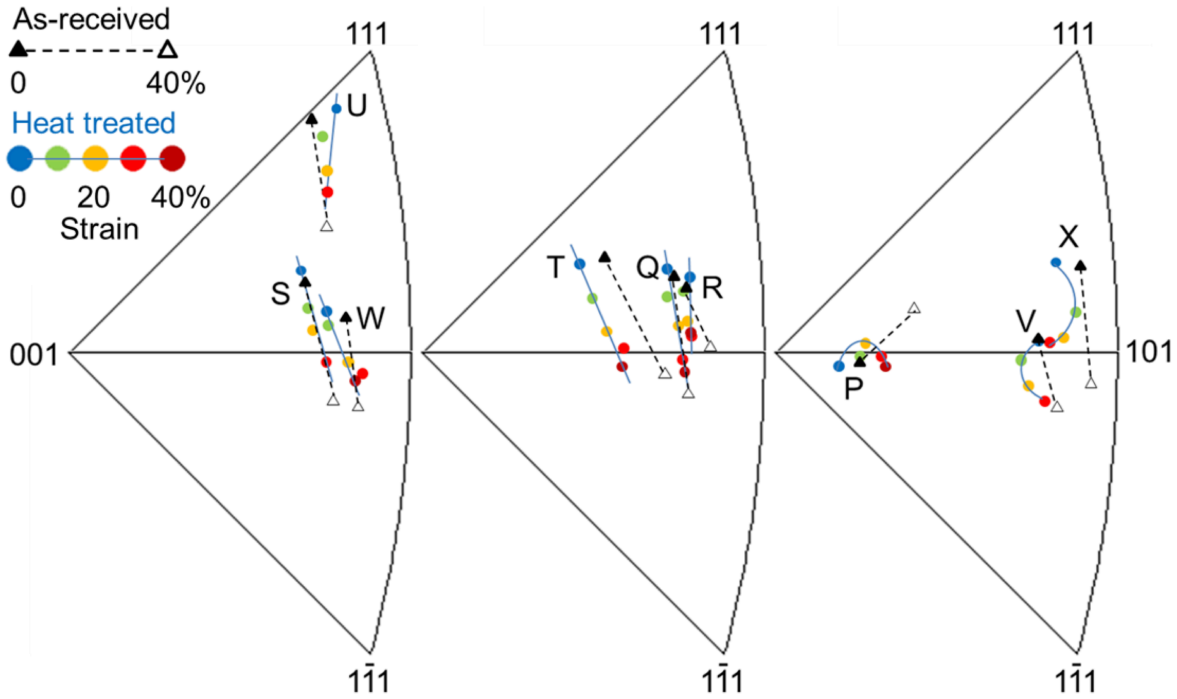

Figure 2.11 Inverse pole figures showing the rotation of the tensile axis orientations of the nine samples for both the as-received as well as the annealed condition [41]. The trajectories of rotation are similar for orientation S, whereas the other orientations show varying degrees of differences between the as-received and heat-treated samples (X is an extreme). This indicates the possibility of different primary slip systems between the as-received and annealed samples.

perienced different deformation mechanisms. The distribution of slip traces in the annealed sample after deformation was found to be more regularly spaced, suggesting more uniform deformation. However, the as-received sample showed irregularly spaced slip bands with differing amounts of slip displacement Fig. 2.12.

In Fig. 2.10, for the as-received sample, the initial flow stress increase can be related to the effect of pre-existing dislocations with lower mobilities creating forest barriers to the primary slip system. The subsequent drop in the flow stress could be explained by the development of irregularly spaced dislocation pathways resulting from overcoming dislocation entanglement barriers that may have enabled highly localized slip behavior (avalanches) between obstacles, as seen from AFM observations.

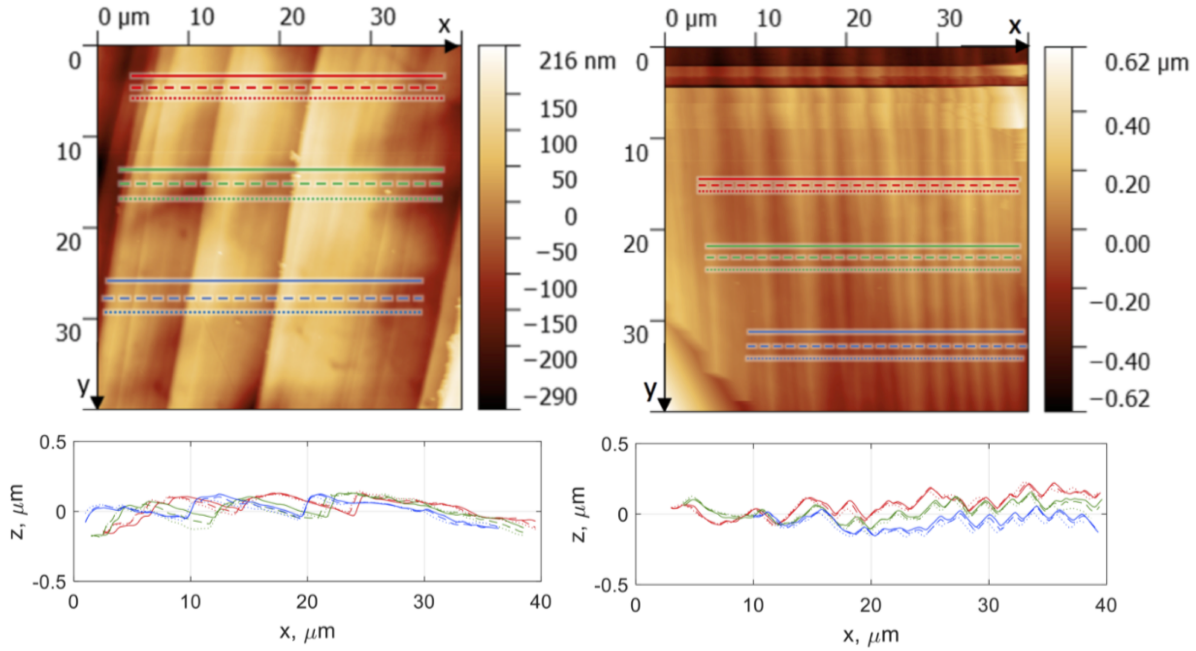

Figure 2.12 AFM topographic map (top) and surface profiles (bottom) for the as-received (left) and annealed samples(right) of orientation T [92, 93]. Widely and irregularly spaced slip steps were observed for the as-received samples and regularly spaced slip steps were observed for the annealed samples.

The conclusions from these studies suggested that the pre-existing dislocations due to prior strain history have a significant impact on which slip systems are favored to operate in single crystal samples, implying that effective crystal plasticity models must be capable of tracking the evolution of dislocation content within the material during deformation [40, 92, 93].

These insights will be useful while formulating and analyzing CP modeling simulations performed in this work.

2.5 Crystal plasticity modeling framework

A framework for simulating material deformation must include the thermodynamics and kinematics of the deformation process. The former describes the motivation for deformation while the latter deals with deformation mechanisms. Constitutive laws in crystal plasticity (CP) models take into account the effect of material anisotropy in response to an external load under applied boundary conditions, thus enabling the investigation of structure–property relationships and prediction of mechanical response. CP models have been utilized to predict a wide range of micro-mechanical phenomena ranging from strain hardening in single crystals to the mechanical response of a polycrystalline aggregate.

In this study, CP simulations are performed using the open source 'Düsseldorf Advanced Material Simulation Toolkit' (DAMASK) developed at Max-Planck-Institut für Eisenforschung GmbH (MPIE) [71–74]. Various constitutive models and homogenization schemes for crystal plasticity simulations at different length scales are available in the DAMASK software, which provides a flexible interface with commercial finite element (FE) packages such as ABAQUS and MSC.Marc. Apart from it being the material point solver (to solve constitutive field equations), DAMASK also has its own integrated boundary value solver that uses spectral methods that reduces computation time significantly compared to finite element-based solvers [17, 26, 82].

CP models in DAMASK are based on a continuum mechanical finite strain framework that describes the mechanical behavior of the body under consideration. These models also require microstructure information associated with the material of interest. The material's mechanical response is estimated by solving global equilibrium conditions. The model also incorporates a prescribed homogenization scheme such that the local equilibrium condition at each discretization point is fulfilled.

In this section, first a brief background of continuum mechanics is provided. Subsequently, the numerical methods used to solve the field equations and an overview of the types of constitutive models are introduced. However, the constitutive models used in this thesis will be detailed in Chapter 4.

2.5.1 Continuum mechanics

CP models are formulated in a continuum mechanical framework describing the mechanical behavior of a body under consideration. In continuum mechanics, the kinematics of deformation is described through various stages in the deformation history of the body or configurations. In this section, the different configurations of a body under loading are described. Using these configurations, stress and strain measures are derived.

A continuous body ($\mathscr{B}$) is a composition of infinite material points $\mathbf{x}$ with $\mathbf{x} \in \mathscr{B}$. This body assumes the region $\mathscr{B}_0$ in the undeformed or reference configuration which is time-independent. In the deformed or current state, the body occupies the region $\mathscr{B}_t$ which is time-dependent. The material points in the reference configuration are described by the vector $\mathbf{x}$ and in the current state by the vector $\mathbf{y}$. Figure 2.13 illustrates this example with the corresponding unit vectors.

In this example, the displacement $\mathbf{u}$ of a material point is calculated as the difference vector between the reference and current configurations. For a given time,

$$\mathbf{u}(\mathbf{x}) = \mathbf{y}(\mathbf{x}) - \mathbf{x} \tag{2.3}$$

A line segment d$\mathbf{x}$ in an infinitesimal neighborhood of a material point $\mathbf{x}$ in the reference configuration is transformed into the current configuration by:

$$\mathbf{y}(\mathbf{x}) + \mathrm{d}\mathbf{y} = \mathbf{y}(\mathbf{x}) + \frac{\partial \mathbf{y}}{\partial \mathbf{x}}\,\mathrm{d}\mathbf{x} + \mathscr{O}\left(\mathrm{d}\mathbf{x}^2\right) \tag{2.4}$$

Neglecting higher order terms we have:

$$\mathrm{d}\mathbf{y} = \frac{\partial \mathbf{y}}{\partial \mathbf{x}}\,\mathrm{d}\mathbf{x} = \mathbf{F}\,\mathrm{d}\mathbf{x} \tag{2.5}$$

$\mathbf{F} := \frac{\partial \mathbf{y}}{\partial \mathbf{x}}$ is called the deformation gradient and is a second-order tensor.

The graphical representation of the vectors and tensors in the different configurations is depicted in Fig. 2.13. The deformation gradient $\mathbf{F}$ maps the vector d$\mathbf{x}$ at $\mathbf{x}$ in the reference configuration to the vector d$\mathbf{y}$ at $\mathbf{y}$ in the current configuration. The deformation tensor has bases in both the reference and the current configuration, hence making it a 2-point tensor. Therefore, its inverse $\mathbf{F}^{-1}$ exists, which maps an element in the current configuration to the reference.

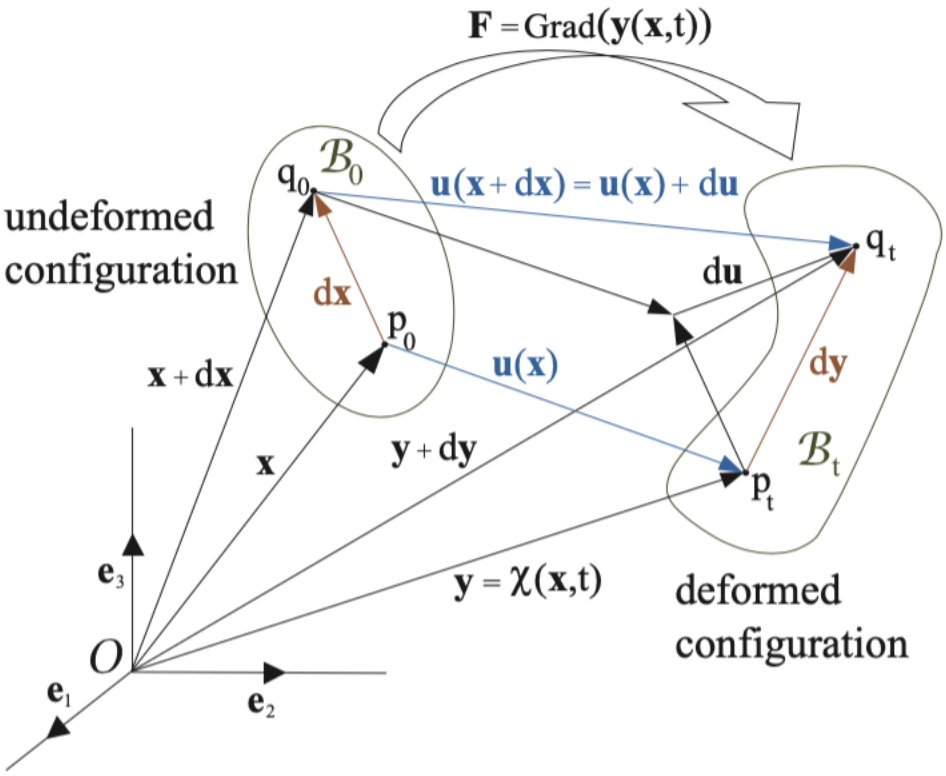

Figure 2.13 Continuum body shown in the undeformed and a deformed configuration [18]. This body assumes the region $\mathscr{B}_0$ in the undeformed configuration and $\mathscr{B}_t$ in the deformed configuration. The material points in the reference configuration are described by the vector $\mathbf{x}$ and in the current state by the vector $\mathbf{y}$. $\mathbf{u}$ is the displacement vector. The deformation gradient $\mathbf{F}$ maps the vector d$\mathbf{x}$ at $\mathbf{x}$ in the undeformed configuration to the vector d$\mathbf{y}$ at $\mathbf{y}$ in the deformed configuration.

The velocity field is defined as:

$$\mathrm{d}\mathbf{v} = \frac{\mathrm{d}\mathbf{u}(\mathbf{x})}{\mathrm{d}t} = \dot{\mathbf{u}}, \tag{2.6}$$

where $\mathbf{u}(\mathbf{x})$ is the displacement field which is a function of time. Since the points in the reference configuration move independent of time, $\dot{\mathbf{u}} = \dot{\mathbf{y}}$ holds.

The spatial gradient of the velocity field is given by :

$$Ł = \frac{\partial \mathbf{v}}{\partial \mathbf{y}} = \dot{\mathbf{F}}\mathbf{F}^{-1}. \tag{2.7}$$

Ł is the velocity gradient.

The deformation gradient can be decomposed into components of pure stretch and pure rotation

as:

$$\mathbf{F} = \mathbf{V}\mathbf{R} = \mathbf{R}\mathbf{U}, \tag{2.8}$$

where $\mathbf{R}$ is the rotation tensor, and $\mathbf{V}$ and $\mathbf{U}$ are the left and right stretch tensors, respectively. Such a polar decomposition can be used to validate a strain measure. Strain in the reference configuration is expressed as the Green–Lagrange strain tensor,

$$\mathbf{E} = \left(\mathbf{F}^{\mathrm{T}}\mathbf{F} - \mathbf{I}\right)/2 \tag{2.9}$$

Strain in the current configuration is expressed as the Euler–Almansi strain tensor,

$$\mathbf{e} = \left(\mathbf{I} - \mathbf{F}^{-\mathrm{T}}\mathbf{F}^{-1}\right)/2 \tag{2.10}$$

Similar to strain measures there is a distinction between stress measures in the different configurations. Stress in the current (deformed) configuration is expressed using the symmetric Cauchy stress tensor σ and is defined as the force acting on an infinitesimal area in the current configuration. The second Piola–Kirchhoff stress tensor, $\mathbf{S}$ is the stress in the reference configuration.

$$\mathbf{S} = \mathbb{C}\mathbf{E} \tag{2.11}$$

where $\mathbb{C}$ is the fourth-order stiffness tensor.

All components of the Cauchy stress tensor for every material point must satisfy the following condition for a body in static equilibrium:

$$\sigma_{ij,j} = 0 \tag{2.12}$$

which in finite-strain theory is expressed as:

$$0 = \boldsymbol{\nabla} \cdot \mathbf{P} \tag{2.13}$$

where $\mathbf{P}$ represents the non-symmetric first Piola–Kirchhoff stress tensor.

With this brief continuum mechanical overview, the crystal plasticity framework is explained next.

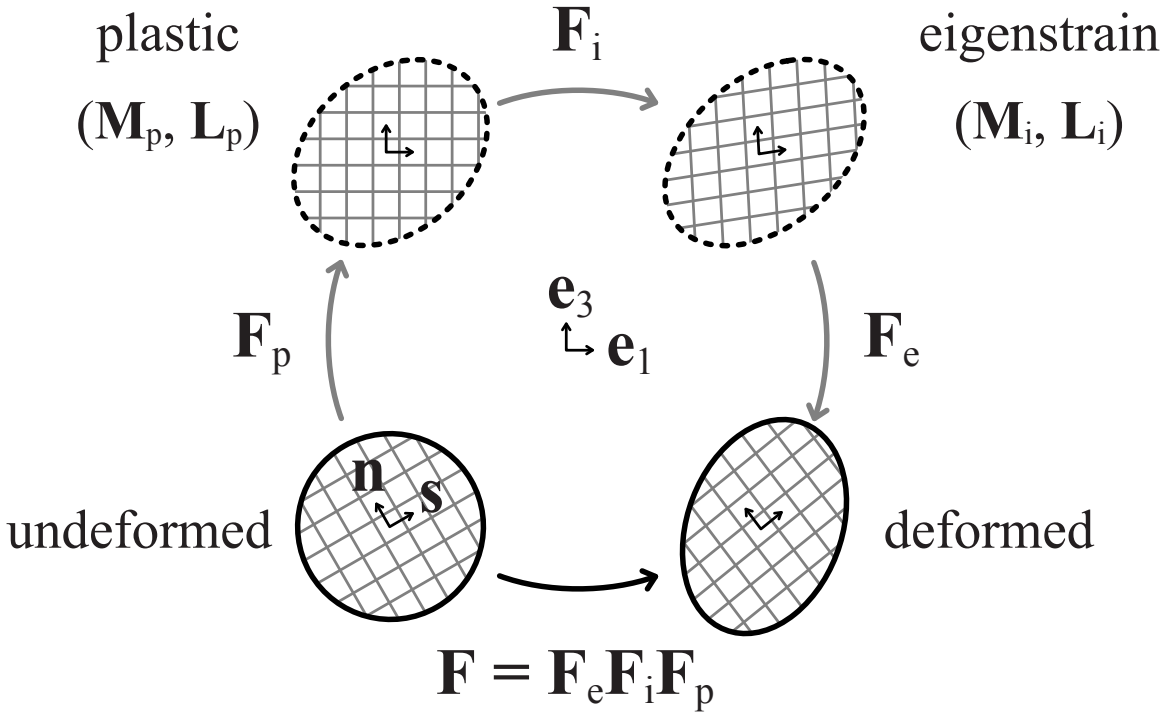

Figure 2.14 Multiplicative decomposition of deformation gradient resulting in intermediate configurations [74].

2.5.2 Numerical framework

The numerical framework of DAMASK is based on the multiplicative decomposition of the deformation gradient $\mathbf{F}$ into a lattice-preserving plastic deformation gradient $\mathbf{F}_\mathrm{p}$, lattice-distorting inelastic 'eigenstrain' deformation gradient $\mathbf{F}_\mathrm{i}$, and the elastic deformation gradient $\mathbf{F}_\mathrm{e}$, expressed as:

$$\mathbf{F} = \mathbf{F}_\mathrm{e}\,\mathbf{F}_\mathrm{i}\,\mathbf{F}_\mathrm{p} \tag{2.14}$$

The plastic deformation gradient $\mathbf{F}_\mathrm{p}$ maps the undeformed configuration to the deformed configuration which conserves volume. $\mathbf{F}_\mathrm{i}$ maps the intermediate volume non-conserving configuration that can accommodate stress-free strains ('eigenstrains') such as thermal strains or chemical strains. $\mathbf{F}_\mathrm{e}$ maps the inelastic to the deformed configuration. This decomposition is schematically shown in Fig. 2.14.

The constitutive laws are formulated using rate form, requiring time integration of the kinematic quantities from t_0 to $t = t_0 + \Delta t$ For a given input measure of deformation gradient $\mathbf{F}$, the

steps followed by the material solver in DAMASK to evaluate a consistent value of stress for each material point are illustrated in Fig. 2.15 and outlined below:

The evolution of the inelastic deformation gradients $\mathbf{F}_\mathrm{p}$ and $\mathbf{F}_\mathrm{i}$ is given in terms of their respective velocity gradients $\mathbf{L}_\mathrm{p}$ and $\mathbf{L}_\mathrm{i}$ by the flow rules:

$$\dot{\mathbf{F}}_\mathrm{p} = \mathbf{L}_\mathrm{p}\mathbf{F}_\mathrm{p} \tag{2.15a}$$

$$\dot{\mathbf{F}}_\mathrm{i} = \mathbf{L}_\mathrm{i}\mathbf{F}_\mathrm{i} \tag{2.15b}$$

The inelastic velocity gradients are additively composed of individual contributions (indexed by n) and are driven by the second Piola–Kirchhoff stress $\mathbf{S}$:

$$\mathbf{L}_\mathrm{p} = \sum_n f_n(\mathbf{S}_\mathrm{p}, ...) \tag{2.16a}$$

$$\mathbf{L}_\mathrm{i} = \sum_n f_n(\mathbf{S}_\mathrm{i}, ...) \tag{2.16b}$$

where $\mathbf{S}$ is obtained from the elastic constitutive equation defined in Eq. (2.11).

Equation (2.15) is integrated over the time integral Δt, resulting in :

$$\mathbf{F}_\mathrm{p}(t) = \mathbf{F}_\mathrm{p}(t_0) + \int_{t_0}^{t} \mathbf{L}_\mathrm{p}(\tau)\mathbf{F}_\mathrm{p}(\tau)\mathrm{d}\tau = \exp\left[\int_{t_0}^{t} \mathbf{L}_\mathrm{p}(\tau)\mathrm{d}\tau\right]\mathbf{F}_\mathrm{p}(t_0) \tag{2.17a}$$

$$\mathbf{F}_\mathrm{i}(t) = \mathbf{F}_\mathrm{i}(t_0) + \int_{t_0}^{t} \mathbf{L}_\mathrm{i}(\tau)\mathbf{F}_\mathrm{i}(\tau)\mathrm{d}\tau = \exp\left[\int_{t_0}^{t} \mathbf{L}_\mathrm{i}(\tau)\mathrm{d}\tau\right]\mathbf{F}_\mathrm{i}(t_0) \tag{2.17b}$$

Equations (2.15) to (2.17) are solved numerically.

The velocity gradient time integrals are approximated implicitly as:

$$\frac{\mathbf{F}_\mathrm{p}(t) - \mathbf{F}_\mathrm{p}(t_0)}{\Delta t} = \mathbf{L}_\mathrm{p}(t)\,\mathbf{F}_\mathrm{p}(t) \tag{2.18a}$$

$$\frac{\mathbf{F}_\mathrm{i}(t) - \mathbf{F}_\mathrm{i}(t_0)}{\Delta t} = \mathbf{L}_\mathrm{i}(t)\,\mathbf{F}_\mathrm{i}(t) \tag{2.18b}$$

$\mathbf{F}_\mathrm{e}$ can be then calculated from Eq. (2.14) whose solution would then provide a stress state satisfying the multiplicative decomposition and the constitutive laws for the respective velocity gradients, represented as generic functions in Eq. (2.16).

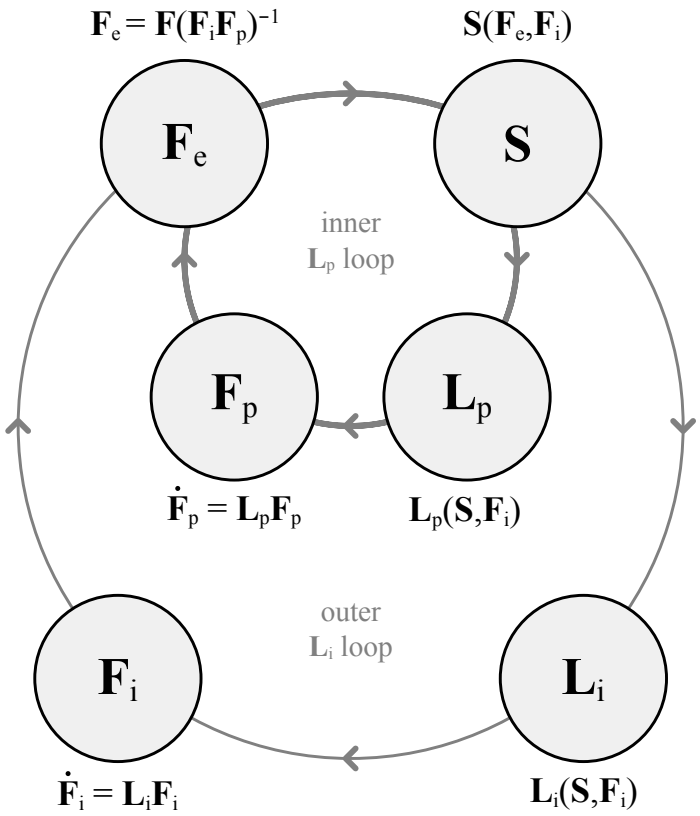

Figure 2.15 Schematic of the solution procedure for the kinematic quantities adopted in DAMASK [74].

The residuals resulting from the solution of coupled equations are minimized using a modified Newton–Raphson scheme with a variable step length until a consistent solution is obtained, within a staggered iterative loop [74, 82]. Convergence of the Newton–Raphson scheme is achieved when the residual drops below a given tolerance.

The advantage of formulating the problem as a residual minimization is the use of open source solvers such as Portable Extensible Toolkit for Scientific Computation (PETSc) which contains numerical algorithms to solve systems of linear or non-linear equations in the most efficient way [2]. The spatial gradients of the mechanical field quantities are calculated using the forward-backward finite difference variant introduced by Schneider et al. [76], Willot [96] that reduces the frequently observed fluctuations in the results (also known as the "Gibbs phenomenon"). The microstructural state integration is done using an implicit fixed point iterative scheme introduced by Kalidindi et al. [39].

The boundary value problem is numerically solved using one of the many existing techniques. The most common methods of solving such static equilibrium problems is using Finite Element Method (FEM) [13, 98] or through spectral methods using Fast Fourier Transform (FFT) introduced first by Moulinec and Suquet [59] and improved by De Geus et al. [15], Eisenlohr et al. [26], Kaßbohm et al. [42], Lebensohn [49], Spahn et al. [83], Willot [96]. The key difference between the two methods is that, in FEM, the solution of the field equation is approximated by local shape functions (lower-order polynomials) that are non-zero in a finite domain ("element") and are then summed to get the total approximate (weak form) solution, while the spectral FFT methods approximate the whole domain by one large set of basis functions [82]. The FEM method has been the most popular in solving micromechanical field equations due to its feasibility to solve systems having complex geometries and boundary conditions while the spectral FFT-based method is best used in periodic systems. DAMASK has been coupled to the commercial FEM packages MSC.MARC and ABAQUS (explicit and implicit) using their respective user subroutine interfaces. For the FFT-based spectral solver used for the simulations in this work, the static equilibrium equation is solved using the direct variational formulation originally introduced by [26] and later modified by [81] using the "basic" scheme. which is a collocation-based approach at the grid points [26].

2.5.3 Constitutive modeling

A constitutive model relates the response of the material to an external load i.e. it relates stress to strain. This relation is necessary to complement the static mechanical equilibrium and the strain compatibility condition. In comparison to general constitutive models, crystal plasticity models take into account the anisotropic mechanical response of crystalline materials.

Constitutive laws depend on the crystal structure and the type of deformation kinetics. In general, constitutive models are composed of three parts,

- microstructure parameterization
- structure evolution
- rate of deformation/kinetics

The microstructure parameterization part distinguishes between isotropic and non-isotropic plastic deformation. Structure evolution, which is a function of the current microstructure and stress state at each point, describes the change of microstructure parameters during deformation, which results in hardening. The deformation kinetics describes the rates of shear at each point. The combination of all three parts as coupled ordinary differential equations (ODEs) at each point makes up the constitutive law.

Each constitutive law is internally parameterized by a set of state variables. The choice of these variables is related to the degree of sophistication of the constitutive law. This can range from empirical descriptions, which are computationally efficient yet limited in accuracy, to physics-based descriptions with higher computational demands and accuracy. Empirical models such as the "*Pheomenological Material Model*" rely solely on data fitting. Physics-based models such as the "*Dislocation density based model*" have parameters that are determined by lower scale simulations or direct experimental observations.

A thorough description of the CP models available in DAMASK can be found in [74]. A presentation of the exact CP models used in this work is outlined in Chapter 4.

In summary, to fulfill the need for better predictive material models that track microstructure evolution during SRF cavity processing, plastic deformation mechanisms in Nb is surveyed. Single-crystal deformation experiments and their corresponding crystal plasticity simulations are paramount to fulfill knowledge gaps that exist for exploring the large-grain approach to SRF cavity forming. The primary objective of this thesis is to develop a dislocation mechanics-based crystal plasticity model that incorporates thermally activated kinetics of dislocation motion and the effects of their mutual interactions, with the goal to achieve predictability and microstructure control. This is formulated for pure Niobium for the purpose of predicting slip activity and the associated strain-hardening and lattice reorientations using single-crystal simulations. Findings from this study aim to supplement prior knowledge discussed above and provide insights into the feasibility of the large-grain approach to SRF cavity forming. Effect of initial conditions such as pre-existing dislocation density distribution will be investigated to better understand their influence on the certainty

unique slip activity in single crystals. These influences may suggest to consider any further improvements in the constitutive description and parameter optimization only after quantifying the uncertainty that they pose on predictability.

CHAPTER 3

TENSILE MECHANICAL PROPERTIES OF SINGLE CRYSTAL NB

This chapter presents an experimental study of the tensile mechanical properties of high-purity niobium single crystals.

This study was a part of a collaboration with I-Cube research, Toulouse, France intended to investigate the tensile mechanical properties of Nb single crystals [14]. The original proposal was aimed towards measuring and analysing the mechanical properties of Nb at higher strain rates to explore electro-hydraulic forming, a high-velocity technique of forming large-grained Nb disks into SRF cavities for particle accelerators [14]. However, this study presented an opportunity to also perform quasi-static tensile tests, which would stand as a valuable source of data for validating constitutive models for Nb. Uniaxial tension tests performed in the study were performed at several different strain rates between $1.3 \times 10^{-4}\,\mathrm{s}^{-1}$ and $10^{3}\,\mathrm{s}^{-1}$. However only tests at strain rates below $1 \times 10^{-1}\,\mathrm{s}^{-1}$ are referenced in this thesis.

Single crystals have the potential to offer a better picture of deformation mechanisms because they are largely free of three-dimensional microstructural features such as grain boundaries and triple junctions. In this work, single crystal specimens of different crystallographic orientations cut from a large-grained niobium disk were deformed in uniaxial tension at various strain-rates [14]. A strategic set of single crystal orientations that have the potential to provide interesting insights on slip system activity were selected for these experiments [14]. Insights from this work are valuable in understanding the anisotropic nature of the single crystal mechanical behavior and can be used to guide crystal plasticity modeling efforts.

3.1 Materials and methods

3.1.1 Nb disk measurements

A large-grained high-purity Nb disk measuring 322 mm in diameter and 3.8 mm in thickness was used for this study. This disk was sourced from the European Organization for Nuclear Research (CERN) and had a residual resistivity ratio (RRR) greater than 300, implying that the ingot

had been electron beam melted multiple times to purify it. The large grains are sections of long columnar grains such that multiple slices have the same orientations and nearly the same grain shapes. Single-crystal specimens were cut by electron discharge machining (EDM) from the ten largest grains as seen in Fig. 3.2.

3.1.2 Orientation measurement

Measurement of crystallographic orientation of the ten grains from which specimens were cut was performed by former student Di Kang at Michigan State University using a non-destructive Laue X-ray diffraction method. A Photonic Science Laue X-ray Imaging System by Microphotonics Inc. was used for this purpose. The Laue method was more practical for measuring ingot slices rather than using the conventional Electron Back Scattered Diffraction (EBSD) technique that is more commonly used for texture measurements in smaller specimens. The Laue back-reflection technique was used to measure the large grained Nb disk. In this technique, a beam of white radiation from an X-ray source shines on a sample which is then diffracted according to Bragg's law. The rays diffracted backwards are recorded on the image plate of an area detector forming diffraction spot patterns. Figure 3.1 shows a schematic of the Laue diffraction back-reflection technique. These diffraction patterns are measured and indexed to determine the orientation of each grain. Each spot on the diffraction pattern can be attributed to a specific plane in the crystal. The crystal orientation is determined by indexing the position the spots in the pattern Measurements were performed at multiple locations in the largest grains (illustrated in Fig. 3.2) to assess whether orientation gradients were present. For more information on the Laue diffraction tool and the software used for indexing the patterns, please refer to details in [41].

Additional measurements were performed on the adjacent disk extracted from the same ingot, which confirmed the identical grain orientations in the two disks. An average difference in Bunge Euler angles of 0.3°, 0.2 ± 0.2 and 0.9 ± 0.4 for ϕ_1, Φ, and ϕ_2, respectively, was measured between the two disks, for three locations, which is consistent with the angular resolution limits of the method.

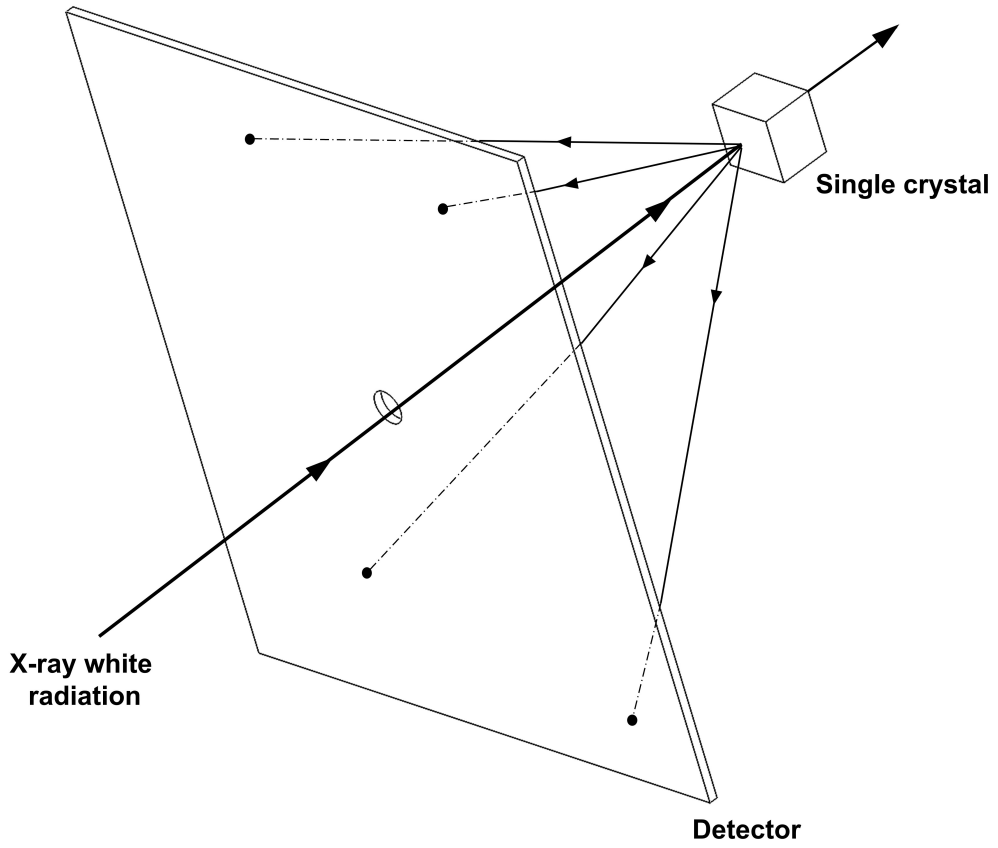

Figure 3.1 Schematic of the Laue back-reflection technique for measuring single crystal orientations.

3.1.3 Selection of tensile orientations

In order to formulate a systematic way to measure the mechanical properties of different crystal orientations, a software toolbox based on Schmid law, which determines the slip plane with direction **m** and plane normal **n** which resolves the most amount of shear during loading, was constructed. This toolbox aided the selection of strategic tensile orientations based on active slip systems visualized in the form of inverse pole figures (IPFs) containing the tensile orientations.

The toolbox algorithm works as follows:

- First, the Schmid factor (SF) of the 24 slip systems in the $\{1\,1\,0\}\langle 1\,1\,1\rangle$ and $\{1\,1\,2\}\langle 1\,1\,1\rangle$ families were calculated for each grain in all possible in-plane tensile orientations.
- Next, the ratio of the highest SF to the second highest SF value was calculated for each orientation and the corresponding competing slip families were visualized using a color code

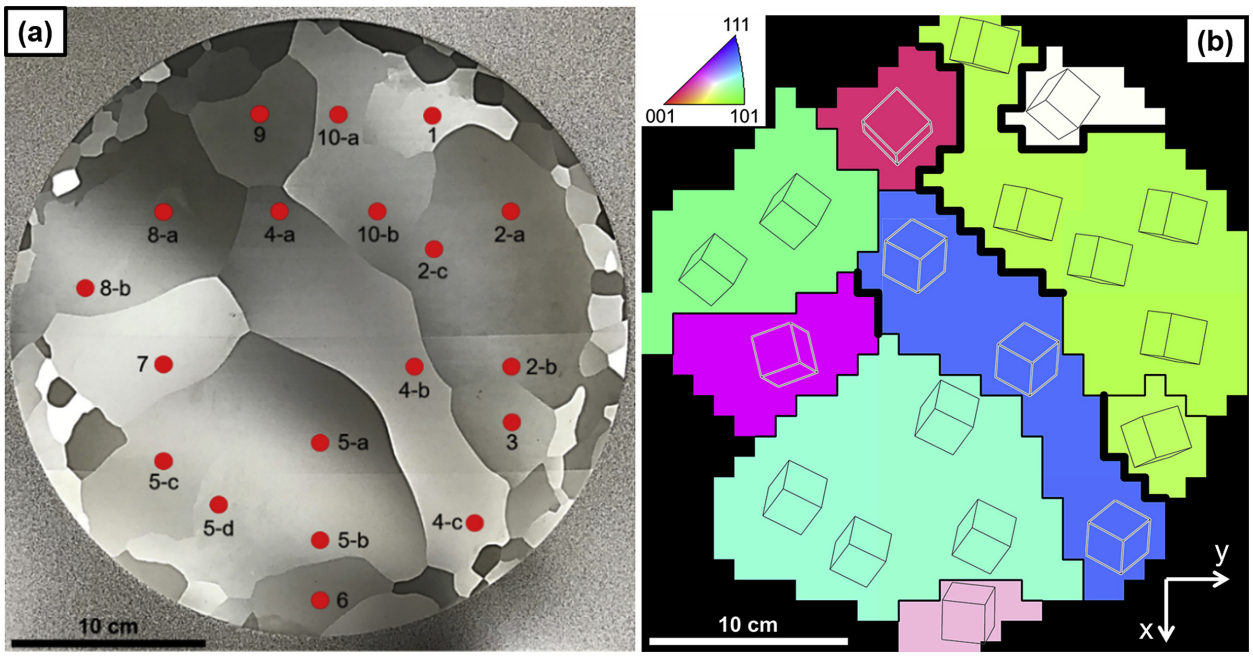

Figure 3.2 (a) Large-grained Nb disk used for the study with red points indicating locations of orientation measurement and (b) normal direction orientation map of the 10 grains with unit cells showing crystal orientation; heavy lines identify coincidence site lattice (CSL) boundaries, and reference x and y directions are labeled.

system.

- Finally, the strength of the competition between the two dominating slip families was visualized by incorporating a color gradient system in addition to a color code. This means, as the color gradient changes from dark to white, the relative preference for the system with higher Schmid factor decreases from stronger to equal.

Specimen orientations were selected based upon 5 different conditions:

1. High and dominant SF in the $\{1\,1\,0\}$ system.
2. High and dominant SF in the $\{1\,1\,2\}$ system.
3. Competing high SF for both systems.
4. Low SF for both systems.
5. Orientations close to symmetry boundaries in their tensile direction inverse pole figures.
6. Reproducibility of properties from adjacent samples with the same tensile direction, as well as nominally the same tensile axis obtained in different grains.

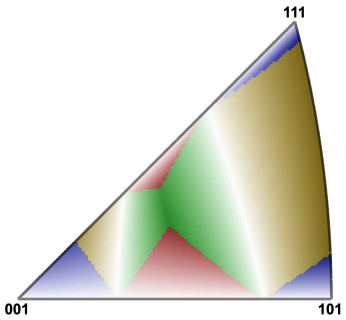

Color	SF1	SF2
red	$\{1\,1\,0\}$	$\{1\,1\,0\}$
green	$\{1\,1\,0\}$	$\{1\,1\,2\}$
blue	$\{1\,1\,2\}$	$\{1\,1\,0\}$
gold	$\{1\,1\,2\}$	$\{1\,1\,2\}$

Figure 3.3 Inverse pole figure (IPF) of in-plane tensile orientations visualizing their most active slip family pairs as the ratio of their Schmid factors. Color code SF1 and SF2 indicate the families of the slip systems with highest and second-highest Schmid factors respectively. As the color gradient changes from dark to white, the relative preference for the system with higher Schmid factor decreases from stronger to equal.

The above outlined idea to select specimen orientations, was not fully realised. This was because the reference coordinate frame used to plot potential tensile orientations was not the same as the one used to measure the grain normal orientations shown in Fig. 3.2. The correct coordinate system should have had the rolling direction (RD), defined as A1, pointing south (downward) and the transverse direction (TD), A2, pointing east (right). The assumed coordinate system however, was wrong by 90°. The consequence of this error is shown in Fig. 3.4. The assumed coordinate system led to a different orientation set as the actual outcome. Although the actual outcome did not have all the orientations that were expected, due to the large sample set involved in the design, there were still specimens in most regions of the IPF, but no orientations close to $[1\,0\,1]$ and $[1\,1\,1]$ which was originally planned.

Figure 3.5(a) shows the layout of orientations of all cut specimens. The larger dogbones were the samples used for quasi-static tension tests. The smaller dog-bones and the cylindrical samples were used for high-strain rate tension tests and compression tests, which are not a part of this thesis. The coloring of each specimen represents the crystallographic direction parallel to the tensile/compression axis in accordance with the IPF shown in the top right corner of the figure. The use of color helped in identifying specimens with similar loading orientations obtained from

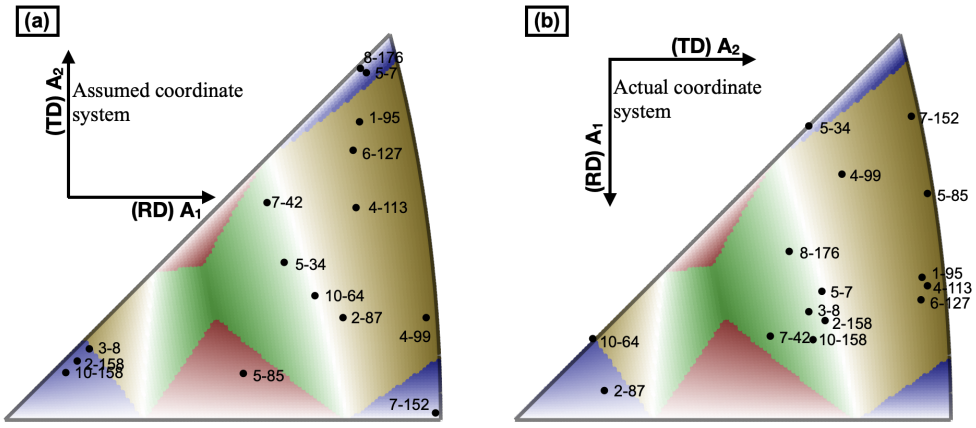

Figure 3.4 Comparison of (a) the tensile orientations intended for the investigation and (b) the actual outcome of tensile orientations due to the confusion of the orientation reference frame.

different grains (having different cutting angles). Figure 3.5(b) shows the tensile axis crystallographic directions of the specimens (black markers) on the IPF. The specific selection of orientations includes multiple specimens for the five conditions previously described. The specimen nomenclature used throughout this chapter and the rest of the thesis is grain number-rotation angle, e.g. 4-113 stands for grain 4 and a 113° counter-clockwise rotation angle from the horizontal axis of the disk.

3.1.4 Sample geometry

All specimens were cut using wire electrical-discharge machining (EDM). This technique was preferred to reduce specimen work hardening, waste, and for its high accuracy. Tensile specimens were later cut in half through their thickness using the same technique to double the number of specimens available for testing. The resulting average thickness was (1.76 ± 0.25) mm. The geometry and dimensions of the specimens used for the quasi-static tension tests is illustrated in Figure 3.6. This design is based on the ASTM E8 subsize specimen and is further miniaturized by a factor of approximately two.

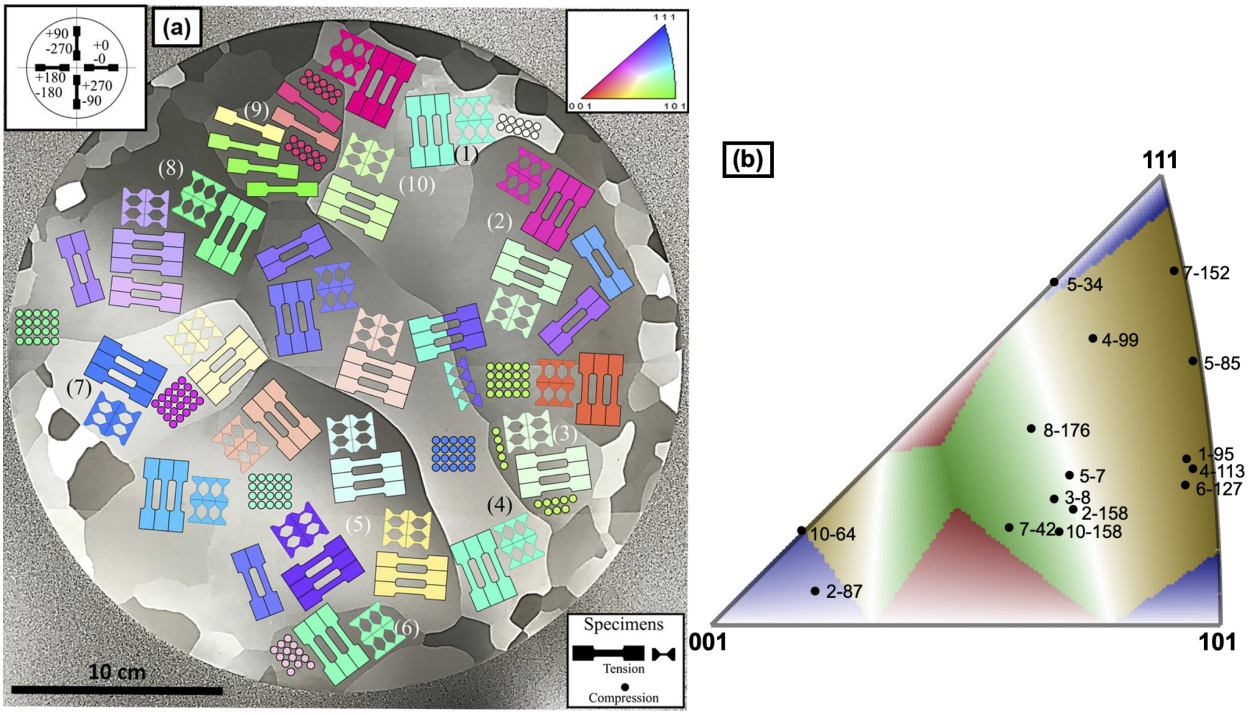

Figure 3.5 (a) Layout of test specimens (only larger dog-bones are a part of this work) and (b) inverse pole figure (IPF) of the tensile axis (black markers) of all the specimens studied in quasi-static tension.

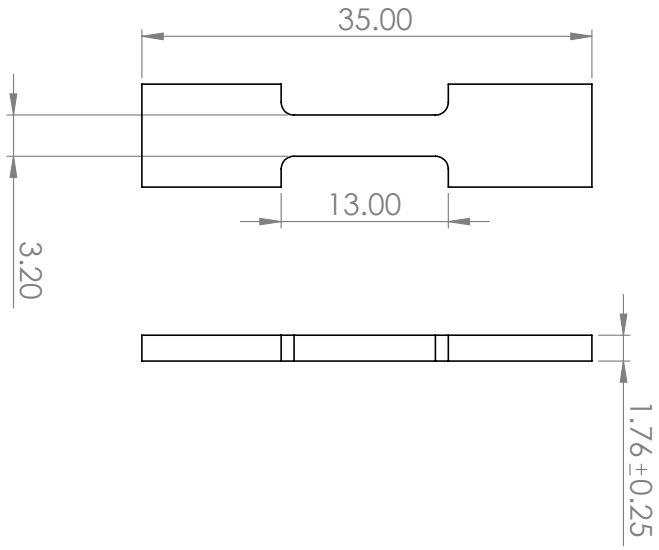

Figure 3.6 Geometry and dimensions (in mm) of the tensile dog-bone specimens.

3.1.5 Quasi-static tensile tests

Quasi-static (QS) tensile tests were performed at room temperature and at constant cross-head speeds of 0.1, 1, 10, 50, and 100 mm min^{-1}, resulting in nominal strain rates of 1.3×10^{-4}, 1.3×10^{-3}, 1.3×10^{-2}, 6.4×10^{-2}, and 1.3×10^{-1} s^{-1} respectively, using a screw-driven table-top universal testing machine (Instron 4302) at MSU. A modulus correction was used to correct for the stiffness of the machine and the grips from the measured cross-head displacement.

3.2 Results and Discussion

3.2.1 Effect of orientation

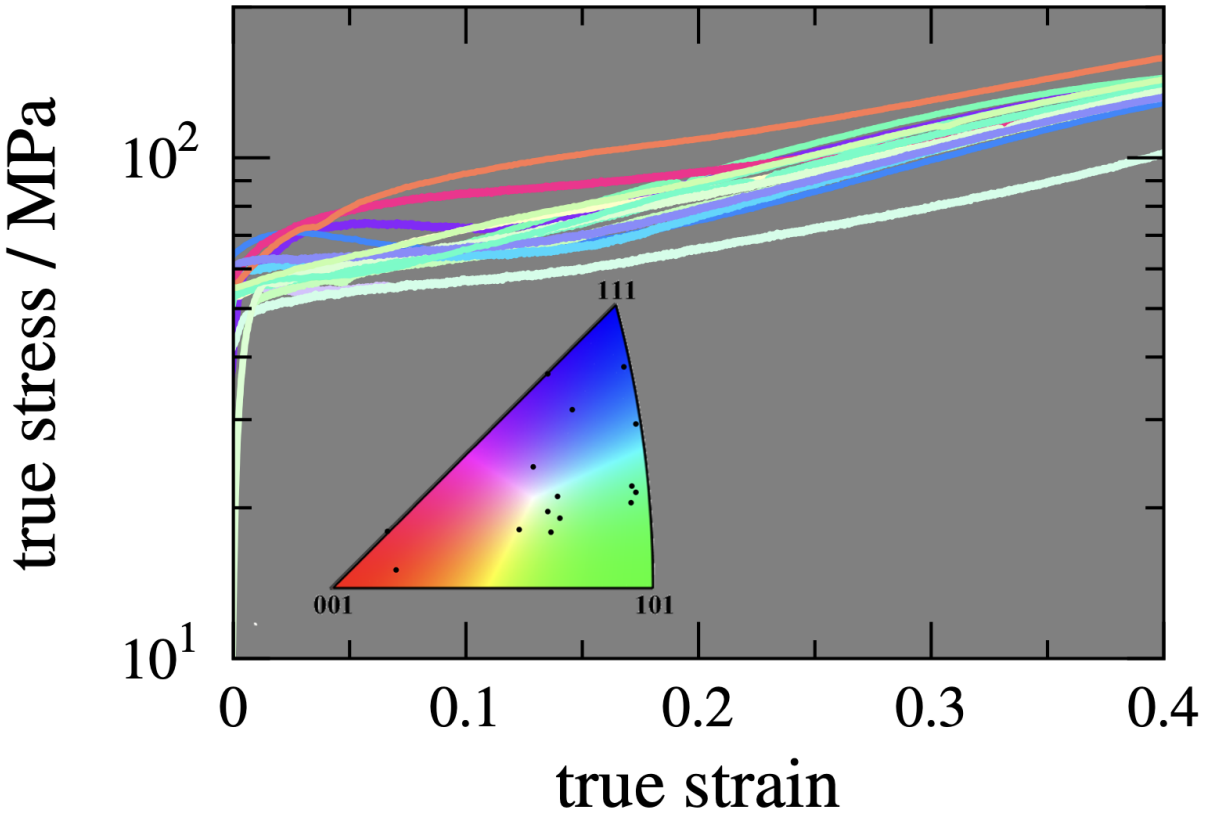

Figure 3.7 True stress–strain curves of tensile specimens colored by initial crystallographic tensile axis (see IPF inset).

Figure Figure 3.7 shows the true stress–strain curves of all the samples tested at the rate of 1.28×10^{-3} s^{-1}. Each curve is colored by the specimen's tensile axis IPF color presented for reference in the figure's inlet. The background color of the figure is gray for for easier visual

resolution of orientations with lighter colors.

Large differences in the yield stress and strain–hardening hardening behavior, indicating a strong dependence on the crystallographic tensile direction. For most orientations, yield is succeeded by a distinct hardening followed by a decrease in flow stress, giving rise to a "bump" in the stress–strain curve. From prior work by Kang [40], Wang et al. [93], this peculiarity can be connected to pre-existing dislocation populations.

3.2.2 Reliability of testing

In order to validate that the testing was reproducible, a minimum of two tests were performed for each orientation. Figure 3.8 shows the true stress–strain curves of quasi-static tensile orientations tested at $1.28 \times 10^{-3}\,\mathrm{s}^{-1}$. The yield stress and strain hardening for stage I and stage II are identical for repeat samples. This shows that the testing methods and material variability was reliable and reproducible.

Additionally, it was established that similar tensile orientations derived from different grains (and different cutting angles) showed similar stress–strain behavior in tension. Figure 3.9 demonstrates that specimens 2-158 and 3-8 are similar tensile orientations, although cut from different grains. They also exhibit the same properties in tension.

3.2.3 Effect of strain rate

The effect of strain rate on crystals with tensile directions near the center of the tensile axis IPF (crystals 2-158 and 3-8), for four different quasi-static strain rates of 1×10^{-4}, 1×10^{-3}, 1×10^{-2}, 0.5×10^{-1}, and $1 \times 10^{-1}\,\mathrm{s}^{-1}$ is compared in Figure 3.10. Because the two orientations are very similar, results for both crystals are presented on the same plot to determine the strain rate sensitivity. The yield stress systematically increases with increasing strain-rate. The elongation to failure is maximum at the strain rate of $0.5 \times 10^{-1}\,\mathrm{s}^{-1}$and drops for the strain rate of $1 \times 10^{-1}\,\mathrm{s}^{-1}$.

3.2.4 Post deformation re-orientation

For sample 5-34 and 8-176, EBSD measurements using SEM were performed on polished cross-sections to measure the change in crystal tensile orientation between the undeformed grip

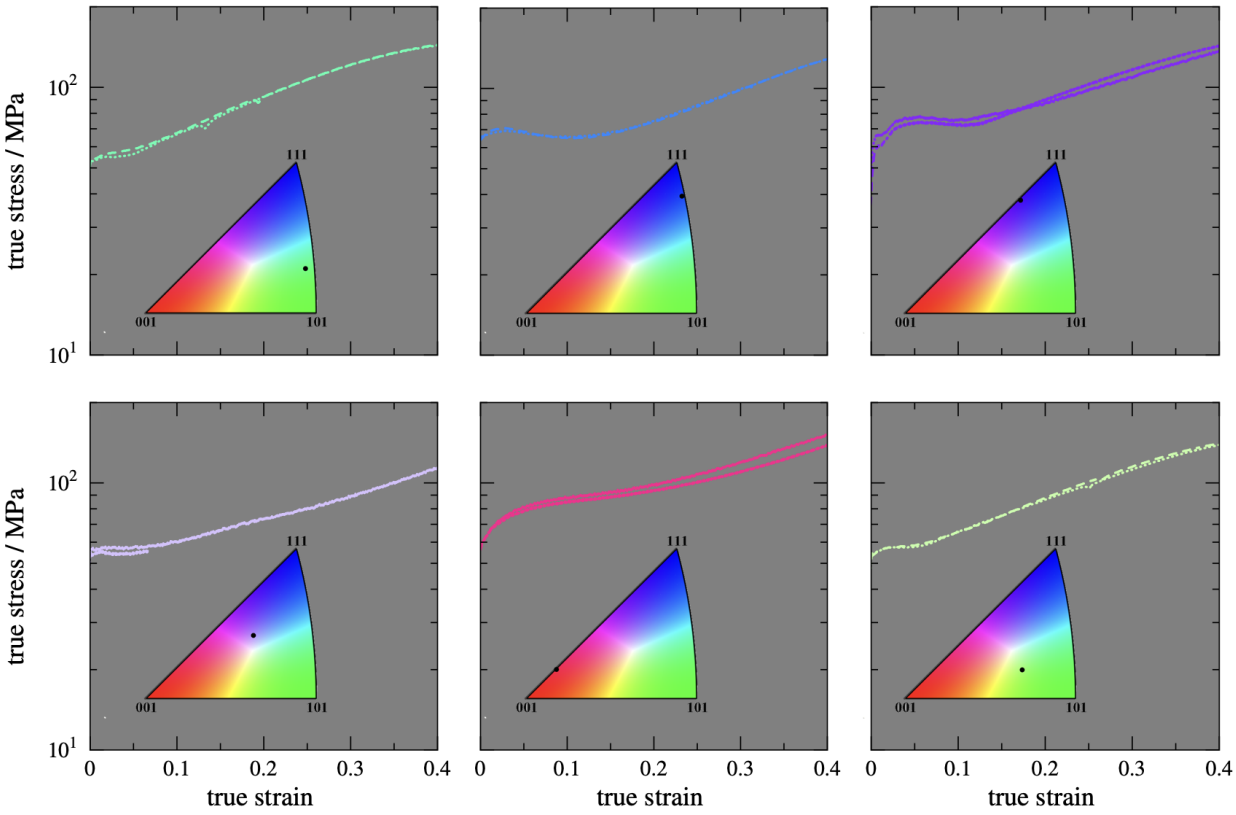

Figure 3.8 True stress–strain curves of quasi-static tensile orientations tested at 1.28×10^{-3} s^{-1}. Two samples were tested for each orientation to demonstrate the consistency of testing and material behavior.

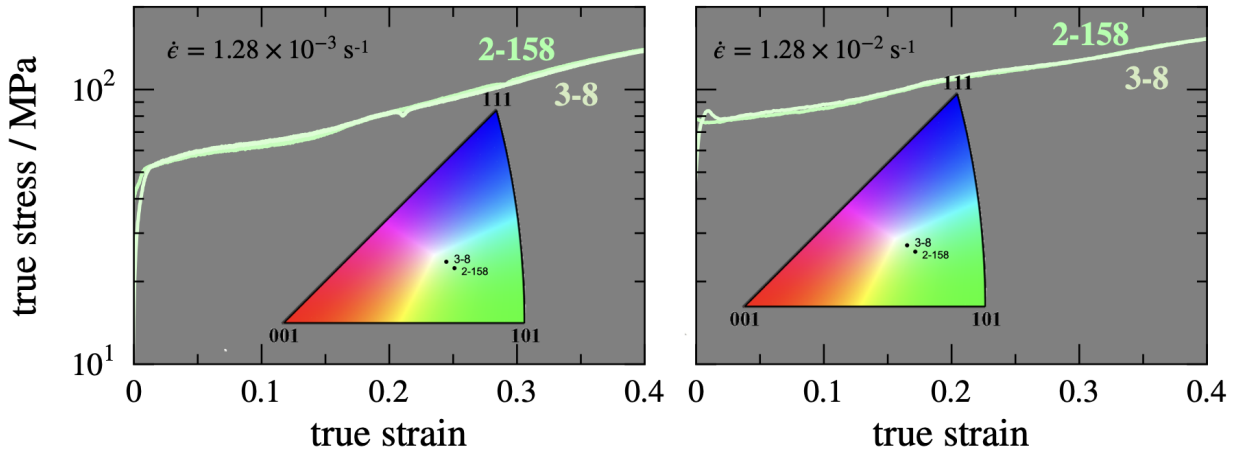

Figure 3.9 True stress–strain curve comparison of specimens 2-158 and 3-8 at two different strain rates demonstrating that they are the same crystallographic orientation.

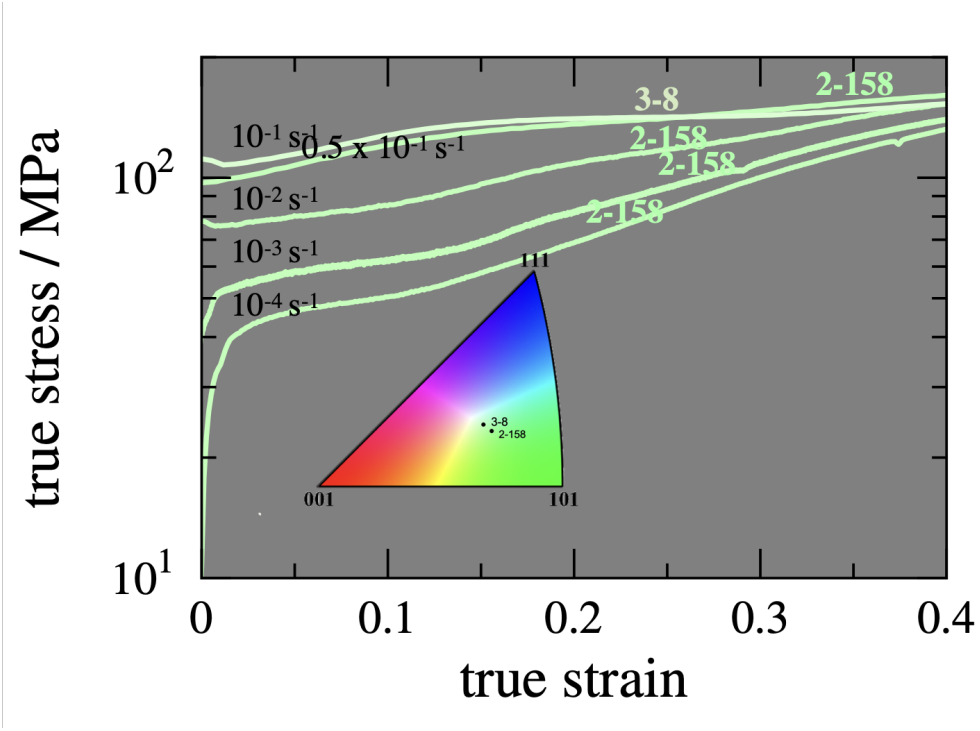

Figure 3.10 True stress–strain curves for different quasi-static strain rates (in s^{-1}) on specimens 2-158 and 3-8 with approximately the same crystallographic orientation near the center of the IPF.

section and the fracture surface. Figures 3.11 and 3.12 show the EBSD measurements for sample 5-34 and 8-176. Tensile direction inverse pole figure color is used to identify the localized rotations in the samples. Large slip bands could be visibly seen on the top surface of sample 5-34. EBSD analysis confirmed that these bands were shear bands with different crystal orientations as shown by contrasting colors. The localized lattice reorientation maps and IPFs show that these orientations observed a rotation towards the terminal stable [1 1 1] direction.

Tensile orientation inverse pole figures used to visualize the rotation of the orientations in Figure 3.13. Measurements of the orientation were performed at the grip and the fracture region. The original tensile axis (expected before cutting) was slightly different from the grip measurement, and is likely due to minor alignment errors while cutting the samples. Most orientations (except 2-158 and 10-64) rotate towards the stable [1 1 1] boundary, following the expectations of classical Schmid behavior.

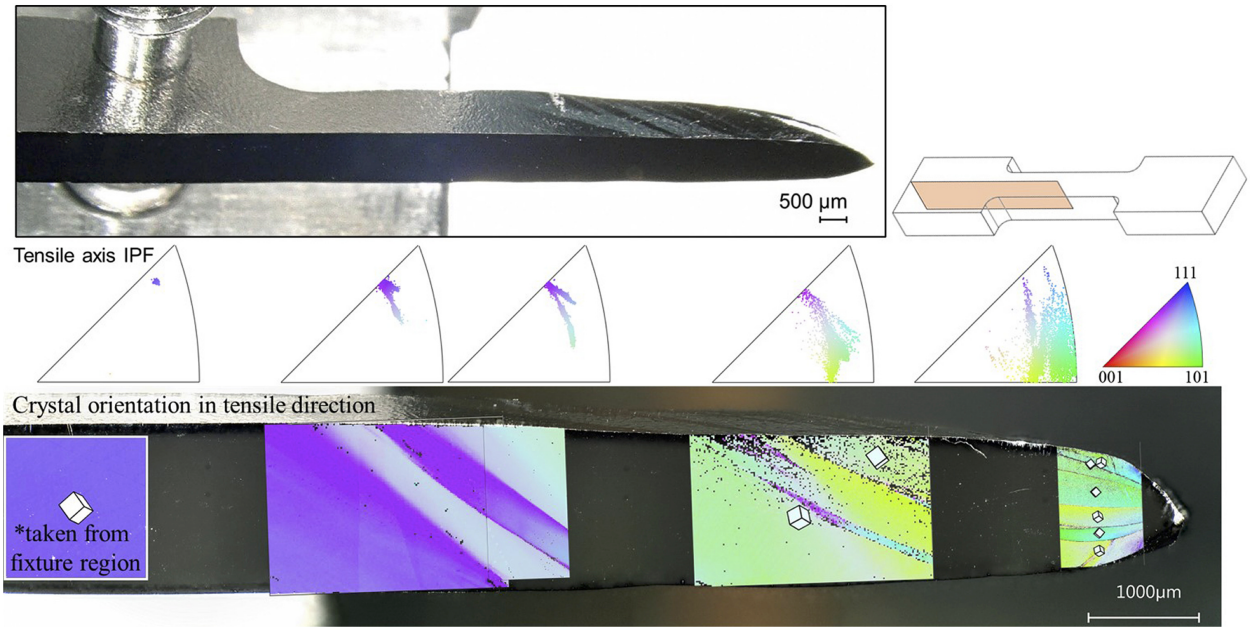

Figure 3.11 Optical image of specimen 5-34 showing large slip bands on the top surface and EBSD orientation maps in the tensile direction showing the crystal rotation from the fixture to the fracture surface [14].

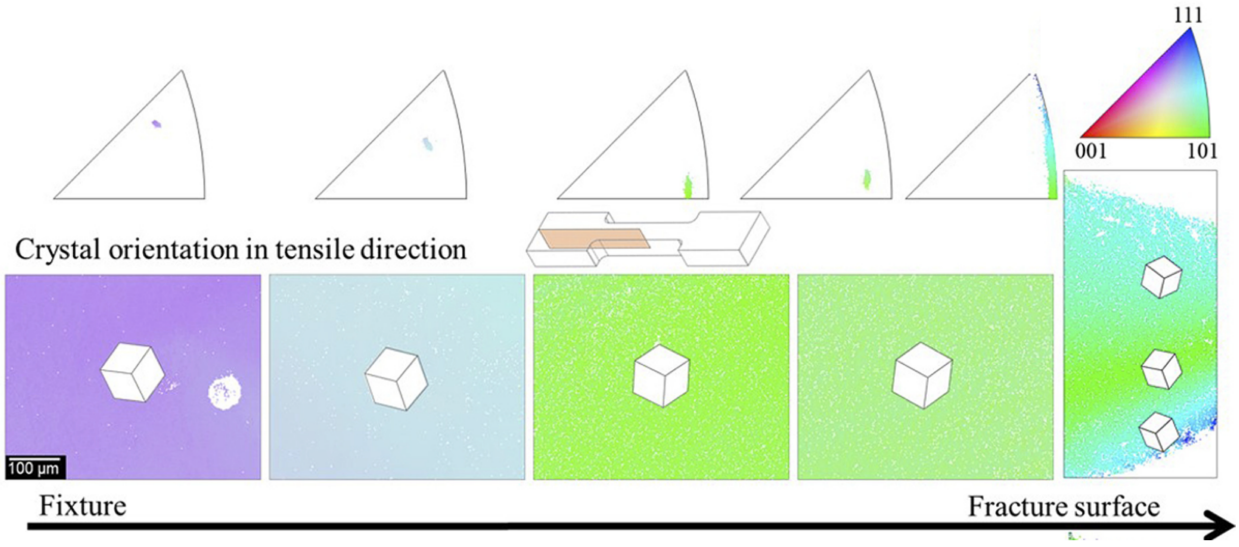

Figure 3.12 EBSD orientation map in the tensile direction of specimen 8-176 with an initial crystallographic orientation near the center of the IPF [14].

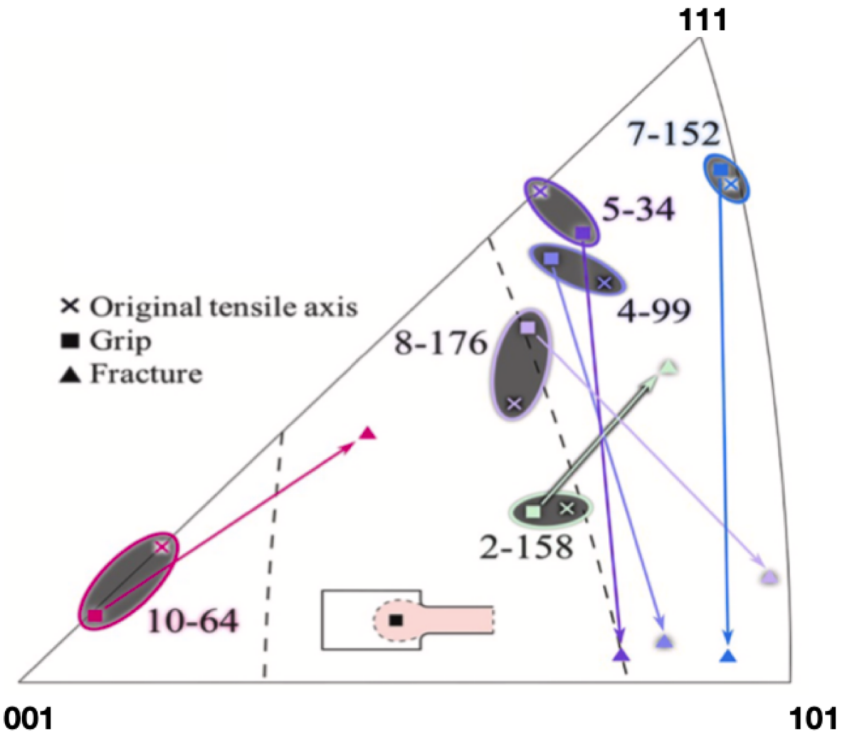

Figure 3.13 Experimental measurements of crystal orientation at the grip and at fracture points of the single-crystal dogbones [14].

CHAPTER 4

CRYSTAL PLASTICITY MODELING OF SINGLE CRYSTAL NB

A dislocation mechanics-based crystal plasticity model is used to simulate the stress-strain response and crystal re-orientation of niobium single crystals during uniaxial tension. The model was implemented in the open-source software DAMASK (Düsseldorf Advanced Material Simulation Kit) [74]. The numerical framework of DAMASK and solution of the boundary value problem using the inherent spectral based FFT solver have been previously detailed in Chapter 2, Section 2.5 and can be obtained in further detail in [74].

The model was formulated by tying together the kinetics of dislocation motion, the microstructure evolution, and the dislocation interactions for Nb based on the works of Blum and Eisenlohr [8], Cereceda et al. [10], Madec and Kubin [55].

4.1 Background

BCC crystal plasticity has been a subject of research since the 60s via experimental investigations as well as atomistic and mesoscopic modeling and simulation efforts [20, 22, 24, 38, 48, 77, 90, 97]. A detailed review of plastic deformation in BCC metals is presented in Chapter 2, Section 2.2

The model formulated for Nb is based on the constitutive description by Cereceda et al. [10] for Tungsten, another BCC refractory metal. This dislocation density-based model is based on thermally activated screw dislocation motion [10]. The microstructure evolution is based on the evolution of dislocation densities, expressed in terms of their generation, mutual interactions and annihilations [8]. For this thesis, the model is parametrized based on new material specific dislocation interaction coefficients obtained from DDD simulations [55], thus making is Nb specific.

This makes the model the most up-to-date with BCC dislocation mechanics.

The description of variables used in this chapter are consistent with the formulation of this model in DAMASK.

4.2 Flow rule

The plastic velocity gradient is additively composed from slip rates as

$$\mathbf{L}_{\mathrm{p}} = \sum_{\alpha} \dot{\gamma}^{\alpha} \mathbf{m}^{\alpha} \otimes \mathbf{n}^{\alpha} \tag{4.1}$$

with the unit vectors $\mathbf{m}^{\alpha}$ and $\mathbf{n}^{\alpha}$ indicating the slip direction and slip plane normal for each slip system (indexed by α) of the different slip families in Nb [74].

The resolved component of the applied stress is known as the Resolved Shear Stress (RSS) is the driving for for the slip rate ($\dot{\gamma}^{\alpha}$) and is expressed as

$$\tau^{\alpha} = \mathbf{M}_{\mathrm{p}} . (\mathbf{m}^{\alpha} \otimes \mathbf{n}^{\alpha}) \tag{4.2}$$

where $\mathbf{M}_{\mathrm{p}}$ is the work-conjugate Mandel stress of the plastic velocity gradient [74].

In dislocation density based models, the slip rate $\dot{\gamma}^{\alpha}$, on a slip system α, is related to the average velocity of mobile screw dislocations v^{α} by the Orowan equation [60]:

$$\dot{\gamma}^{\alpha} = \rho_{\mathrm{mob}}^{\alpha} b v^{\alpha} \tag{4.3}$$

where $\rho_{\mathrm{mob}}^{\alpha}$ is the mobile dislocation density in slip system α, and b is the length of the Burgers vector.

4.3 Screw dislocation mobility law

The constitutive law described in this section is adopted from Cereceda et al. [10]. In our

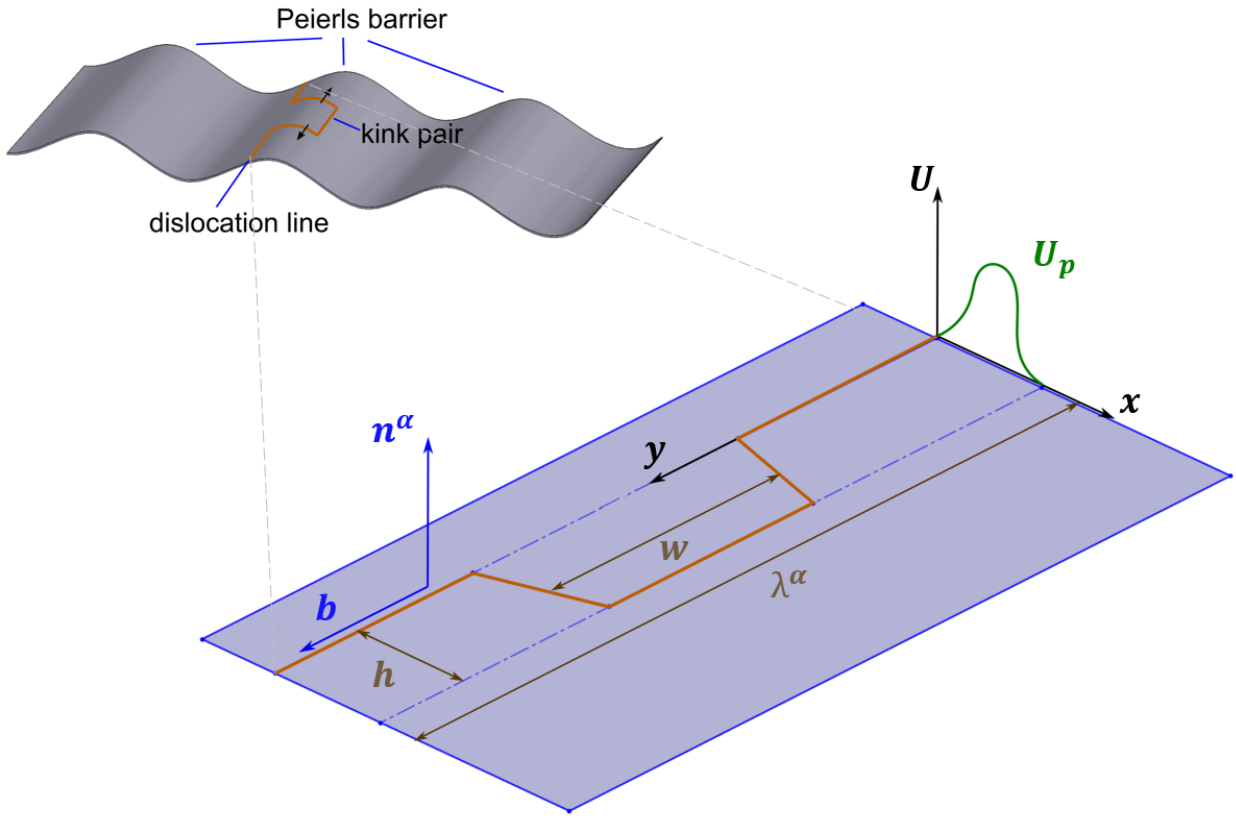

Figure 4.1 Schematic representation of a kink pair on a screw dislocation segment of length l lying on a slip plane $\mathbf{n}^\alpha$. The vertical axis represents the potential energy, with the Peierls potential indicated. Adapted from [10].

temperature regime, screw dislocation motion is the rate limiting activity for BCC crystal plasticity. During thermal activation in BCC metals, a dislocation overcomes a short-range barrier by nucleation of kink-pairs and their subsequent lateral relaxation. This is depicted schematically in Fig. 4.1. The average dislocation velocity is calculated from the total time required for a kink pair to form and subsequently sweep past a short-range barrier as

$$v^\alpha = \frac{h}{t_t}, \tag{4.4}$$

where h is the distance between two consecutive Peierls valleys and t_t is the total time taken for a kink pair to nucleate and sweep past a screw dislocation segment of length λ^α , calculated as

$$t_t = t_n + t_k = J(\tau^\alpha, T)^{-1} + \frac{\lambda^\alpha - w}{2v_k(\tau^\alpha, T)} \tag{4.5}$$

where t_n is the time taken to nucleate a kink pair and t_k is the time taken for the kink pair to travel half the length of the screw dislocation segment. The nucleation time is inversely related to the kink pair nucleation rate, $J(\tau^\alpha, T)$. w is the separation distance between the kink pair and v_k is the the velocity of the kink pair. The kink pair nucleation rate follows an Arrhenius formulation:

$$J(\tau^\alpha, T) = \frac{\omega(\lambda^\alpha - w)}{b} \exp\left(-\frac{\Delta H_{\text{kp}}(\tau^\alpha)}{kT}\right) \tag{4.6}$$

where ω is the attempt frequency, ΔH_{kp} is the activation energy of a kink pair at stress of τ^α and k is the Boltzmann's constant. The kink velocity is expressed as

$$v_k(\tau^\alpha, T) = \frac{b\tau^\alpha}{B(T)} \tag{4.7}$$

where B is the friction coefficient which assumes a constant value from calculations of [10]. Using Equations (4.5) to (4.7) in Equation (4.4), the average dislocation velocity can be calculated.

The stress dependence of $\dot{\gamma}^\alpha$ is a consequence of the stress dependence of ΔH_{kp}. ΔH_{kp} is formulated as

$$\Delta H_{\text{kp}} = Q_{\text{sl}} \left\{ 1 - \left[\frac{\tau^\alpha_{\text{eff}}}{\tau_{\text{p}}} \right]^p \right\}^q \tag{4.8}$$

where Q_{sl} is the activation energy for glide in the absence of applied stress. p and q define the shape of the dislocation obstacle. For most obstacles, $0 < p \leq 1$ and $1 \leq q \leq 2$.

τ^α_{eff} is the thermal component of stress which is calculated as

$$\tau^\alpha_{\text{eff}} = \begin{cases} |\tau^\alpha| - \tau^\alpha_{\text{pass}} & \text{for} \quad |\tau^\alpha| > \tau^\alpha_{\text{pass}} \\ 0 & \text{for} \quad |\tau^\alpha| \leq \tau^\alpha_{\text{pass}} \end{cases} \tag{4.9}$$

where τ^α is the resolved shear stress on the slip system α.

The athermal component, $\tau^\alpha_{\text{pass}}$ also known as the passing stress (hardening stress) is calculated as

$$\tau^\alpha_{\text{pass}} = \mu b \left(\sum_{\alpha'=1}^{N_s} \xi_{\alpha\alpha'} (\rho^{\alpha'}_{\text{mob}} + \rho^{\alpha'}_{\text{dip}}) \right)^{\frac{1}{2}} \tag{4.10}$$

where $\rho_{\text{mob}}^{\alpha'}$ and $\rho_{\text{dip}}^{\alpha'}$ are the dipole dislocation densities in slip system α', $\xi_{\alpha\alpha'}$ is the interaction coefficient matrix between the slip system α and other slip systems α' and μ is the shear modulus. Dislocation interaction matrix is further in upcoming Section 4.4.1.

τ_{p} is the Peierls stress needed to overcome the obstacle without any thermal activation:

$$\tau_{\text{p}} = (|\tau^{\alpha}| - \tau_{\mu}^{\alpha}) \qquad \text{at T = 0 K} \tag{4.11}$$

4.4 Dislocation density evolution law

From the contributions of Blum and Eisenlohr [8], dislocation density evolution is related to their multiplication, dipole formation and mutual annihilation.

The rate of evolution of the mobile dislocation density is given by:

$$\dot{\rho}_{\text{mob}}^{\alpha} = \frac{|\dot{\gamma}^{\alpha}|}{b\Lambda^{\alpha}} - \frac{2\hat{d}^{\alpha}}{b}\rho_{\text{mob}}^{\alpha}|\dot{\gamma}^{\alpha}| \tag{4.12}$$

The first term in Equation (4.12) accounts for the generation of unipolar (mobile) dislocations due to multiplication determined by the dislocation mean free path Λ^{α}. The second term accounts for its decrease due to dipole formation.

A dipole dislocation is formed when two mobile dislocations with opposite signs are at a distance greater than $\check{d}^{\alpha}$ but less than the critical distance for dipole formation $\hat{d}^{\alpha}$. The evolution of the dipole dislocation density is given by

$$\dot{\rho}_{\text{dip}}^{\alpha} = \frac{2(\hat{d}^{\alpha} - \check{d}^{\alpha})}{b}\rho_{\text{mob}}^{\alpha}|\dot{\gamma}^{\alpha}| - \frac{2\check{d}^{\alpha}}{b}\rho_{\text{dip}}^{\alpha}|\dot{\gamma}^{\alpha}| - \rho_{\text{dip}}^{\alpha}\frac{4v_{\text{cl}}}{\hat{d}^{\alpha} - \check{d}^{\alpha}} \tag{4.13}$$

The terms in Eq. (4.13) are the formation of dislocation dipoles reduced by the spontaneous annihilation of mobile dislocations, the spontaneous annihilation of dipoles with mobile dislocations and the loss of dislocation dipoles from dislocation climb.

$\hat{d}$ is the glide plane distance below which two dislocations form a stable dipole calculated as

$$\hat{d}^{\alpha} = \frac{\mu b}{8\pi(1-\nu)|\tau^{\alpha}|} \tag{4.14}$$

$\check{d}$ is the distance below which two dislocations annihilate, typically a multiple of the Burgers vector:

$$\check{d}^{\alpha} = D_{\text{a}} b \tag{4.15}$$

where D_a is the annihilation coefficient.

The dislocation climb velocity v_{cl}, is calculated as

$$v_{cl} = \mu D_0 \exp\left(-\frac{Q_{cl}}{k_B T}\right) \frac{f_{at}}{\pi(1-\nu)k_B T} \frac{1}{\hat{d}^\alpha + \check{d}^\alpha} \tag{4.16}$$

where Q_{cl} is the activation energy for dislocation climb, D_0 is the pre-factor of the self-diffusion coefficient and f_{at} is the factor to calculate activation volume for climb.

In this model, strain hardening is described using a dislocation Mean Free Path (MFP) approach, where the mean free path is denoted by Λ^α and is calculated as

$$\frac{1}{\Lambda^\alpha} = \frac{1}{D} + \frac{1}{\lambda^\alpha} \tag{4.17}$$

where D is the effective grain size and

$$\frac{1}{\lambda^\alpha} = \frac{1}{i_{sl}} \left(\sum_{\alpha'=1}^{N_s} \xi_{\alpha\alpha'} (\rho_{mob}^{\alpha'} + \rho_{dip}^{\alpha'}) \right)^{\frac{1}{2}} \tag{4.18}$$

where i_{sl} is a fitting parameter that represents the number of dislocations passed by a dislocation before being trapped by a forest dislocation.

4.4.1 Dislocation interaction coefficients

A recent study by Madec and Kubin [55] revealed that dislocation interaction coefficients are not universal for a given crystal structure. It was shown that the value of the Poisson ratio and the existence of asymmetric junction configurations affect these values. The latter results in doubly degenerate coefficients where the strengths differ when the primary system and the forest system are interchanged. These effects are a consequence of various dislocation mechanisms and slip system geometries, and these details are covered in greater detail in Chapter 2, Section 2.2.3.

In Eq. (4.10), $\xi_{\alpha\alpha'}$ is the coefficient matrix of interaction strengths between the different slip systems α and α'. Madec and Kubin [55] calculated 24 different coefficients corresponding to the self-interaction , the coplanar interaction , three collinear interactions, and twelve junctions, of which seven are doubly degenerated and five occur between $\{1\,1\,0\}$ and $\{1\,1\,2\}$ slip systems, using dislocation dynamics (DD) simulations for various BCC metals including Nb. This CP model used

these accurate material-dependent coefficients for $\xi_{\alpha\alpha'}$, with the expectation of more accurate prediction of strain hardening due to dislocation interactions during tension.

4.5 Specimen geometry, boundary conditions and model parameters

The mechanical response of a single crystal undergoing uniaxial tension using dogbone samples exhibits marked spatial gradients between the central and peripheral gage sections experimentally. Capturing the these gradients through full-field simulations requires a well suited constitutive description with proper combinations of primary state variables (input parameters). To take advantage of a numerically efficient (Fourier-based) spectral numerical solution scheme provided in DAMASK, single-crystal samples of dogbone geometry were discretized on a regular grid with a resolution of $300 \times 44 \times 10$. To circumvent the strict periodicity constraint imposed by that solution scheme on the hexahedral simulation box, those grid points outside of the dogbone geometry were considered to be of a dilatational material with comparatively low stiffness and strength [56]. Due to the computationally expensive nature of dogbone simulations, it is necessary to identify the boundary conditions that are necessary to mimic the behavior of single crystals with a simpler geometry having a lower mesh resolution, without compromising the results. This was done by simulating a simplified geometry with just a rectangular block of gage section, while using the same boundary conditions as the full dogbone. The two geometries are schematically shown in Fig. 4.2.

	D1	C1	B2	A2	A3	C3	B4	D4	A6	D6	B5	C5	A-4	B-3	C-10	D-9	D-6	C-5	B-12	A-11	C-2	D-1	A-8	B-7
D1	1	3	6	6	7	5	4	2	4	2	7	5	18	18	11	8	9	13	17	14	13	9	17	14
C1	3	1	6	6	4	2	7	5	7	5	4	2	18	18	8	11	13	9	14	17	9	13	14	17
B2	6	6	1	3	5	7	2	4	5	7	2	4	11	8	18	18	17	14	9	13	17	14	13	9
A2	6	6	3	1	2	4	5	7	2	4	5	7	8	11	18	18	14	17	13	9	14	17	9	13
A3	7	5	4	2	1	3	6	6	2	4	7	5	9	17	13	14	18	11	18	8	13	17	9	14
C3	4	2	7	5	3	1	6	6	5	7	4	2	13	14	9	17	18	8	18	11	9	14	13	17
B4	5	7	2	4	6	6	1	3	7	5	2	4	17	9	14	13	11	18	8	18	17	13	14	9
D4	2	4	5	7	6	6	3	1	4	2	5	7	14	13	17	9	8	18	11	18	14	9	17	13
A6	5	7	4	2	2	4	7	5	1	3	6	6	9	17	14	13	13	17	14	9	18	11	8	18
D6	2	4	7	5	5	7	4	2	3	1	6	6	13	14	17	9	9	14	17	13	18	8	11	18
B5	7	5	2	4	7	5	2	4	6	6	1	3	17	9	13	14	17	13	9	14	11	18	18	8
C5	4	2	5	7	4	2	5	7	6	6	3	1	14	13	9	17	14	9	13	17	8	18	18	11
A-4	19	19	10	8	9	12	16	15	9	12	16	15	1	20	24	24	23	22	21	2	23	22	2	21
B-3	19	19	8	10	16	15	9	12	16	15	9	12	20	1	24	24	22	23	2	21	22	23	21	2
C-10	10	8	19	19	12	9	15	16	15	16	12	9	24	24	1	20	21	2	23	22	2	21	23	22
D-9	8	10	19	19	15	16	12	9	12	9	15	16	24	24	20	1	2	21	22	23	21	2	22	23
D-6	9	12	16	15	19	19	10	8	12	9	16	15	23	21	22	2	1	24	20	24	23	2	22	21
C-5	12	9	15	16	10	8	19	19	16	15	12	9	21	23	2	21	24	1	24	20	2	23	21	22
B-12	16	15	9	12	19	19	8	10	15	16	9	12	22	2	23	22	20	24	1	24	22	21	23	2
A-11	15	16	12	9	8	10	19	19	9	12	15	16	2	22	21	23	24	20	24	1	21	22	2	23
C-2	12	9	16	15	12	9	16	15	19	19	10	8	23	21	2	22	23	2	21	22	1	24	24	20
D-1	9	12	15	16	16	15	12	9	10	8	19	19	21	23	22	2	2	23	22	21	24	1	20	24
A-8	16	15	12	9	9	12	15	16	8	10	19	19	2	22	23	21	21	22	23	2	24	20	1	24
B-7	15	16	9	12	15	16	9	12	19	19	8	10	22	2	21	23	22	21	2	23	20	24	24	1

Table 4.1 Dislocation interaction matrix for BCC metals [55]. Schmid and Boas notation is used to identify slip systems. The full details of slip systems corresponding to the notations can be found in Appendix:A.

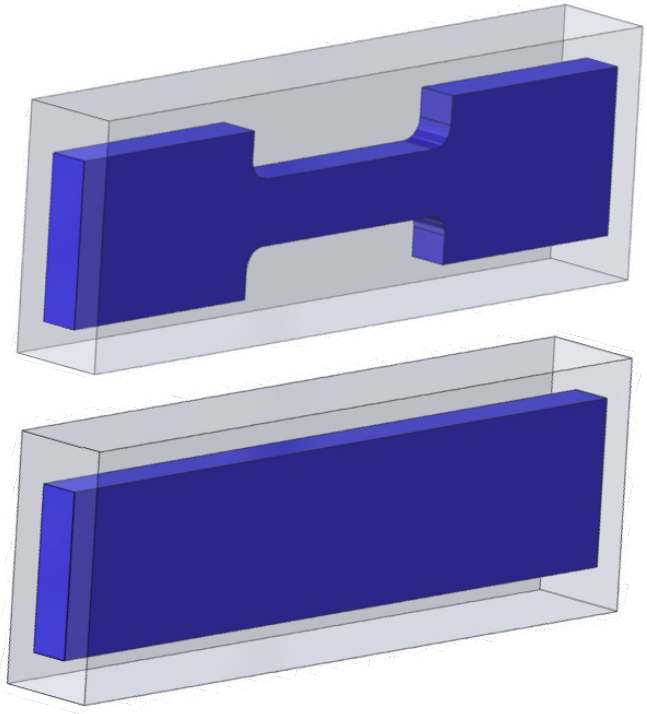

Figure 4.2 Comparison of full dogbone (top) and simplified gage section (bottom) geometries used in the simulations.

Selected orientations were simulated in uniaxial tension at a strain rate of $1 \times 10^{-3}\,\mathrm{s}^{-1}$ until 20% strain in the gage section. The simulation results were post-processed to calculate the stress-strain response and lattice re-orientation. The elasticity and plasticity parameters for Nb used in the simulations are presented in Table 4.3 and Section 4.5.

	ID	interaction type	coefficient
	1	self	0.009
	2	collinear 60°	0.825
{1 1 0}-{1 1 0}			
	3	coplanar	0.009
	4	J_1 0° (G)	0.205
	5	J_1 70.53° (G)	0.245
	6	J_2	0.310
	7	J_3	0.285
{1 1 2}-{1 1 0}			
	8	collinear 90°	0.9
	9	collinear 30°	0.64
	10	J_4 0° (G)	0.2025
	11	J_4 70.53° (G)	0.255
	12	J_5 0° (G)	0.175
	13	J_5 70.53° (G)	0.205
	14	J_6 29.50°	0.205
	15	J_6 58.52°	0.20
	16	J_7 58.52°	0.25
	17	J_7 79.98°	0.27
	18	J_8 35.26°	0.275
	19	J_8 90°	0.265
{1 1 2}-{1 1 2}			
	20	J_9	0.28
	21	J_{10} 28.56°	0.23
	22	J_{10} 72.98°	0.235
	23	J_{11}	0.265
	24	J_{12}	0.19

Table 4.2 Dislocation interactions and their coefficient values for Nb [55]. (G) indicates glissile junctions.

parameter	value
C_{11}	246 GPa
C_{12}	134 GPa
C_{44}	28 GPa

Table 4.3 Elastic constants used for Nb.

Variable	Description	Value	Unit
B	friction coefficient	8.3×10^{-5}	Pa s
ω	attempt frequency for kink pair nucleation	9.1×10^{11}	s^{-1}
h	height of the kink pair	2.567	Å
w	width of the kink pair	11	b
Q_{cl}	Activation energy for climb	4.5×10^{-19}	J
Q_{sl}	Activation energy for glide	2.72×10^{-19}	J
τ_{p}	Peierls stress	20	MPa
b	magnitude of Burgers vector	2.72	Å
D_{a}	annhihilation coefficient	10	–
D_0	pre-factor for self-diffusion	1.1×10^{-4}	–
d_{g}	grain size	50×10^{-6}	m
p	p exponent in glide velocity	0.86	–
q	q exponent in glide velocity	1.69	–
i_{sl}	Adj. parameter for distance between 2 forest dislocations	100	–
f_{at}	factor to calculate atomic volume	1	–
$\xi_{\alpha\alpha'}$	dislocation interaction matrix	Table 4.2	–
$\rho^{\alpha}_{\mathrm{mob0}}$	initial mobile dislocation density	10^{11}	m^{-2}
$\rho^{\alpha}_{\mathrm{dip0}}$	initial dipole dislocation density	10^{11}	m^{-2}

Table 4.4 Plasticity parameters for Nb used in the model.

4.6 Constitutive model for dilatational layer and selection of material parameters

The mechanical response of the surrounding buffer layer is formulated using an isotropic plasticity model that combines an isochoric response due to the deviatoric stress with a dilatational response due to the hydrostatic pressure (mean stress) [56]. The deviatoric stress (in the lattice configuration) is given by:

$$\mathbf{M}_{\mathrm{p}}^{\mathrm{dev}} = \mathbf{M}_{\mathrm{p}} - \mathrm{tr}\,\mathbf{M}_{\mathrm{p}}/3 \tag{4.19}$$

The mean stress (in the intermediate configuration) is given by:

$$\mathbf{M}_{\mathrm{i}}^{\mathrm{sph}} = \mathbf{I}\,\mathrm{tr}\,\mathbf{M}_{\mathrm{i}}/3 \tag{4.20}$$

The kinetics and internal state parameterization of the model are derived from the phenomenological crystal plasticity model that postulates a power-law relation between driving force and deformation rate, and an internal deformation resistance (ξ) [56, 66, 74]. The strain rate connected to isochoric deformation is driven by J_2, i.e. the second invariant of $\mathbf{M}_{\mathrm{p}}^{\mathrm{dev}}$:

$$\dot{\gamma}_{\mathrm{p}} = \dot{\gamma}_0 \left(\frac{\sqrt{3J_2}}{\mathbf{M}\xi} \right)^n = \dot{\gamma}_0 \left(\sqrt{\frac{3}{2}} \frac{\left\| \mathbf{M}_{\mathrm{p}}^{\mathrm{dev}} \right\|_F}{M\xi} \right)^n \tag{4.21}$$

where $\dot{\gamma}_0$ is the reference strain rate, n is the stress exponent and M is the Taylor factor. Consequently, the associated plastic velocity gradient $\mathbf{L}_{\mathrm{p}}$ acting in the lattice configuration is calculated as:

$$\mathbf{L}_{\mathrm{p}} = \frac{\dot{\gamma}_{\mathrm{p}}}{M} \frac{\mathbf{M}_{\mathrm{p}}^{\mathrm{dev}}}{\left\| \mathbf{M}_{\mathrm{p}}^{\mathrm{dev}} \right\|_F} \tag{4.22}$$

The dilatational response of the buffer layer is facilitated using a similar constitutive law for the dilatational rate $\dot{\gamma}_{\mathrm{i}}$ and velocity gradient $\mathbf{L}_{\mathrm{i}}$ in the intermediate configuration as:

$$\dot{\gamma}_{\mathrm{i}} = \dot{\gamma}_0 \left(\frac{\sqrt{3J_2}}{\mathbf{M}\xi} \right)^n = \dot{\gamma}_0 \left(\sqrt{\frac{3}{2}} \frac{\left\| \mathbf{M}_{\mathrm{i}}^{\mathrm{sph}} \right\|_F}{M\xi} \right)^n \tag{4.23}$$

$$\mathbf{L}_{\mathrm{i}} = \frac{\dot{\gamma}_{\mathrm{i}}}{M} \frac{\mathbf{M}_{\mathrm{i}}^{\mathrm{sph}}}{\left\| \mathbf{M}_{\mathrm{i}}^{\mathrm{sph}} \right\|_F} \tag{4.24}$$

The scalar resistance ξ to plastic flow evolves asymptotically from its initial value ξ_0 towards a final saturation value xi_∞, analogous to the phenomenological power law model:

$$\dot{\xi} = Mh_0\dot{\gamma}\left|1 - \frac{\xi}{\xi_\infty}\right|^a \operatorname{sgn}\left(1 - \frac{\xi}{\xi_\infty}\right) \tag{4.25}$$

where h_0 and a are hardening parameters.

Maiti and Eisenlohr [56] used a plastically isotropic plate with a circular void at its center to estimate the elastic constants and plastic parameters of both materials. The largest elastic stiffness constant C_{11} of the dilatational void was scaled down one order of magnitude relative to its surrounding plate. C_{12} and C_{44} were calculated such that elastic isotropy and vanishing Poisson ratio for the void was ensured. The flow stress of the void was set to be two orders of magnitude lower than the plate material.

However, during test simulations of single crystal Nb using the described model, the compromise between diminishing stress in the buffer layer and its associated computational cost and non-convergence was attained by reducing C_{11} and the flow stress by 3 orders of magnitude relative to Nb. The process of realizing the relative elastic constants and flow stress was trial and error based, during a tedious exercise of debugging non-convergence of simulations which involved testing the sensitivity of all constitutive parameters. While this relative value works in achieving diminishing stress for single crystal Nb in the dogbone geometry, it may be worthwhile doing an exhaustive study of optimizing the buffer layer constitutive parameters for different bulk materials.

The set of material parameters for the surrounding buffer layer used in single crystal Nb simulations are outlined in Table 4.5

parameter	value
C_{11}	0.24 GPa
C_{12}	0 GPa
C_{44}	0.12 GPa
$\dot{\varepsilon}_0$	$1 \times 10^{-3}\ \mathrm{s}^{-1}$
n	5
τ_0	0.3 MPa
g_∞	0.6 MPa
a	2
h_0	1 MPa
M	3

Table 4.5 Summary of material parameters for the dilatational layer used in the simulations: elastic constants C_{ij}, reference strain-rate $\dot{\varepsilon}_0$, stress exponent n , initial and saturation flow-stress τ_0 and g_∞, hardening parameters h_0 and a, and Taylor factor M.

4.7 Summary of orientations for simulations

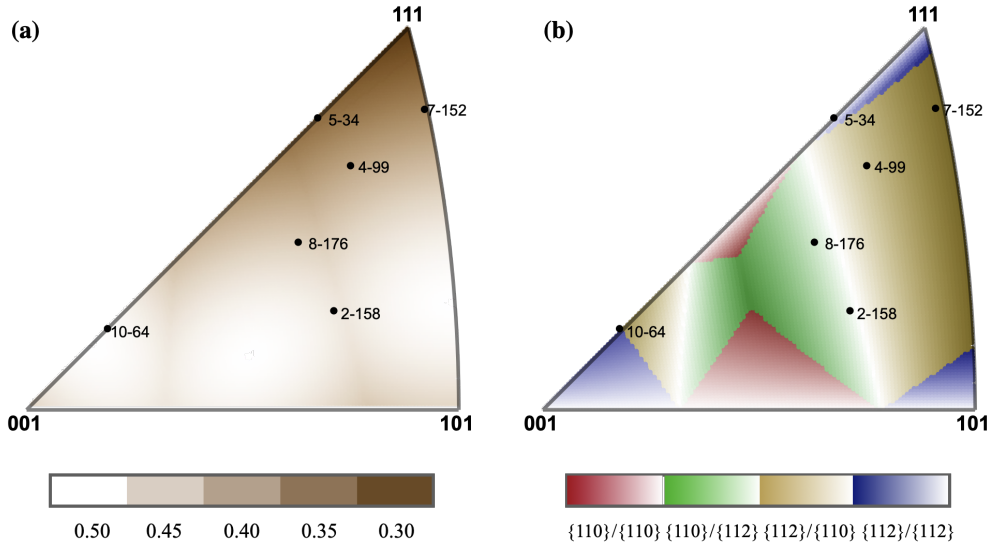

Figure 4.3 Tensile orientations selected for simulations in inverse pole figures visualizing (a) Magnitude of the Schmid factor of the most active slip system. (b) Most active slip family pairs, visualized as the ratio of their Schmid factors. As the color gradient changes from dark to white, the relative preference for the system with higher Schmid factor decreases from stronger to equal.

The simulated orientations were selected based on the availability of measured values of the tensile stress–strain responses and lattice re-orientation measurements (from EBSD) to facilitate a one-to-one comparison. The selected orientations are visualized in two IPFs to convey information about the dominant slip families and their relative strengths as well as the magnitude of the Schmid

factor of the most active slip system in Fig. 4.3. The IPF showing magnitude of the Schmid factor provides insights into ease of plastic deformation on the most active slip system. In Fig. 4.3(a), white zones have the higher Schmid factor and darker zones have lower values. Fig. 4.3(b) was constructed as follows: The Schmid factor (SF) of the 24 slip systems in the $\{1\,1\,0\}\langle 1\,1\,1\rangle$ and $\{1\,1\,2\}\langle 1\,1\,1\rangle$ families were calculated for each grain in all possible in-plane tensile orientations. Next, the ratio of the highest SF to the second highest SF value was calculated for each orientation and the corresponding competing slip families were visualized using a color code system. Finally, the strength of the competition between the two dominating slip families was visualized by incorporating a color gradient system in addition to a color code. This means, as the color gradient changes from dark to white, the relative preference for the system with higher Schmid factor decreases from stronger to equal. This helps provide insights into the expected dominant slip family pairs.

4.8 Results and Discussion

The results of the simulations were post-processed to calculate and visualize their lattice reorientation and stress–strain responses and were simultaneously compared to the experimental measurements. True stress–strain curves are produced from the Cauchy stress values calculated from the first Piola–Kirchhoff stress and deformation gradient, and the strain tensor of the deformation gradient. Details of these calculations are presented in Chapter 2, Section 2.5.1. The lattice reorientation is visualized in an IPF, by importing the orientation information of all the gage section points for the first and last time increment from the simulation results. The model assumes slip activity on the 12 $\langle 1\,1\,1\rangle\{1\,1\,0\}$ and 12 $\langle 1\,1\,1\rangle\{1\,1\,2\}$ slip systems with equal populations of dislocation density on each system. The full dogbone geometry is compared to the simplified gage section geometry to analyze whether the computationally cheaper alternative can provide meaningful physical insight into the mechanical responses of interest.

4.8.1 Lattice reorientation after deformation

The spatially resolved local reorientation (tension direction IPF color map) and von Mises strain map for the dogbone geometries is presented in Fig. 4.4. This is compared to the direct

observation (photographs) of samples post failure shown in Fig. 4.5. Samples 5-34, 10-64, and 2-158 show slip bands in the experimental sample and similar bands were observed in their dogbone simulations. The experimental sample 4-99 was unavailable for photography, and hence is not shown in the analysis. The homogeneous lattice reorientation map on the simplified geometry is presented in Fig. 4.6. The simplified geometry, which by design, cannot accommodate local strains due to its uniform cross-section, has the same lattice reorientation for every voxel of its geometry. Therefore, it cannot be used to reproduce spatial heterogeneity in the lattice reorientation. This is evident from the comparisons of the lattice reorientation maps for the two geometries.

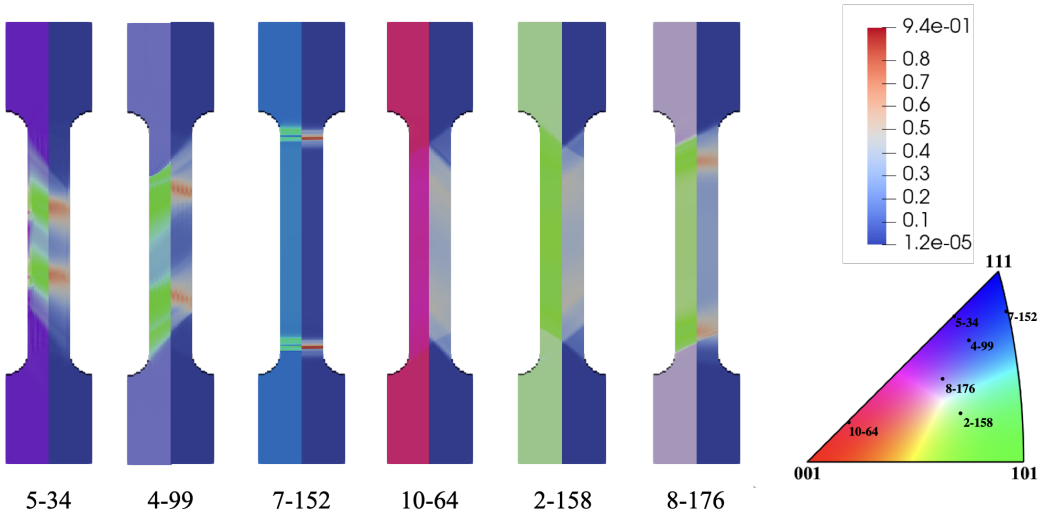

Figure 4.4 Local tension direction lattice reorientation (left side) and von Mises strain (right side) maps of the simulated dogbone samples, showing spatial gradients in the gage section.

Next, experimental EBSD measurements of deformed samples 5-34 and 8-176 are compared to tension direction inverse pole figure maps on their respective dogbone simulations for the same cross sections in Fig. 4.7 and Fig. 4.8. For orientations 5-34 and 8-176, the slip bands and their local re-orientation were similar looking overall, although a one-to-one matching cannot be easily made owing to the different total strains between the experimental and simulated samples. The trajectory of lattice reorientation (described by gage section tensile orientations plotted in IPFs -

Figure 4.5 Photographs of experimental single crystal dogbones after deformation to failure, showing visible spatially heterogeneous slip bands in samples 5-34, 10-64 and 2-158. A gap is intentionally left for missing sample 4-99.

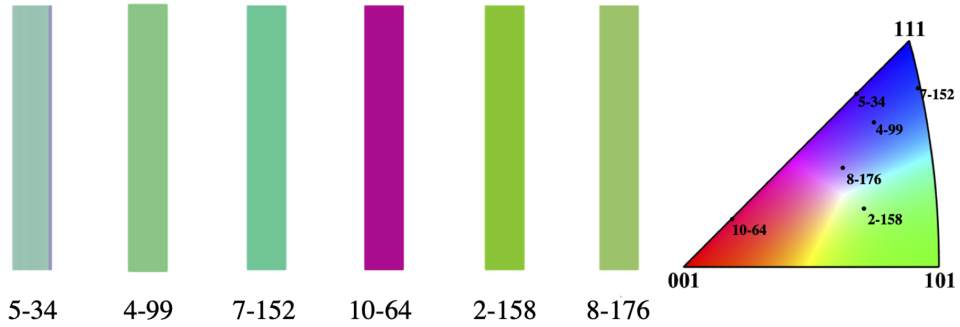

Figure 4.6 Local tension direction lattice reorientations maps of the simulated simplified geometry samples. This geometry does not show any spatial heterogeneity due to their uniform cross section.

refer Figs. 4.7 and 4.8 (c)) follow approximately the same path as their respective experimental observations - refer third IPF in Figs. 4.7 and 4.8 (a) for 20 % strain. Comparison of the spread of gage section tensile orientations in the experimental and simulated IPFs for sample 5-34 in Fig. 4.7 (compare third IPF in (a) for approximately 20 % strain and (c)) reveal that they are strikingly similar.

The re-orientation trajectories are analysed using IPFs. Fig. 4.9 shows tension direction IPF of all gage section points at the end of 20 % strain for all the simulated orientations. The experimental measurements are shown beside the simulated outcomes for comparison. The experimental measurements were performed only at the fixture region and neck region and the the trajectory was extrapolated using straight lines. A cloud like region around the overall solid reorientation

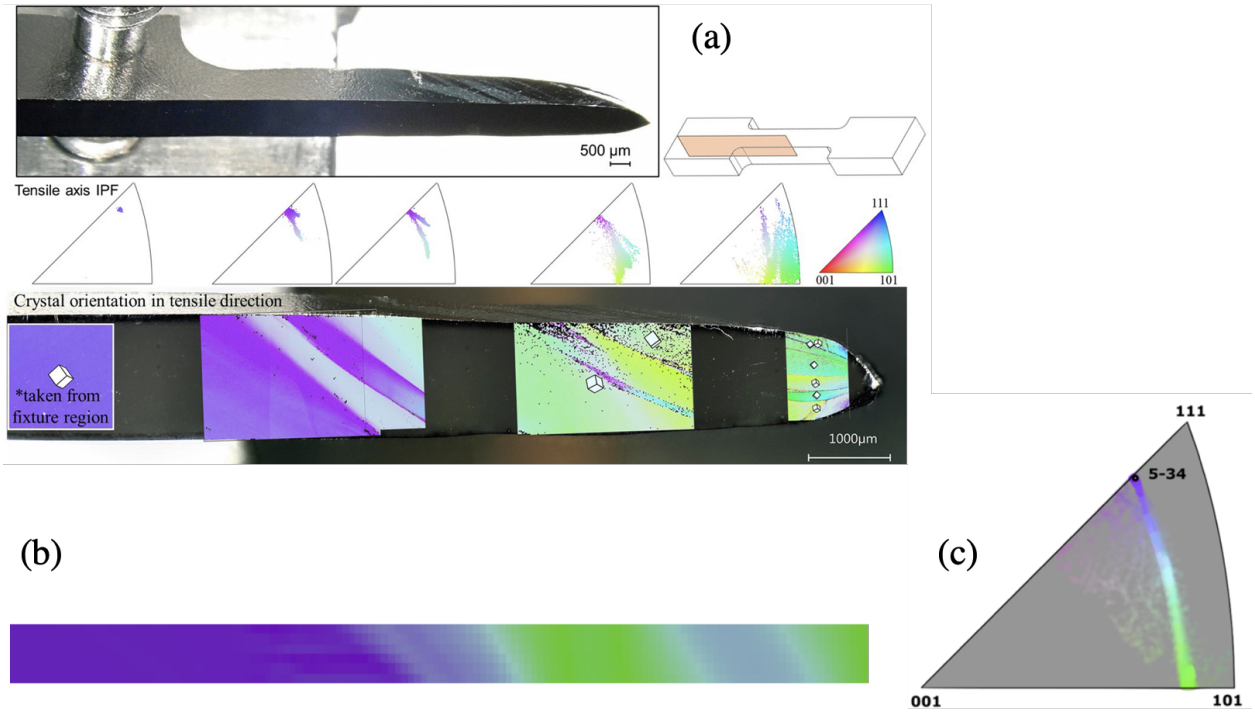

Figure 4.7 (a)Top image - Optical image of specimen 5-34 showing large shear bands on the top surface. Bottom image - EBSD orientation maps in the tensile direction showing the crystal rotation from the fixture to neck using IPF as well as local maps on the sample cross-section [14]. (b) Tensile IPF map on simulated dogbone geometry of the same initial orientation, shown for the same cross-section showing spatial gradients in re-orientation. (c) Tensile IPF map of the simulated gage section after 20 % deformation.

trajectory for 5-34 is likely due to skin effects at the intersection of the buffer layer and Nb which was not observed for any other orientation. This indicates that the buffer layer parameters may need further optimization. It is evident that samples 2-158 and 10-64 follow a different trajectory in the simulation. The classical expectation of following the terminal stable $\langle 1\,1\,1 \rangle$ boundary is not fulfilled experimentally by these 2 orientations and they will be investigated in the upcoming sections.

For simplified geometry simulations, due to homogeneous response, re-orientation is plotted as a function of strain (until 20 %). Since the average reorientation trajectory of the dogbone and simplified geometry is the same, the simplified geometry was used for future simulations for lattice reorientation, thus saving computational cost.

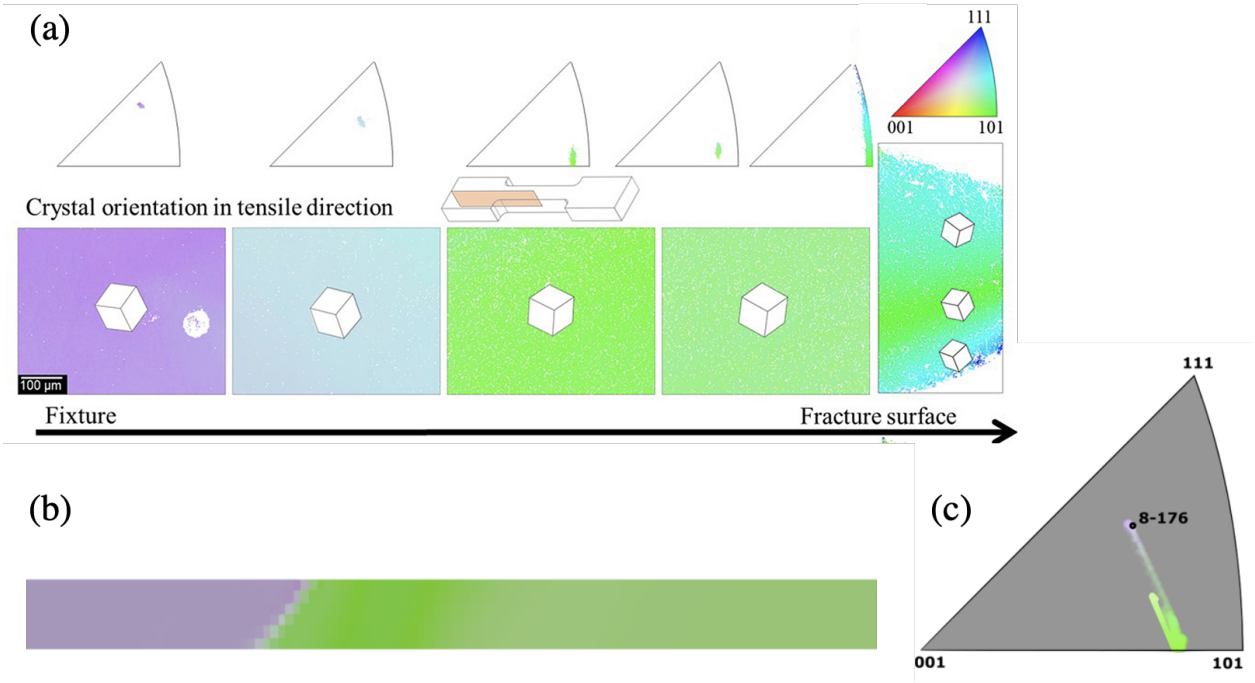

Figure 4.8 (a) EBSD orientation map in the tensile direction of specimen 8–176 with an initial crystallographic orientation near the center of the IPF [14]. (b) Tensile IPF map on simulated dogbone geometry of the same initial orientation, shown for the same cross-section showing spatial gradients in re-orientation. (c) Tensile IPF map of the simulated gage section after 20 % deformation from the simulation.

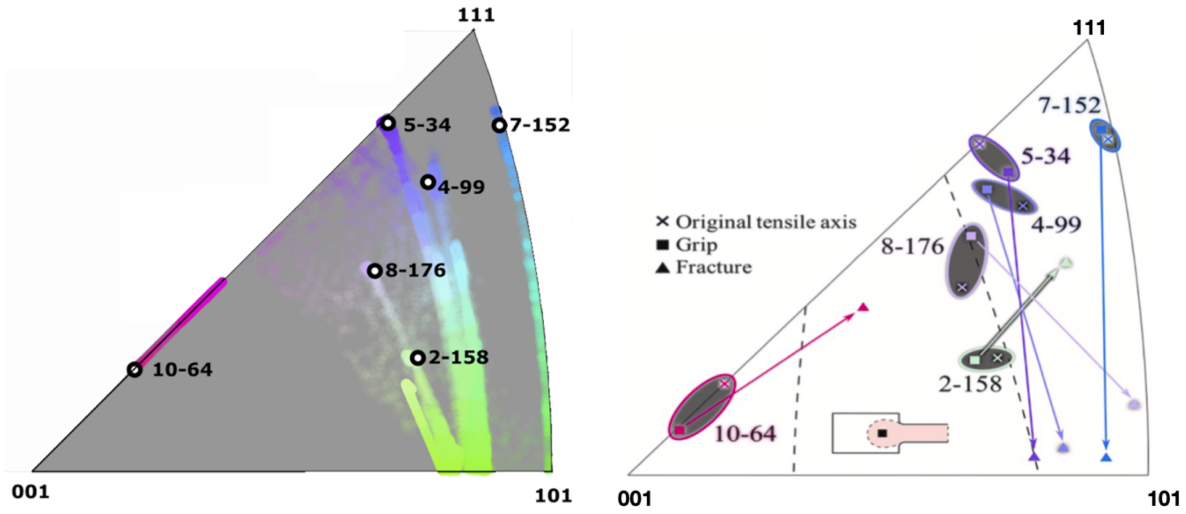

Figure 4.9 Lattice reorientation of simulated single-crystal dogbones (left) and experimentally measured single crystals for reference (right). The experimental measurements were performed only at the fixture region and neck region and the the trajectory was extrapolated using straight lines. The cloud like appearance around the lattice reorientation trajectory for 5-34 is likely due to skin effects at the intersection of the buffer layer and Nb.

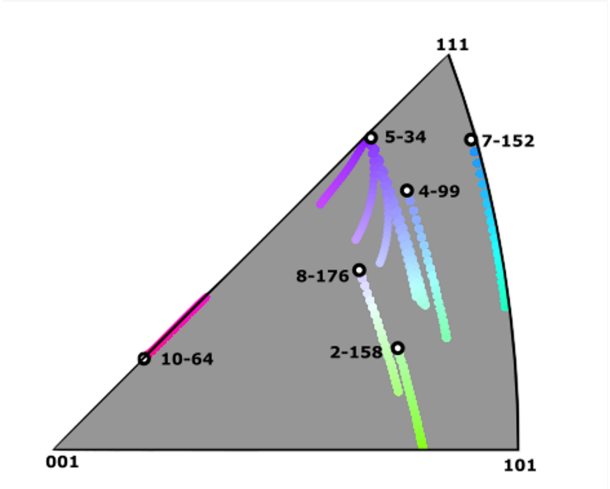

Figure 4.10 Lattice reorientation of simulated single-crystal simplified geometries.

4.8.2 Stress–strain curves

The true stress-strain curves from the simulations are compared to the experimentally measured outcomes in Fig. 4.11. Both dogbones and simplified geometries had the same stress–strain behavior and therefore are not separately presented. Although the strain-hardening behavior is not convincingly captured for any orientation, the overall yield and flow stress trends are similar for most orientations with the exception of 10-64. Sample 10-64 had the highest flow stress experimentally, when it is expected to be a soft orientation, which cannot be meaningfully explained without further investigations.

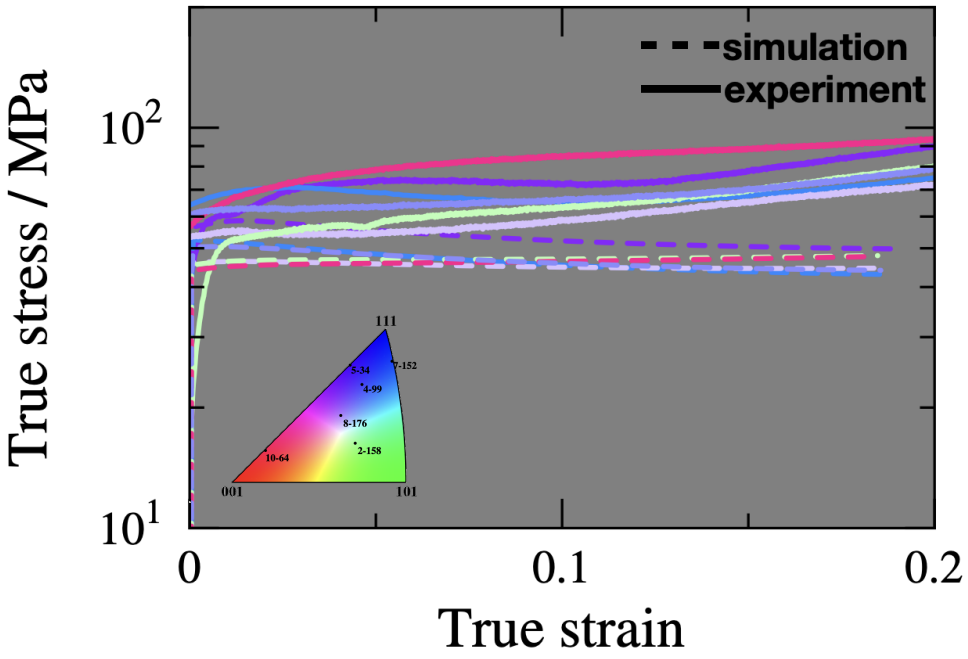

Figure 4.11 Comparison of experimental and simulated true stress–strain curves of tensile specimens colored by initial crystallographic tensile axis (see IPF inset).

4.8.3 Investigating the effect of initial dislocation density distribution on slip system activity, lattice reorientation, and stress–strain response

The presence of non-uniform distribution of dislocation densities across slip systems is highly likely in real samples. Since it is impractical to measure dislocation content on individual slip systems experimentally, it becomes essential to estimate their influence on slip system activity and its associated lattice reorientation and stress–strain response.

As a first step towards gaining these insights, the influence of initial conditions was tested by inhomogeneously distributing the initial dislocation densities on the 12 $\{1\,1\,0\}$ and 12 $\{1\,1\,2\}$ slip systems in the simulations of sample 10-64. 10-64 was chosen due to the discrepancies in it's lattice reorientation trajectory between simulation and experiment.

Inhomogeneity in the pre-existing dislocation density distribution in this orientation is introduced by using a log-normal distribution with a mean dislocation density μ and variance σ^2. 4 different distribution cases were tested with variances of $\sigma^2 = e^{0.2}$, e^1, e^2 and e^3 at a mean dislocation density of 1×10^{11} m^{-2}. For each case, the slip activity - expressed as shear rate on individual slip systems as a function of strain, and the associated lattice reorientation trajectories are analysed and compared. The results are connected to the direct influence of dislocation densities on strain hardening and re-orientation.

From Schmid factor calculations, 10-64 expects $\{1\,1\,2\}$ dominant single slip activity on slip system 15 ($(2\bar{1}\,1)[1\,1\,\bar{1}]$) with the highest value. The Schmid factor values for all the slip systems (along with the slip system indexes referenced in the analysis) for this orientation are presented in Figure 4.12. Figure 4.13 shows the effect of different log-normal distributions (case 1 – case 4) of initial dislocation densities on the slip activity (shear rate on slip systems) and the associated lattice reorientation. For a small variance as in case 1, the Schmid behavior is still obeyed, where system 15 is the most active slip system. It is evident that multiple slip systems are active for case 2 based on the shear rates, resulting in different (although very similar) reorientation trajectories. In case 3, system 15 is still the most active, however, tertiary system 9 is producing appreciable slip. In case 4, slip system 13, with the second highest Schmid factor, is the most active slip system, causing a

different rotation trajectory.

It can be inferred from these findings that non-homogeneous distributions of pre-existing dislocation densities influence slip activity and lattice reorientation trajectories.

It is important to note that for case 3, which had a higher distribution variance than case 2, slip activity was almost similar to the expectation from an almost homogeneous distribution (case 1). This is because, the systems with higher dislocation densities are different in the two cases. This indicates that the influence is not solely dependent on the magnitude of the variance, but also on which particular systems have higher pre-existing dislocation densities.

This can be reasoned as follows: The distribution of high pre-existing dislocation content on forest systems influences hardening, by imposing barriers to the primary slip system via dislocation interactions. Depending on the amount of particular forest dislocation content, the tensile axis orientation can change to follow alternate paths to continue plastic deformation.

The true stress–strain curves from the simulations are compared to the reference experiment in Fig. 4.14. Case 4, which had a high variance of the log-normal distribution, as well as different primary slip activity shows a higher yield and flow stress compared to the other cases. This can be explained as follows: For a given orientation during tension, if the slip system with highest RSS has a lower dislocation population compared to its forests, the flow-stress increases to activate new sources for plastic deformation to progress. The matching of experimental measurements, however, is still not captured in this exercise.

slip system index	slip system	Schmid factor
1	$(0\,1\,1)[1\,\bar{1}\,1]$	0.0004
2	$(0\,1\,1)[\bar{1}\,\bar{1}\,1]$	0.0007
3	$(0\,\bar{1}\,1)[1\,1\,1]$	0.1193
4	$(0\,\bar{1}\,1)[\bar{1}\,1\,1]$	0.1196
5	$(1\,0\,1)[\bar{1}\,1\,1]$	0.3304
6	$(1\,0\,1)[\bar{1}\,\bar{1}\,1]$	0.431
7	$(\bar{1}\,0\,1)[1\,1\,1]$	0.4493
8	$(\bar{1}\,0\,1)[1\,\bar{1}\,1]$	0.3121
9	$(1\,1\,0)[\bar{1}\,1\,1]$	0.45
10	$(1\,1\,0)[\bar{1}\,1\,\bar{1}]$	0.3117
11	$(\bar{1}\,1\,0)[1\,1\,1]$	0.33
12	$(\bar{1}\,1\,0)[1\,1\,\bar{1}]$	0.4317
13	$(2\,1\,1)[\bar{1}\,1\,1]$	0.4506
14	$(\bar{2}\,1\,1)[1\,1\,1]$	0.45
15	$(2\,\bar{1}\,1)[1\,1\,\bar{1}]$	**0.4981**
16	$(2\,1\,\bar{1})[1\,\bar{1}\,1]$	0.3602
17	$(1\,2\,1)[1\,\bar{1}\,1]$	0.1798
18	$(\bar{1}\,2\,1)[1\,1\,\bar{1}]$	0.2497
19	$(1\,\bar{2}\,1)[1\,1\,1]$	0.1217
20	$(1\,2\,\bar{1})[\bar{1}\,1\,1]$	0.3289
21	$(1\,1\,2)[1\,1\,\bar{1}]$	0.2484
22	$(\bar{1}\,1\,2)[1\,\bar{1}\,1]$	0.1804
23	$(1\,\bar{1}\,2)[\bar{1}\,1\,1]$	0.1217
24	$(1\,1\,\bar{2})[1\,1\,1]$	0.3283

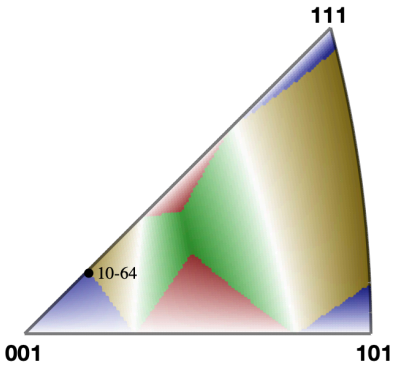

Figure 4.12 Summary of Schmid factors for sample 10-64 in the direction of tension. System 15 with the highest (bold) Schmid factor is the expected primary slip system.

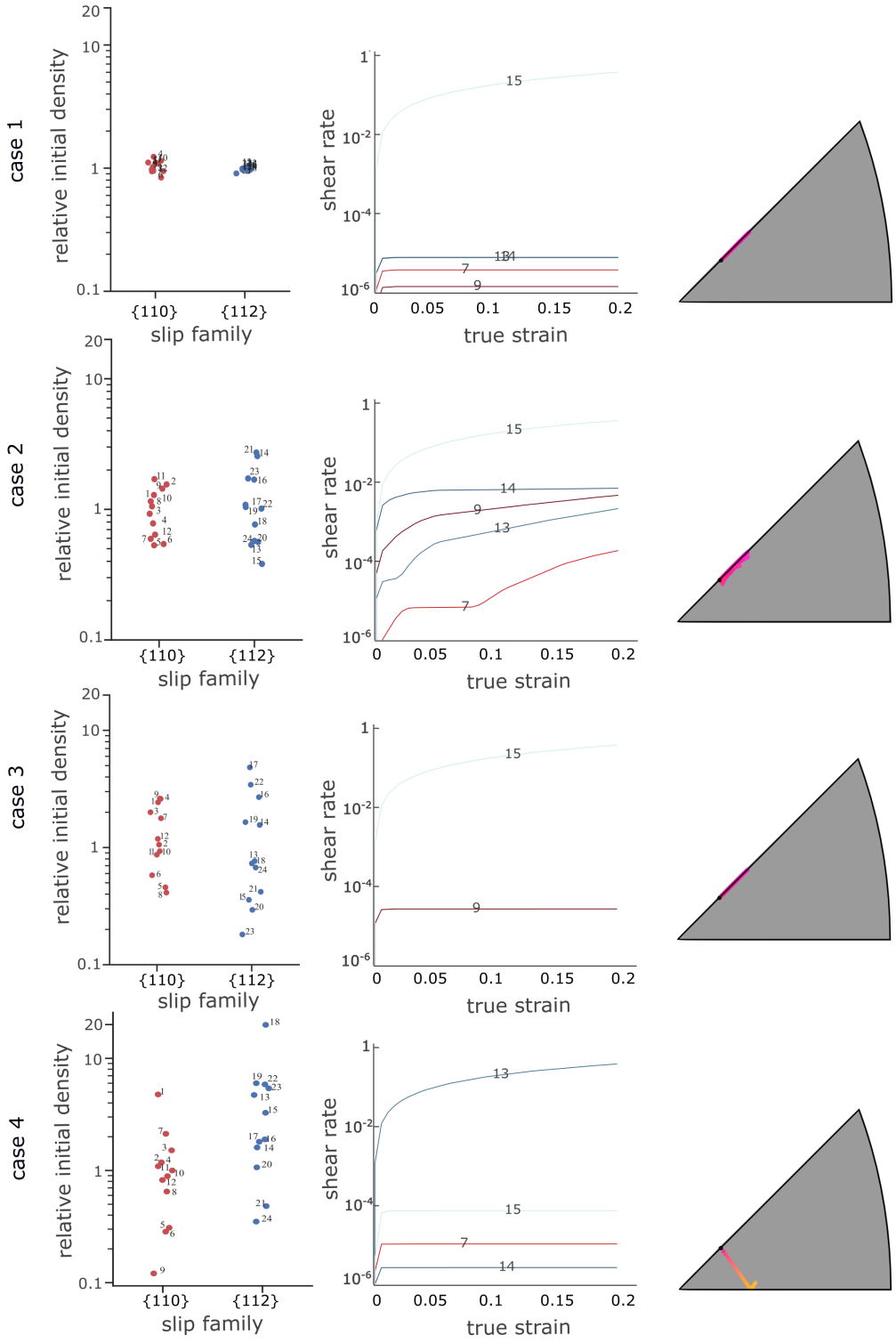

Figure 4.13 Effect of different initial dislocation density distributions (case 1 to case 4) on slip system activity (plotted as shear rate on individual slip systems) and its consequence on the lattice reorientation path (visualized in IPFs).

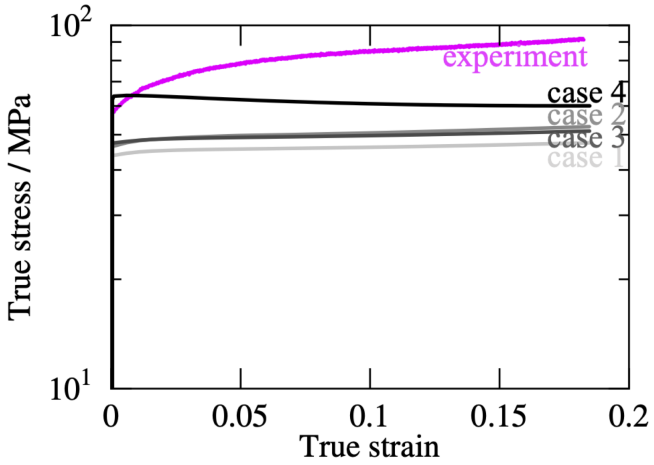

Figure 4.14 Comparison of true stress vs. true strain for the different initial dislocation density distributions simulated (case 1 to case 4) against the experimental measurement for sample 10-64.

4.8.4 Influence of high initial dislocation densities on detrimental forest systems

The mismatch in the prediction of lattice reorientation for sample 2-158 indicates that the expected primary slip system from classical Schmid factor calculations (assuming equal dislocation densities on all slip systems) is not the active slip system in reality. This discrepancy can potentially be due to the presence of higher pre-existing dislocation densities on systems that act as potent forests to the expected primary slip, based on inferences from the preceding section. Forest systems pose as barriers to the expected primary system, thus activating secondary or tertiary slip systems that may follow different reorientation paths.

This hypothesis is tested by identifying the forest slip systems for the expected primary slip system and increasing their relative dislocation densities. Forest systems are selected based on systems having higher values of interaction strengths with the expected primary slip system. These correspond to the collinear reactions between different slip systems sharing the same Burgers vector as the primary slip system. Figure 4.15 shows the Schmid factors and the dislocation interaction coefficients for sample 2-158.

From Fig. 4.15, it can be seen that systems 2, 6, 15, 18, and 21 are prominent forests due to higher interaction strengths with the primary slip system 12, with the highest Schmid factor. System 2 and 6 with the same Burgers vector as system 12, form collinear $\{1\,1\,0\}$ – $\{1\,1\,0\}$ interactions. System 15 and 18 similarly form collinear $\{1\,1\,0\}$ – $\{1\,1\,2\}$ interactions. System 21 which has a slip plane perpendicular to system 12, forms the strongest collinear interaction.

The influence of increasing the relative initial densities of forest systems by a factor of 2, 5, and 10 on slip system activity (as shear rates on slip systems) and its associated lattice reorientation is presented in Fig. 4.16

It can be seen from case 1 (homogeneous distribution) that sample 2-158 expects $\{1\,1\,0\}$ dominant single slip activity on slip system 12, with a competing Schmid factor on $\{1\,1\,2\}$ slip system 15. However, when the forest systems have double the dislocation density in case 2, the shear rates on these slip systems are flipped, making system 15 more active than system 12. The lattice reorientation, however, remains the same because both systems share the same Burgers vector. In

slip system index	slip system	Schmid factor	interaction coefficient
1	$(0\,1\,1)[1\,\bar{1}\,1]$	0.1761	0.245
2	$(0\,1\,1)[\bar{1}\,\bar{1}\,1]$	0.1393	**0.825**
3	$(0\,\bar{1}\,1)[1\,1\,1]$	0.0686	0.205
4	$(0\,\bar{1}\,1)[\bar{1}\,1\,1]$	0.2468	0.285
5	$(1\,0\,1)[\bar{1}\,1\,1]$	0.1267	0.245
6	$(1\,0\,1)[\bar{1}\,\bar{1}\,1]$	0.3461	**0.825**
7	$(\bar{1}\,0\,1)[1\,1\,1]$	0.0192	0.205
8	$(\bar{1}\,0\,1)[1\,\bar{1}\,1]$	0.2385	0.285
9	$(1\,1\,0)[\bar{1}\,1\,1]$	0.1201	0.310
10	$(1\,1\,0)[\bar{1}\,1\,\bar{1}]$	0.4146	0.310
11	$(\bar{1}\,1\,0)[1\,1\,1]$	0.0494	0.009
12	$(\bar{1}\,1\,0)[1\,1\,\bar{1}]$	**0.4853**	0.009
13	$(2\,1\,1)[\bar{1}\,1\,1]$	0.0038	0.20
14	$(\bar{2}\,1\,1)[1\,1\,1]$	0.0174	0.175
15	$(2\,\bar{1}\,1)[1\,1\,\bar{1}]$	0.48	**0.64**
16	$(2\,1\,\bar{1})[1\,\bar{1}\,1]$	0.3771	0.25
17	$(1\,2\,1)[1\,\bar{1}\,1]$	0.3411	0.20
18	$(\bar{1}\,2\,1)[1\,1\,\bar{1}]$	0.3606	**0.64**
19	$(1\,\bar{2}\,1)[1\,1\,1]$	0.0681	0.175
20	$(1\,2\,\bar{1})[\bar{1}\,1\,1]$	0.2118	0.25
21	$(1\,1\,2)[1\,1\,\bar{1}]$	0.1194	**0.90**
22	$(\bar{1}\,1\,2)[1\,\bar{1}\,1]$	0.0361	0.265
23	$(1\,\bar{1}\,2)[\bar{1}\,1\,1]$	0.2157	0.265
24	$(1\,1\,\bar{2})[1\,1\,1]$	0.0507	0.2025

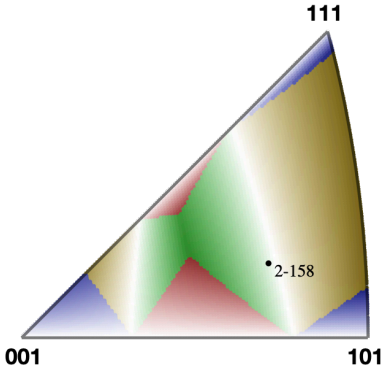

Figure 4.15 Summary of Schmid factors for sample 2-158 in the direction of tension. System 12 with the highest Schmid factor is the expected primary slip system. The interaction coefficients of each slip system with 12 are presented in column 4, with the collinear interactions in bold.

case 3, when the forest systems have 5 times more density than the reference, system 10 overtakes system 12, however, it is still the secondary system by two orders of magnitude. Therefore, the lattice reorientation is still dominated by slip activity on the most active system 15. In case 4, the forest systems have an order of magnitude higher dislocation densities. In this situation, tertiary system 10 with a different Burgers vector becomes the most active slip system, thus resulting in a different lattice reorientation.

This exercise demonstrates that the range of acceptable relative densities of barrier forests is low, since twice the amount already leads to different slip system activity. Overall, the investiga-

tions from using non-uniform initial dislocation densities in simulations indicate that slip activity can be non-unique in single crystal experiments of unknown pre-existing dislocation contents.

The true stress–strain curves from the simulations are compared to the reference experiment in Fig. 4.17. Case 4, which had a high variance of the log-normal distribution as well as different primary slip activity, shows a higher yield and flow stress compared to the other cases. This observation is the same as observed in the previous exercise.

Inferences from the exercises of varying the initial dislocation density distributions indicate that a numerical study is needed to clearly understand the relation between non-uniform pre-existing dislocation density distributions and non-unique outcomes of slip activity and lattice reorientation. This is discussed next, in Chapter 5.

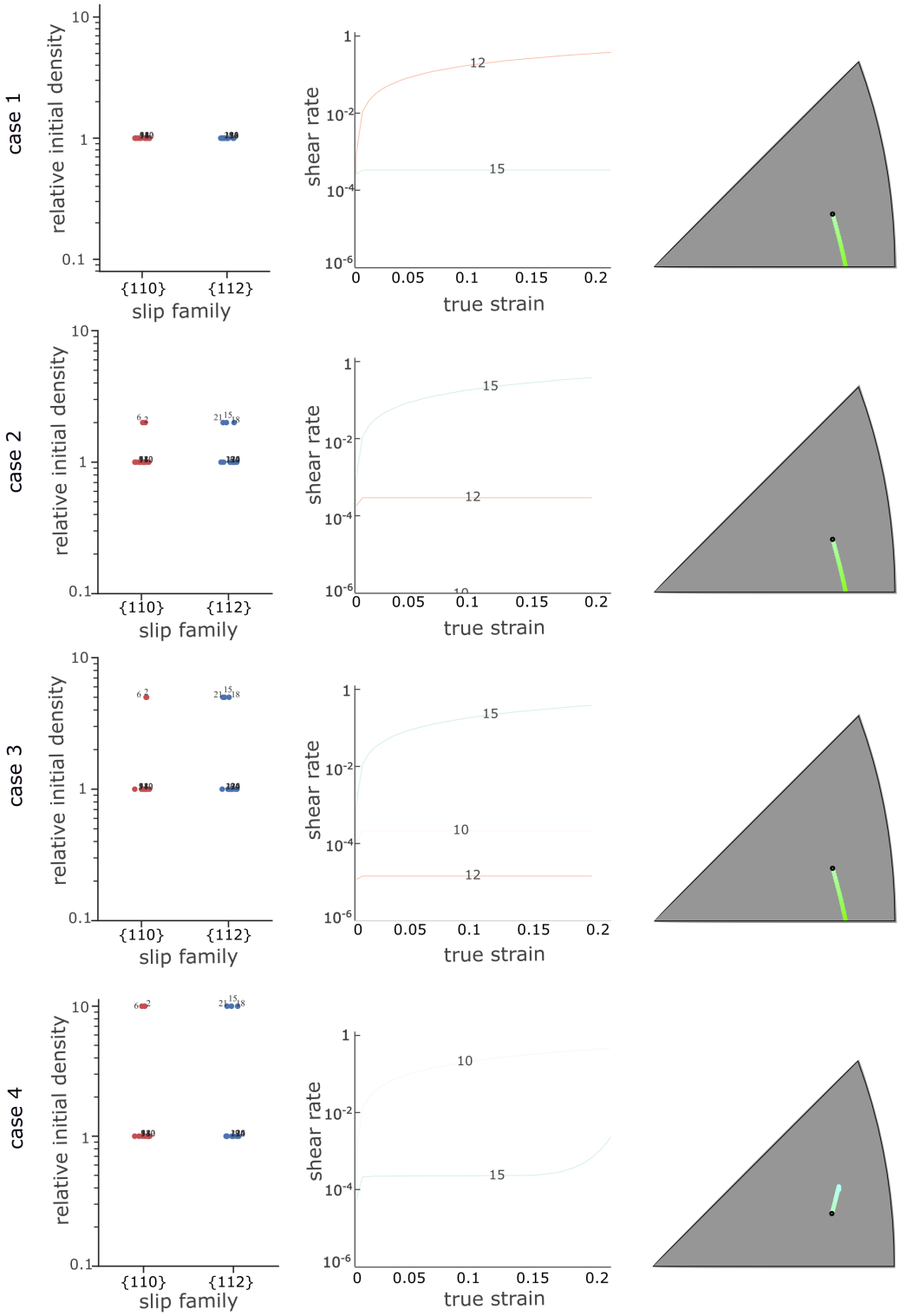

Figure 4.16 Effect of different initial dislocation density distributions (case 1 to case 4) on slip system activity (plotted as shear rate on individual slip systems) and its consequence on the crystal's re-orientation path.

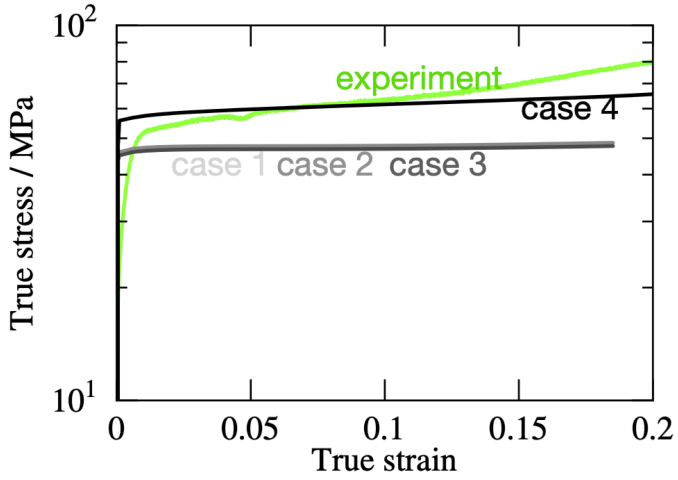

Figure 4.17 Comparison of true stress vs. true strain for the different initial dislocation density distributions simulated (case 1 to case 4) against the experimental measurement for sample 2-158.

CHAPTER 5

STUDY OF SLIP SYSTEM ACTIVITY IN SINGLE CRYSTAL NB

A BCC dislocation mechanics-based modeling approach was used to predict the lattice re-orientation and stress–strain response of single crystal Nb in Chapter 4. Simulations of the newly designed single crystal uniaxial deformation experiments revealed that the stress–strain and lattice re-orientation behavior is not convincingly captured for many orientations. This motivated a systematic investigation of the source of these discrepancies. The primary state variable used in a dislocation mechanics-based CP model is the dislocation density. The model assumes a homogeneous distribution of pre-existing dislocation densities on all slip systems, however, this is not the case in real samples. Since it is impractical to measure the pre-existing dislocation distribution on individual slip systems in a sample, it becomes necessary to know the limit of variability in the pre-existing dislocation densities among the slip systems in a sample, which can be used for successful crystal plasticity predictions using dislocation mechanics-based model. The effect of non-uniform initial dislocation density distributions on slip activity is investigated using a numerical study detailed in this chapter. The developed numerical tool can potentially be used to study the same effect for crystal structures other than BCC, making it a powerful analysis tool for any single crystal experiment.

5.1 Numerical methodology to study slip activity in single crystal Nb

The motivation of this numerical study is to investigate the stability of unique slip activity in BCC metals when the pre-existing dislocation density distribution is non-uniform across their 24 slip systems. To demonstrate this, 6 different cases of pre-existing dislocation density distributions (d0, d1, d2, d3, d4, and d5) were considered. The dislocation density distributions d0 to d5 are log-normal with mean dislocation densities of 1×10^{11} m^{-2} and their variances increasing from 1 to $e = 2.718$. Figure 5.1 shows the cumulative probability of d0 to d5. For each of the 6 distributions, 5000 different randomly generated instances of dislocation density distributions were used to calculate Schmid factors (for 12 $\{1\,1\,0\}$ and 12 $\{1\,1\,2\}$ slip systems) for all possible in-plane orientations. Due to the asymmetric nature of the dislocation interactions in BCC metals employed in

the dislocation mechanics-based model described in Section 4.4.1, the Schmid factor is normalized by the square root of the sum of the interaction coefficients of the 24 slip systems.

A simple algorithm of how the code works is outlined below:

1. Initialize distribution case by providing the mean and variance of the log-normal distribution.
2. Begin loop for first instance of a pre-existing dislocation density distribution. The 24 densities for the slip systems are created here by generating a random instance for the distribution initialized in previous step.
3. Begin an inner loop over all possible in-plane tensile orientations that can be visualized in a standard stereo-graphic triangle IPF. Calculate Schmid factor for each slip system and normalize by the square root of the sum of the interaction coefficients of the 24 slip systems.
4. Identify the 2 slip systems with the highest Schmid factors. Identify their respective slip family index as $\{1\,1\,0\}$ or $\{1\,1\,2.\}$
5. Based on the combination of their indexes, each orientation is identified as:
    - $\{1\,1\,0\}/\{1\,1\,0\}$ which means highest Schmid factor belongs to $\{1\,1\,0\}$ and second highest Schmid factor belongs to $\{1\,1\,0\}$.
    - $\{1\,1\,0\}/\{1\,1\,2\}$ which means highest Schmid factor belongs to $\{1\,1\,0\}$ and second highest Schmid factor belongs to $\{1\,1\,2\}$.
    - $\{1\,1\,2\}/\{1\,1\,0\}$ which means highest Schmid factor belongs to $\{1\,1\,2\}$ and second highest Schmid factor belongs to $\{1\,1\,0\}$.
    - $\{1\,1\,2\}/\{1\,1\,2\}$ which means highest Schmid factor belongs to $\{1\,1\,2\}$ and second highest Schmid factor belongs to $\{1\,1\,2\}$.
6. Save the identification of each orientation in a tracker.
7. Repeat step 2 to step 6 for 5000 different instances of the distribution.
8. The tracker for each orientation reveals if it had unique slip activity for all 5000 instances or not.

9. Non-unique orientations are further categorized based on how many combinations (up to 4) outlined in step 5 were realized for the 5000 instances.

10. Repeat from step 1 for next distribution.

The results from the calculations are used to estimate the highest variance of an initial dislocation density distribution that still results in unique slip activity for tensile orientations.

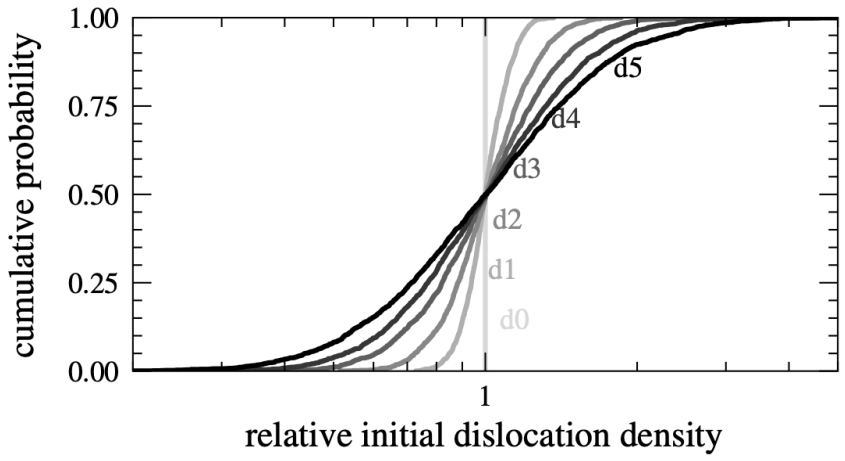

Figure 5.1 Cumulative probability distribution of relative dislocation densities, used in the different cases.

5.2 Results: Effect of non-uniform pre-existing dislocation density distribution

The effect of having a non-uniform distribution of pre-existing dislocation density on the most active slip families and their corresponding slip systems is visualized using inverse pole figures (IPFs).

5.2.1 Effect on unique pair of highest active slip families

The 4 possible combinations of most active slip family pairs are:

- {1 1 0}/{1 1 0}
- {1 1 0}/{1 1 2}
- {1 1 2}/{1 1 0}
- {1 1 2}/{1 1 2}

It was found that the combination of the most active slip families is unique for every tensile orientation when the distribution of pre-existing dislocation densities is uniform (case d0). However, this was not true for non-uniform distributions (cases d1 to d4).

Figure 5.2 demonstrates these findings. Each IPF in the figure shows the results of a particular distribution case (d0 to d5). For each case, orientations with a single outcome for the most active slip family pair (unique orientations) are colored uniquely as indicated in the left legend of Fig. 5.2. Orientations with non-unique outcomes for the most active slip family pair (non-unique orientations) are colored with a shade of gray depending on the number of combinations (upto 4) observed while testing 5000 different instances. Lighter shades have more possibilities than darker shades of gray and the respective number of possibilities are indicated in the right legend of Fig. 5.2. Orientations with a single outcome for the most active slip family pair (unique orientations) are colored uniquely as indicated in the left legend of Fig. 5.2. It is evident that the number of non-unique orientations (indicated by growing areas of gray) increases as the variance of the distribution. For distribution case d4 with a variance of e, all orientations are non-unique, indicating that slip activity is completely unpredictable.

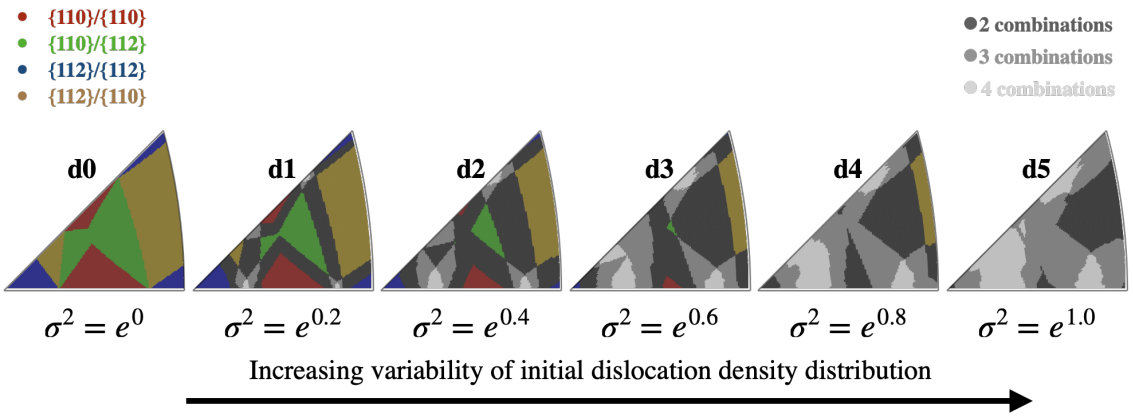

Figure 5.2 Effect of non-uniform pre-existing dislocation density distributions on unique pair of highest active slip families. From left to right: the variance of the dislocation density distribution increases and their values are indicated (d0 to d5 in Fig. 5.1). Unique orientations are colored according to the left legend. Non-unique orientations are colored with a shade of gray depending on the number of combinations of highest active slip family pairs (up to 4) observed for that orientation.

These findings demonstrate that when the exact pre-existing dislocation density distribution

(on a per slip system basis) is unknown, simulations of non-unique (gray) orientations can result in two or more outcomes of slip activity (and consequently the lattice re-orientation and stress-strain response) which can create discrepancies between measured and simulated experiments.

5.2.2 Effect on consistent most active slip system

The effect of having a non-uniform distribution of pre-existing dislocation density on the top-most active slip system in the $\{1\,1\,0\}$ family is visualized using IPFs. The 12 $\{1\,1\,0\}$ slip systems are 12 visualized with different shades of red. For a given orientation, if the most active $\{1\,1\,0\}$ slip system is unique, it is colored with it's respective shade of red, if not, the orientation is white.

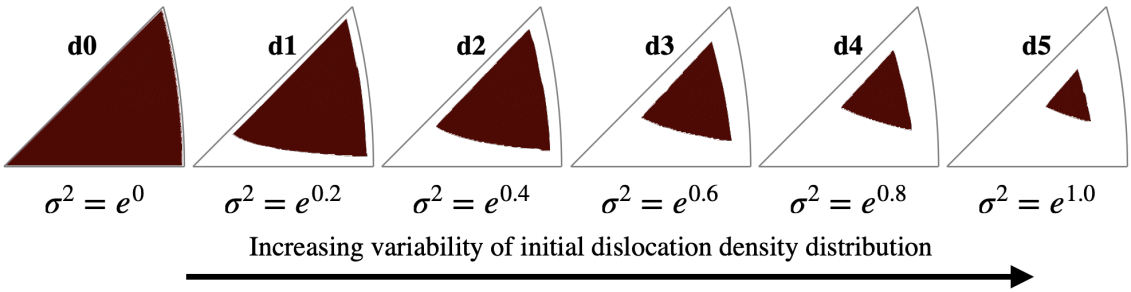

Figure 5.3 IPF visualization of orientations with consistent most active $\{1\,1\,0\}$ slip system. From left to right: the variance of the dislocation density distribution increases and their values are indicated (d0 to d5 in Fig. 5.1). Unique orientations are colored with a respective shade of red. Non-unique orientations are white.

From Fig. 5.3 it is clear that there is one unique most active $\{1\,1\,0\}$ slip system. Non-unique orientations (white areas) are present for non uniform distributions and grow with increasing distribution variance.

Next, the effect of having a non-uniform distribution of pre-existing dislocation density on the top-most active slip system in the $\{1\,1\,2\}$ family is visualized using IPFs. The 12 $\{1\,1\,0\}$ slip systems are visualized with 12 different shades of blue. For a given orientation, if the most active $\{1\,1\,0\}$ slip system is unique, it is colored with it's respective shade of blue, if not, the orientation is white.

From Fig. 5.4 it is clear that there are 2 unique most active slip systems in the $\{1\,1\,2\}$ family. Non-unique orientations (white areas) are present for non uniform distributions and grow with increasing distribution variance.

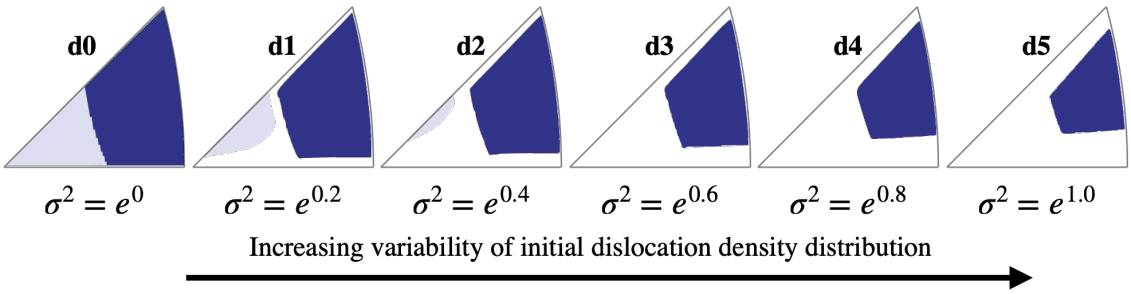

Figure 5.4 IPF visualization of orientations with consistent most active $\{1\,1\,2\}$ slip system. From left to right: the variance of the dislocation density distribution increases and their values are indicated (d0 to d5 in Fig. 5.1). Unique orientations are colored with a respective shade of blue. Non-unique orientations are white.

5.3 Key findings

When the pre-existing dislocation density distribution is non-uniform, not all tensile orientations exhibit unique slip activity during deformation. Slip activity is expressed by identifying the slip systems with two highest Schmid factors and testing their reproducibility - first in terms of slip family pairs, then in terms of consistent highest active $\{1\,1\,0\}$ and $\{1\,1\,2\}$ slip systems. When increasing distribution variances are considered, the number of tensile orientations that have reproducible slip activity reduce. This may be one of the reasons that can explain the discrepancies between experimental samples with unknown pre-existing dislocation densities and their corresponding simulations which assume uniform distribution. These findings indicate that the precise matching of single crystal deformation is highly likely to be an elusive goal when the distribution of pre-existing dislocation densities is unknown.

CHAPTER 6

SUMMARY

A new investigation of the mechanical properties of high-purity Niobium single crystals is presented.

Based on a given set of a few grain orientations within a large-grain Nb disk, a methodology to produce deformation samples of (almost) arbitrary crystallographic tensile direction was developed. This allowed investigation of specific tensile directions of interest under multiple strain rates. At quasi-static strain rates (up to $1 \times 10^{-2}\,\mathrm{s}^{-1}$), a stronger dependence of yield stress and strain-hardening behavior on the crystallographic tensile direction was observed. For most orientations, yield is succeeded by a distinct hardening followed by a decrease in flow stress, giving rise to a "bump" in the stress–strain curve. Crystal rotations at fracture were compared for the different orientations using scanning electron microscopy to provide EBSD orientation maps. A rotation toward the terminal stable $[1\,1\,1]$ orientation anticipated from classical Schmid factor analysis was measured for several samples; a few samples, however, re-oriented differently. Thus, the origin of this apparent inconsistency, i.e., why the classical Schmid expectation is not universally fulfilled, has been investigated.

To that extent, a dislocation mechanics-based crystal plasticity model was used to simulate the stress–strain response and crystal re-orientation of niobium single crystals under uniaxial tension. The model is based on thermally activated dislocation motion as described by Cereceda et al. [10]. The dislocation density evolution is modeled in terms of dislocation generation, interactions, and annihilation following Blum and Eisenlohr [8]. The model is parameterized based on new material-specific dislocation interaction coefficients obtained from discrete dislocation dynamics simulations [55]. The model has been implemented in the open-source software DAMASK (Düsseldorf Advanced Material Simulation Kit) [74].

To take advantage of a numerically efficient (Fourier-based) numerical solution scheme provided in DAMASK, single-crystalline samples of dogbone shape were discretized on a regular grid with a resolution of $300 \times 44 \times 10$. To circumvent the strict periodicity constraint imposed by that

solution scheme on the hexahedral simulation box, those grid points outside of the dogbone geometry were considered to be of a dilatational material with comparatively low stiffness and strength [56]. During test simulations, it was found that the compromise between diminishing stress in this 'buffer layer' and the associated increasing computational cost (or even non-convergence) was reached by adjusting the elastic constant C_{11} and the flow stress by 3 orders of magnitude relative to Nb—as opposed to one and two orders as originally suggested by Maiti and Eisenlohr [56]. Due to the computationally expensive nature of dogbone simulations, a simplified geometry with just a rectangular block of gage section under the same boundary conditions as the full dogbone was used for computational investigations.

The realistic boundary conditions induced by the dogbone geometry resulted in spatially heterogeneous slip response (such as slip localization), similar to experimental observations. Neither the geometrically faithful dogbone geometry nor the simplistic fully periodic geometry was able to consistently match the yield stress as well as the detailed strain hardening behavior across multiple tensile orientations. Nevertheless, the overall trends were comparable between measurements and simulations. In contrast to the experimental observations, the dogbone and simplified simulations *always* followed the expected reorientation when the initial dislocation content assumed in the model was homogeneously distributed across all available slip systems. Hence, whether the discrepancies between the simulated and experimental stress–strain and crystal re-orientations are connected to the specific distribution of initial dislocation density was investigated for two orientations for which a non-expected reorientation was measured. Simulations starting from log-normal distributions of dislocation density with increasing variance showed that the resulting slip activity and associated crystal re-orientation becomes more and more non-unique with increasing variance. This behavior was explained by the reduced activity of the expected slip system due to relatively high dislocation density on systems that pose potent forest obstacles.

This general hypothesis was confirmed by deliberately designing dislocation density configurations containing a high density of dislocations that act as a forest to the expected primary slip system. Results from these investigations showed that, specifically, forest systems having high

interaction strengths with the primary slip system can act as effective barriers, thereby inducing the activation of secondary and/or tertiary slip systems that cause re-orientation different from the expectation.

An exhaustive numerical study probing thousands of initial dislocation density distributions was condensed into inverse pole figure (IPF) maps that chart the range of crystallographic tensile directions for which unique outcomes can be expected despite a given variability in the pre-existing dislocation density distribution. Five different log-normal density distributions with mean dislocation densities of $1 \times 10^{11}\ \mathrm{m}^{-2}$ and variances of increasing from 1 to e were studied. Visualization of the range of orientations with unique dominant slip systems for each distribution shows that the fraction of non-unique orientations increases as the extent of variance of the log-normal distribution of the dislocation density increases from 1 to e, making the slip activity for all tensile orientations totally unpredictable for higher variances.

These findings indicate that the precise matching of measured single crystal deformation with simulations following dislocation mechanics-based CP models is very likely an elusive goal, was long as the distribution of pre-existing dislocation densities in the sample is unknown and suspected to be heterogeneous.

CHAPTER 7

CONCLUSIONS AND FUTURE WORK

7.1 Key conclusions

- The classical Schmid expectation of lattice reorientation was not universally fulfilled in some of the single-crystal Nb orientations deformed in tension.
- In some orientations, yield is succeeded by a distinct hardening followed by a decrease in flow stress, giving rise to a "bump" in the measured stress–strain curve.
- Using a dogbone geometry with realistic boundary conditions can capture spatially heterogeneous slip response, similar to experimental observations (such as slip localization), however, simplified geometries can only predict the overall lattice reorientation.
- The discrepancies between the simulated and experimental stress–strain and crystal re-orientations are connected to the specific distribution of initial dislocation density.
- When the distribution of pre-existing dislocation densities on available slip systems in a single crystal is non-homogeneous, slip activity and associated crystal reorientation are not unique.
- There are no tensile orientations with a unique outcome for slip activity above a distribution variance of e when log-normal distributions of dislocation densities are considered.
- The precise matching of single crystal deformation cannot be expected from dislocation mechanics-based CP models as long as the distribution of pre-existing dislocation densities in the sample is unknown and suspected to be heterogeneous.

7.2 Recommendations for future work

- The model used in this work considers only screw glide dislocation kinetics, based on the fact that edge dislocations move very rapidly in BCC metals, whereas the annihilation kinetics is based on climb of edge segments. However, it may be beneficial to incorporate both dislocation characters and all of their associated kinetics in the constitutive description.

Particularly, cross-slipping of screw dislocations should be included in the constitutive law. The availability of a many slip planes sharing a common $\langle 1\,1\,1 \rangle$ direction, makes cross-slip very likely in BCC materials, thereby having the potential to further improve the constitutive description.

- The formulated dislocation mechanics-based constitutive description should be validated not based on (non-unique and hence unreliable) single-crystal experiments, but on (statistical) evaluations of poly-crystalline deformation experiments.
- It will be useful to study, in detail, the sensitivity of simulation convergence on the elastic stiffness constants and flow stresses of the dilatational layer, for various materials.
- Methods to measure dislocation density on individual slip systems in single crystals using synchrotron or neutron diffraction methods could provide a means to quantify the fraction of dislocations on each slip system, and make it possible to compare experiments meaningfully with simulations.

BIBLIOGRAPHY

[1] Deformation process in single crystals. https://www.tec-science.com/material-science/ductility-of-metals/deformation-process-in-single-crystals-stress-strain-curve/.

[2] Shrirang Abhyankar and BF Smith. Petsc: An advanced math and computing framework for rapidly developing parallel smart grid applications. In *Proceedings of the IEEE PES General Meeting*, volume 4, page 6, 2013.

[3] F Ackermann, H Mughrabi, and A Seeger. Temperature- and strain-rate dependence of the flow stress of ultrapure niobium single crystals in cyclic deformation. *Acta Metallurgica*, 31 (9):1353–1366, 1983. ISSN 0001-6160. doi:10.1016/0001-6160(83)90006-8.

[4] C.Z. Antoine. Materials and surface aspects in the development of srf niobium cavities; eucard editorial series on. 2012.

[5] Derek Baars. *Investigation of active slip systems in high purity single crystal niobium*. PhD thesis, Michigan State University, 2013.

[6] Barry Barish and James E. Brau. The international linear collider. *International Journal of Modern Physics A*, 28(27):1330039, 2013. doi:10.1142/S0217751X13300391.

[7] TR Bieler, NT Wright, F Pourboghrat, C Compton, KT Hartwig, D Baars, A Zamiri, S Chandrasekaran, P Darbandi, H Jiang, et al. Physical and mechanical metallurgy of high purity nb for accelerator cavities. *Physical Review Special Topics-Accelerators and Beams*, 13(3): 031002, 2010. doi:10.1103/PhysRevSTAB.13.031002.

[8] W. Blum and P. Eisenlohr. Dislocation mechanics of creep. *Materials Science and Engineering: A*, 510-511:7–13, 2009. ISSN 0921-5093. doi:10.1016/j.msea.2008.04.110. 11th International Conference of Creep and Fracture of Engineering Materials and Structures, CREEP 2008.

[9] D. K. Bowen, J. W. Christian, and G. Taylor. Deformation properties of niobium single crystals. *Canadian Journal of Physics*, 45(2):903–938, 1967. doi:10.1139/p67-069.

[10] David Cereceda, Martin Diehl, Franz Roters, Dierk Raabe, J Manuel Perlado, and Jaime Marian. Unraveling the temperature dependence of the yield strength in single-crystal tungsten using atomistically-informed crystal plasticity calculations. *International Journal of Plasticity*, 78:242–265, 2016. doi:10.1016/j.ijplas.2015.09.002.

[11] Julien Chaussidon, Marc Fivel, and David Rodney. The glide of screw dislocations in bcc fe: atomistic static and dynamic simulations. *Acta materialia*, 54(13):3407–3416, 2006. doi:10.1016/j.actamat.2006.03.044.

[12] J.W. Christian. Some surprising features of the plastic deformation of body-centered cubic

metals and alloys. *Metall Mater Trans A*, 14:1237–1256, 1983. doi:10.1007/BF02664806.

[13] Richard Courant et al. Variational methods for the solution of problems of equilibrium and vibrations. *Lecture notes in pure and applied mathematics*, pages 1–1, 1994.

[14] J.-F. Croteau, E. Pai Kulyadi, C. Kale, D. Siu, D. Kang, A.T. Perez Fontenla, E. García-Tabarés Valdivieso, T.R. Bieler, P. Eisenlohr, K.N. Solanki, D. Balint, P.A. Hooper, S. Atieh, N. Jacques, and E. Cantergiani. Effect of strain rate on tensile mechanical properties of high-purity niobium single crystals for srf applications. *Materials Science and Engineering: A*, 797:140258, 2020. ISSN 0921-5093. doi:10.1016/j.msea.2020.140258.

[15] TWJ De Geus, J Vondřejc, J Zeman, RHJ Peerlings, and MGD3627184 Geers. Finite strain fft-based non-linear solvers made simple. *Computer Methods in Applied Mechanics and Engineering*, 318:412–430, 2017.

[16] Jörg Diehl. Zugverformung von kupfer-einkristallen. *International Journal of Materials Research*, 47(5):331–343, 1956.

[17] Martin Diehl. A spectral method using fast fourier transform to solve elastoviscoplastic mechanical boundary value problems. *TU München: München, Germany*, 2010.

[18] Martin Diehl. *High-resolution crystal plasticity simulations*. Apprimus Wissenschaftsverlag, 2016.

[19] George E. Dieter. *Mechanical metallurgy*. McGraw-Hill series in materials science and engineering. McGraw-Hill, 1986. ISBN 0070168938.

[20] John E Dora and Stanley Rajnak. Nucleation of kink pairs and the peierls' mechanism of plastic deformation. *Trans. Aime*, 230:1052–1064, 1963.

[21] M. Duesbery, R. Foxall, and P. Hirsch. The plasticity of pure niobium single crystal. *J. Phys. Colloques*, 27:C3–193–C3–204, 1966. doi:10.1051/jphyscol:1966325.

[22] M and-S Duesbery and V Vitek. Plastic anisotropy in bcc transition metals. *Acta Materialia*, 46(5):1481–1492, 1998. doi:10.1016/S1359-6454(97)00367-4.

[23] MS Duesbery. On non-glide stresses and their influence on the screw dislocation core in body-centred cubic metals i. the peierls stress. *Proceedings of the Royal Society of London. A. Mathematical and Physical Sciences*, 392(1802):145–173, 1984.

[24] MS Duesbery and RA Foxall. A detailed study of the deformation of high purity niobium single crystals. *Philosophical Magazine*, 20(166):719–751, 1969. doi:10.1080/14786436908228040.

[25] MS Duesbery and RA Foxall. A detailed study of the deformation of high purity niobium

single crystals. *Philosophical Magazine*, 20(166):719–751, 1969.

[26] P. Eisenlohr, M. Diehl, R.A. Lebensohn, and F. Roters. A spectral method solution to crystal elasto-viscoplasticity at finite strains. *International Journal of Plasticity*, 46:37–53, 2013. ISSN 0749-6419. doi:10.1016/j.ijplas.2012.09.012. Microstructure-based Models of Plastic Deformation.

[27] A. Ermakov, I. Jelezov, X. Singer, W. Singer, G.B. Viswanathan, V. Levit, H.L. Fraser, H. Wen, and M. Spiwek. Physical properties and structure of large grain/single crystal niobium for superconducting RF cavities. *Journal of Physics: Conference Series*, 97:012014, feb 2008. doi:10.1088/1742-6596/97/1/012014.

[28] MW Finnis and JE Sinclair. A simple empirical n-body potential for transition metals. *Philosophical Magazine A*, 50(1):45–55, 1984.

[29] R. A. Foxall, M. S. Duesbery, and P. B. Hirsch. The deformation of niobium single crystals. *Canadian Journal of Physics*, 45(2):607–629, 1967. doi:10.1139/p67-052.

[30] RA Foxall and CD Statham. Dislocation arrangements in deformed single crystals of niobium-molybdenum alloys and niobium-9 at.% rhenium. *Acta Metallurgica*, 18(11):1147–1158, 1970.

[31] P Franciosi. Glide mechanisms in bcc crystals: an investigation of the case of α-iron through multislip and latent hardening tests. *Acta Metallurgica*, 31(9):1331–1342, 1983. doi:10.1016/0001-6160(83)90004-4.

[32] Ei-ichi Furubayashi. Behavior of dislocations in fe-3% si under stress. *Journal of the Physical Society of Japan*, 27(1):130–146, 1969.

[33] H Gough. The behaviour of a single crystal of α-iron subjected to alternating torsional stresses. *Proceedings of the Royal Society of London. Series A, Containing Papers of a Mathematical and Physical Character*, 118(780):498–534, 1928.

[34] R Gröger and V Vitek. Breakdown of the schmid law in bcc molybdenum related to the effect of shear stress perpendicular to the slip direction. In *Materials Science Forum*, volume 482, pages 123–126. Trans Tech Publ, 2005.

[35] John Price Hirth and Jens Lothe. *Theory of dislocations.* Wiley, 1982. ISBN 0471091251.

[36] D Hull, JF Byron, and FW Noble. Orientation dependence of yield in body-centered cubic metals. *Canadian Journal of Physics*, 45(2):1091–1099, 1967.

[37] Derek Hull and D. J. Bacon. *Introduction to dislocations.* Butterworth-Heinemann, 2001. ISBN 0750646810.

[38] K Ito and V Vitek. Atomistic study of non-schmid effects in the plastic yielding of bcc metals. *Philosophical Magazine A*, 81(5):1387–1407, 2001.

[39] S.R. Kalidindi, C.A. Bronkhorst, and L. Anand. Crystallographic texture evolution in bulk deformation processing of fcc metals. *Journal of the Mechanics and Physics of Solids*, 40(3): 537–569, 1992. ISSN 0022-5096. doi:10.1016/0022-5096(92)80003-9.

[40] Di Kang. *Characterization of microstructure and slip behavior of niobium used to fabricate accelerator cavities*. PhD thesis, Michigan State University, 2019.

[41] Di Kang, Derek Baars, Thomas Bieler, Chris Compton, Farhang Pourboghrat, and Aboozar Mapar. Study of slip and deformation in high purity single crystal nb for accelerator cavities. In *MISSING*, 2015.

[42] Sven Kaßbohm, Wolfgang H Müller, and Robert Feßler. Improved approximations of fourier coefficients for computing periodic structures with arbitrary stiffness distribution. *Computational materials science*, 37(1-2):90–93, 2006.

[43] P. Kneisel, G.R. Myneni, G. Ciovati, J. Sekutowicz, and T. Carneiro. Preliminary results from single crystal and very large crystal niobium cavities. In *Proceedings of the 2005 Particle Accelerator Conference*, pages 3991–3993, 2005. doi:10.1109/PAC.2005.1591693.

[44] P. Kneisel, G. Ciovati, P. Dhakal, K. Saito, W. Singer, X. Singer, and G.R. Myneni. Review of ingot niobium as a material for superconducting radiofrequency accelerating cavities. *Nuclear Instruments and Methods in Physics Research Section A: Accelerators, Spectrometers, Detectors and Associated Equipment*, 774:133–150, 2015. ISSN 0168-9002. doi:10.1016/j.nima.2014.11.083.

[45] U F Kocks. Proc. of the conf. at the 50th anniversary meeting on dislocations and properties of real materials. pages 125–143. The Institute of Metals, 1985.

[46] UF Kocks. The relation between polycrystal deformation and single-crystal deformation. *Metallurgical and Materials Transactions B*, 1(5):1121–1143, 1970.

[47] UF Kocks and R Maddin. Observations on the deformation of niobium. *Acta Metallurgica*, 4(1):91–92, 1956.

[48] Aenne Koester, Anxin Ma, and Alexander Hartmaier. Atomistically informed crystal plasticity model for body-centered cubic iron. *Acta Materialia*, 60(9):3894–3901, 2012.

[49] Ricardo A Lebensohn. N-site modeling of a 3d viscoplastic polycrystal using fast fourier transform. *Acta materialia*, 49(14):2723–2737, 2001.

[50] P.J. Lee, A.A. Polyanskii, A. Gurevich, A.A. Squitieri, D.C. Larbalestier, P.C. Bauer, C. Boffo, and H.T. Edwards. Grain boundary flux penetration and resistivity in large grain

niobium sheet. *Physica C: Superconductivity*, 441(1):126–129, 2006. ISSN 0921-4534. doi:10.1016/j.physc.2006.03.027. Proceedings of the 12th International Workshop on RF Superconductivity.

[51] Hojun Lim, Jay D Carroll, Joseph R Michael, Corbett C Battaile, Shuh Rong Chen, and J Matthew D Lane. Investigating active slip planes in tantalum under compressive load: Crystal plasticity and slip trace analyses of single crystals. *Acta Materialia*, 185:1–12, 2020.

[52] M. Stanley Livingston, John P. Blewett, and D. Keefe. Particle accelerators. *Physics Today*, 15(11):63–63, 1962. doi:10.1063/1.3057863.

[53] F Louchet, LP Kubin, and D Vesely. In situ deformation of bcc crystals at low temperatures in a high-voltage electron microscope dislocation mechanisms and strain-rate equation. *Philosophical Magazine A*, 39(4):433–454, 1979.

[54] R Maddin and NK Chen. Plasticity of columbium single crystals. *Jom*, 5(9):1131–1136, 1953.

[55] Ronan Madec and Ladislas P. Kubin. Dislocation strengthening in fcc metals and in bcc metals at high temperatures. *Acta Materialia*, 126:166–173, 2017. doi:10.1016/j.actamat.2016.12.040.

[56] Tias Maiti and Philip Eisenlohr. Fourier-based spectral method solution to finite strain crystal plasticity with free surfaces. *Scripta Materialia*, 145:37–40, mar 2018. doi:10.1016/j.scriptamat.2017.09.047.

[57] Aboozar Mapar. Crystal plasticity modeling of the deformation of bcc iron and niobium single crystals, 2017.

[58] T. E. Mitchell, R. A. Foxall, and P. B. Hirsch. Work-hardening in niobium single crystals. *The Philosophical Magazine: A Journal of Theoretical Experimental and Applied Physics*, 8 (95):1895–1920, 1963. doi:10.1080/14786436308209081.

[59] Herve Moulinec and Pierre Suquet. A fast numerical method for computing the linear and nonlinear mechanical properties of composites. *Comptes Rendus de l'Académie des sciences. Série II. Mécanique, physique, chimie, astronomie*, 1994.

[60] Egon Orowan. Zur kristallplastizität. i. *Zeitschrift für Physik*, 89(9):605–613, 1934.

[61] Hasan Padamsee. The science and technology of superconducting cavities for accelerators. *Superconductor Science and Technology*, 14(4):R28–R51, mar 2001. doi:10.1088/0953-2048/14/4/202.

[62] Hasan Padamsee. *RF Superconductivity 2010: Science, Technology and Applications*. 2010.

[63] Hasan Padamsee. 50 years of success for SRF accelerators—a review. *Superconductor Science and Technology*, 30(5):053003, apr 2017. doi:10.1088/1361-6668/aa6376.

[64] Hasan Padamsee, Ja Knobloch, and T Hays. *RF Superconductivity for Accelerators*. John Wiley & Sons, 1998.

[65] Rudolf Peierls. The size of a dislocation. In *Selected Scientific Papers Of Sir Rudolf Peierls: (With Commentary)*, pages 273–276. World Scientific, 1997.

[66] Daniel Peirce, Robert J Asaro, and A Needleman. Material rate dependence and localized deformation in crystalline solids. *Acta metallurgica*, 31(12):1951–1976, 1983.

[67] A. A. Polyanskii, P. J. Lee, A. Gurevich, Zu-Hawn Sung, and D. C. Larbalestier. Magneto-optical study high-purity niobium for superconducting rf application. *AIP Conference Proceedings*, 1352(1):186–202, 2011. doi:10.1063/1.3579237.

[68] Sylvain Queyreau, Ghiath Monnet, and Benoît Devincre. Slip systems interactions in alpha-iron determined by dislocation dynamics simulations. *International Journal of Plasticity*, 25 (2):361–377, 2009. doi:10.1016/j.ijplas.2007.12.009.

[69] Dierk Raabe and Kurt Lücke. Rolling textures of niobium and molybdenum. *International Journal of Materials Research*, 85(5):302–307, 1994.

[70] Anthony D Rollett and UF Kocks. A review of the stages of work hardening. *Solid state phenomena*, 35:1–18, 1993.

[71] F Roters, P Eisenlohr, C Kords, DD Tjahjanto, M Diehl, and D Raabe. Damask: the düsseldorf advanced material simulation kit for studying crystal plasticity using an fe based or a spectral numerical solver. *Procedia Iutam*, 3:3–10, 2012.

[72] Franz Roters. Advanced material models for the crystal plasticity finite element method: development of a general cpfem framework. Technical report, Fachgruppe für Materialwissenschaft und Werkstofftechnik, 2011.

[73] Franz Roters, Philip Eisenlohr, Luc Hantcherli, Denny Dharmawan Tjahjanto, Thomas R Bieler, and Dierk Raabe. Overview of constitutive laws, kinematics, homogenization and multiscale methods in crystal plasticity finite-element modeling: Theory, experiments, applications. *Acta materialia*, 58(4):1152–1211, 2010.

[74] Franz Roters, Martin Diehl, Pratheek Shanthraj, Philip Eisenlohr, C Reuber, Su Leen Wong, Tias Maiti, Alireza Ebrahimi, Thomas Hochrainer, H-O Fabritius, et al. Damask–the düsseldorf advanced material simulation kit for modeling multi-physics crystal plasticity, thermal, and damage phenomena from the single crystal up to the component scale. *Computational Materials Science*, 158:420–478, 2019. doi:10.1016/j.commatsci.2018.04.030.

[75] E. Schmid and W. Boas. *Kristallplastizität*. Springer Berlin, Heidelberg, 1935. ISBN 978-3-662-34261-9. doi:10.1007/978-3-662-34532-0.

[76] Matti Schneider, Felix Ospald, and Matthias Kabel. Computational homogenization of elasticity on a staggered grid. *International Journal for Numerical Methods in Engineering*, 105 (9):693–720, 2016.

[77] A Seeger. The temperature and strain-rate dependence of the flow stress of body-centred cubic metals: A theory based on kink–kink interactions. *Zeitschrift fur Metallkunde*, 72(6): 369–380, 1981.

[78] A. Seeger and W. Wasserbäch. Anomalous slip – a feature of high-purity body-centred cubic metals. *physica status solidi (a)*, 189(1):27–50, 2002.

[79] Alfred Seeger. Peierls barriers, kinks, and flow stress: recent progress. *International Journal of Materials Research*, 93(8):760–777, 2002.

[80] Alfred Seeger. Progress and problems in the understanding of the dislocation relaxation processes in metals. *Materials Science and Engineering: A*, 370(1-2):50–66, 2004.

[81] Pratheek Shanthraj, Philip Eisenlohr, Martin Diehl, and Franz Roters. Numerically robust spectral methods for crystal plasticity simulations of heterogeneous materials. *International Journal of Plasticity*, 66:31–45, 2015.

[82] Pratheek Shanthraj, Martin Diehl, Philip Eisenlohr, Franz Roters, and Dierk Raabe. *Spectral Solvers for Crystal Plasticity and Multi-physics Simulations*, pages 1347–1372. Springer Singapore, Singapore, 2019. ISBN 978-981-10-6884-3. doi:10.1007/978-981-10-6884-3_80.

[83] J Spahn, H Andrä, M Kabel, and R Müller. A multiscale approach for modeling progressive damage of composite materials using fast fourier transforms. *Computer Methods in Applied Mechanics and Engineering*, 268:871–883, 2014.

[84] Z.-H. Sung, M. Wang, A. A. Polyanskii, C. Santosh, S. Balachandran, C. Compton, D. C. Larbalestier, T. R. Bieler, and P. J. Lee. Development of low angle grain boundaries in lightly deformed superconducting niobium and their influence on hydride distribution and flux perturbation. *Journal of Applied Physics*, 121(19):193903, 2017. doi:10.1063/1.4983512.

[85] Zu-Hawn Sung, Peter J. Lee, Anatolii Polyanskii, Shreyas Balachandran, Santosh Chetri, David C. Larbalestier, Mingmin Wang, Christopher Compton, and Thomas R. Bieler. Large grain cbmm nb ingot slices: An ideal test bed for exploring the microstructure-electromagnetic property relationships relevant to srf. *AIP Conference Proceedings*, 1687 (1):020004, 2015. doi:10.1063/1.4935318.

[86] S Takeuchi, E Furubayashi, and T Taoka. Orientation dependence of yield stress in 4.4crystals. *Acta Metallurgica*, 15(7):1179–1191, 1967. ISSN 0001-6160. doi:10.1016/0001-

6160(67)90392-6.

[87] G. Taylor. Thermally-activated deformation of bcc metals and alloys. *Progress in Materials Science*, 36:29–61, 1992. ISSN 0079-6425. doi:10.1016/0079-6425(92)90004-Q.

[88] Geoffrey Ingram Taylor. The mechanism of plastic deformation of crystals. part i.—theoretical. *Proceedings of the Royal Society of London. Series A, Containing Papers of a Mathematical and Physical Character*, 145(855):362–387, 1934.

[89] Geoffrey Ingram Taylor and Constance F Elam. The distortion of iron crystals. *Proceedings of the Royal Society of London. Series A, Containing Papers of a Mathematical and Physical Character*, 112(761):337–361, 1926.

[90] V Vitek. Core structure of screw dislocations in body-centred cubic metals: relation to symmetry and interatomic bonding. *Philosophical Magazine*, 84(3-5):415–428, 2004. doi:10.1080/14786430310001611644.

[91] V Vitek and M Yamaguchi. Core structure of nonscrew dislocations on (110) planes in b.c.c. crystals. II. peierls stress and the effect of an external shear stress on the cores. *Journal of Physics F: Metal Physics*, 3(3):537–542, mar 1973. doi:10.1088/0305-4608/3/3/011.

[92] M Wang. *Effect of microscopic defects on superconducting properties of high purity niobium used for SRF cavities*. PhD thesis, Michigan State University, 2020.

[93] M Wang, D Kang, and TR Bieler. Direct observation of dislocation structure evolution in srf cavity niobium using electron channeling contrast imaging. *Journal of Applied Physics*, 124 (15):155105, 2018. doi:10.1063/1.5050032.

[94] Christopher R Weinberger, Garritt J Tucker, and Stephen M Foiles. Peierls potential of screw dislocations in bcc transition metals: Predictions from density functional theory. *Physical Review B*, 87(5):054114, 2013.

[95] Christopher Robert Weinberger, Brad Lee Boyce, and Corbett Chandler Battaile. Slip planes in bcc transition metals. *International materials reviews*, 58(5):296–314, 2013.

[96] François Willot. Fourier-based schemes for computing the mechanical response of composites with accurate local fields. *Comptes Rendus Mécanique*, 343(3):232–245, 2015.

[97] T Yalcinkaya, WAM Brekelmans, and MGD Geers. Bcc single crystal plasticity modeling and its experimental identification. *Modelling and Simulation in Materials Science and Engineering*, 16(8):085007, 2008. doi:10.1088/0965-0393/16/8/085007.

[98] OC Zienkiewicz. *The Finite Element Method in Structural and Continuum Mechanics: Numerical Solution of Problems in Structural and Contimuum Mechanics*. 1967.

APPENDIX A : SUMMARY OF SLIP SYSTEMS USED FOR NB

The particular order for slip systems in this thesis is consistent with the order followed in DAMASK (src/lattice.f90).

	slip system index	slip system
D1	1	$(0\,1\,1)[1\,\bar{1}\,1]$
C1	2	$(0\,1\,1)[\bar{1}\,\bar{1}\,1]$
B2	3	$(0\,\bar{1}\,1)[1\,1\,1]$
A2	4	$(0\,\bar{1}\,1)[\bar{1}\,1\,1]$
A3	5	$(1\,0\,1)[\bar{1}\,1\,1]$
C3	6	$(1\,0\,1)[\bar{1}\,\bar{1}\,1]$
B4	7	$(\bar{1}\,0\,1)[1\,1\,1]$
D4	8	$(\bar{1}\,0\,1)[1\,\bar{1}\,1]$
A6	9	$(1\,1\,0)[\bar{1}\,1\,1]$
D6	10	$(1\,1\,0)[\bar{1}\,1\,\bar{1}]$
B5	11	$(\bar{1}\,1\,0)[1\,1\,1]$
C5	12	$(\bar{1}\,1\,0)[1\,1\,\bar{1}]$
A-4	13	$(2\,1\,1)[\bar{1}\,1\,1]$
B-3	14	$(\bar{2}\,1\,1)[1\,1\,1]$
C-10	15	$(2\,\bar{1}\,1)[1\,1\,\bar{1}]$
D-9	16	$(2\,1\,\bar{1})[1\,\bar{1}\,1]$
D-6	17	$(1\,2\,1)[1\,\bar{1}\,1]$
C-5	18	$(\bar{1}\,2\,1)[1\,1\,\bar{1}]$
B-12	19	$(1\,\bar{2}\,1)[1\,1\,1]$
A-11	20	$(1\,2\,\bar{1})[\bar{1}\,1\,1]$
C-2	21	$(1\,1\,2)[1\,1\,\bar{1}]$
D-1	22	$(\bar{1}\,1\,2)[1\,\bar{1}\,1]$
A-8	23	$(1\,\bar{1}\,2)[\bar{1}\,1\,1]$
B-7	24	$(1\,1\,\bar{2})[1\,1\,1]$

Table A.1 The 24 slip systems and their respective indexes used in this thesis. Schmid and Boas notations for the same are summarized in the first column.

APPENDIX B : SOFTWARE DEVELOPED

The pre-processing scripts used to create geometries, boundary conditions, material parameters and the post-processing scripts to create stress–strain curves, plot lattice reorientations, shear rate, and other quantities are documented in an open repository on GitHub called “SXCPNiobium”. See https://github.com/EurekaPaiKulyadi/SXCPNiobium.git for details.

The Python codes and plotting scripts for the IPF visualization performed for Chapter 5 are documented in an open repository on GitHub called “Unique-Orientations-IPF”. See https://github.com/EurekaPaiKulyadi/Unique-Orientations-IPF.git for details.